Modelling the Nanocantilever Response to Stressed Networks of Antibiotic Binding Events

Anna Dejardin

London Centre for Nanotechnology
University College London

Supervisors:
Prof. A. Marshall Stoneham
Dr. Dorothy Duffy
Dr Rachel McKendry

Thesis submitted to UCL in partial fulfillment of the requirements for the degree of Doctor of Philosophy

2012

I, Anna Dejardin, confirm that the work presented in this thesis is my own. Where information has been derived from other sources, I confirm that this has been indicated in the thesis.

Abstract

Antibiotic resistance is a rapidly emerging global health problem as year on year more drugs are rendered ineffective and fewer new antibiotics developed to meet the demand. This is exemplified by Vancomycin, the 'antibiotic of last resort' for decades, now facing growing resistance among bacteria. Interest around modifying existing drugs to improve their antibiotic action and stabilise them against resistance is raising the need for detailed understanding of the modes of action of antibiotics.

Nanocantilevers provide a complementary method for exploring both the binding process and the mechanical mode of action by which Vancomycin and its derivatives weaken and destroy bacterial cell wall. When functionalised with monolayers of peptides analogous to cell wall precursors the cantilevers measure the build up of surface stresses in-plane, on a surface, representative of the antibacterial interactions in-situ.

This thesis reports the first steps towards a comprehensive theoretical model of stress induction on a nanocantilever, focusing on elucidating the chemical and geometric nature of experimentally observed responses to Vancomycin.

The chemical origins of stress generation are explored within, using a monolayer of decanethiol as a model system and looking at contributions from both adsorbate-adsorbate and adsorbate-substrate interactions. How those individual molecular contributions combine across the cantilever to produce the eventual deflection is investigated by varying the coverage of Vancomycin binding events across an appropriately functionalised cantilever, using an interaction potential

extrapolated from molecular dynamics simulations and a lattice model developed in this thesis to return the corresponding stress and deflection. The elastic response of the beam itself is also examined in some detail, as is the effect of the operating medium on the cantilever's action.

All findings provide the first steps to a truly representative, and quantitatively predictive, model of nanocantilever operation and insight into the technology's unique merit in the race to discover a new generation of antibiotics.

Acknowledgements

This thesis is dedicated to the memory of Marshall Stoneham, without whom it would not exist. I owe him much, not least sincere thanks for his support, generosity and originality.

My supervisors, Dorothy and Rachel, have been hugely supportive and deserve massive thanks for making this process so much more pleasant and enjoyable. Particular thanks to Dorothy for taking me on in a difficult time and at a late stage and helping keep everything on track and to Rachel for her continuing belief in the thesis and her financial support.

I'd also like to acknowledge here all those colleagues, across the institution, who quietly and simply offered me their time and their help in the spring of 2011.

Many thanks to the experimentalists I've worked with over the course of the past few years; their work has been a motivation and their insights and advice a grounding connection to the real world. This includes Rosie Paxman and Bart Hoogenboom for involving me in their work on dynamic cantilevers as rheological sensors and for the many discussions around the area, and Manuel Vogtli, Joe Bailey and Joseph Ndieyira for sharing their data and findings so openly and prompting discussion and research that deepened my understanding of the experimental limitations and possibilities of biosensing through surface stress generation.

I would also like to thank Tony Harker, for giving so freely of his time to answer my Mathematica queries, and Gabriel Aeppli for his interest and advice.

Thanks must also go to all those people I've met through the LCN who, though unconnected to my work, have provided a lot of support. To Ana-Sofia who helped me get settled in the first few days and has been my DL POLY go-to; to Maria Sushko who offered her insights into simulation techniques and potentials; to Dara for his ever patient and illuminating explanations; to Marc for good advice on curve fitting and on knowing when to just get on with it; to Charlie and Rich, for many hours, numerous teas and seemingly endless talk of letters and numbers; and to Simon, my PhD next of kin, for all that entails, and then some.

Contents

List of Figures

List of Tables

Chapter 1

Introduction

This thesis is predominantly interested in the theory surrounding the intersection at which a rapidly emerging health problem and a newly developed technology meet. The problem is global, with terrifying consequences; that of increasing antibiotic resistance and dwindling production of new drugs to fill the gaps. The technology exploits the simple, mechanical mode of action of nanocantilevers, but suffers from a lack of complete understanding as to how signals are transduced.

1.1 Antibiotic resistance

As can be seen in the timeline in figure (1.1.1), showing the number of antibiotics approved by the US over the past few decades, the process of discovery, development and release of new antibiotics that began in the 40s with Penicillin is falling off rapidly. This is in part due to our having potentially reached the end of naturally occurring antibiotic agents [1] and to pharmaceutical companies being unwilling to pour money and time into products that guarantee little assurance of financial return, developed as they are to be administered in short runs. Unfortunately this dearth of antimicrobial drugs comes alongside an increase in resistance in bacteria, due to genetic mutation and sharing of genetic

material and no doubt exacerbated by the overuse and misuse of antibiotics [2].

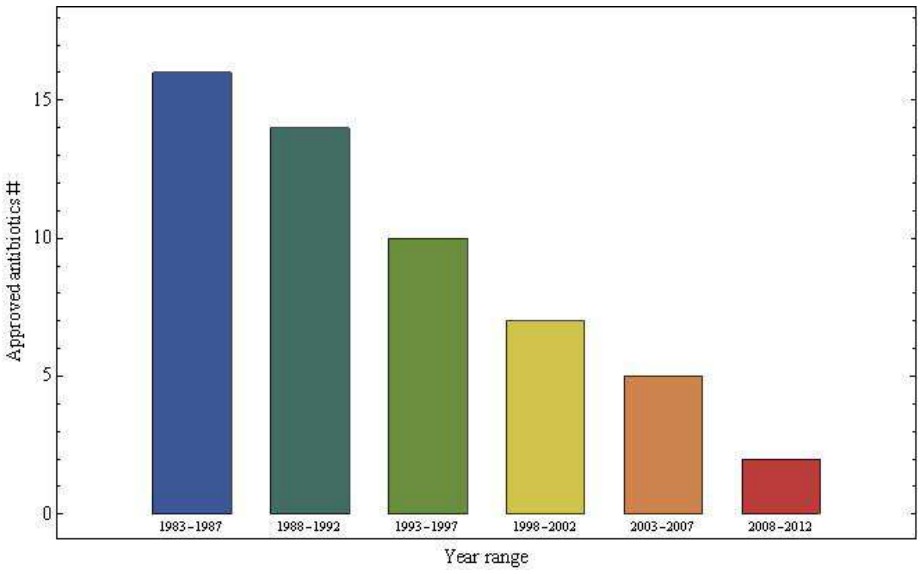

Figure 1.1.1: Showing the falloff in the number of new antibiotics licensed by the US in the last three decades. Data from the Infectious Diseases Society of America.

Attention within the industry has shifted to synthetic drugs; modifications to existing antibiotics can produce newly effective derivatives [3]. As cost and time are, as ever, of the essence, this is a process that must be approached as efficiently as possible. Logical steps towards improving the antibiotic action and stabilising systems against resistance come from detailed understanding of the modes of action of antibiotics and the processes by which resistance occurs.

1.2 Vancomycin

Vancomycin is widely known as 'the antibiotic of last resort', used therapeutically against gram-positive bacteria such as Staphylococci that are frequently responsible for post-surgical infection. It is often the last effective antibiotic as all others are rendered ineffective by increasingly resistant strains of bacteria, as epitomised by methicillin resistant staphylococcus aureus (MRSA), the hospital

'superbug'.

Bacterial cells are distinguished from animal cells by the presence of a cell wall. In gram-positive bacteria, which are the subset to which the work in this thesis relates, the inner membrane holding the bacterial cytoplasm and all the workings of the living cell is surrounded by a thick layer of peptidoglycan.

Peptidoglycan is predominantly made up of two sugars, N-acetyl glucosamine and N-acetyl muramic acid, which are cross-linked for structure and stability by amino acid bridging structures, mucopeptides, the make-up of which varies between bacterial types. In the process of the cell wall being built, mucopeptide precursors project from individual polysaccharide chains around the bacterium. In the case of those bacteria that Vancomycin attacks, this mucopeptide precursor terminates in the amino acid sequence L-Lysine-D-Alanyl-D-Alanine [4]. The D- amino acids, not generally found within proteins in nature, help to protect the structure against degradation by proteases, and the cross-linking leads to a framework that is both strong and rigid, to maintain the bacterium's shape and prevent it from rupturing due to internal osmotic pressure.

In the normal process of events the terminal sequence of L-Lys-D-Ala-D-Ala of the precursor is recognised by a transpeptidase enzyme which cross-links two adjacent sugars via removal of the final D-Ala [5]. But in the presence of Vancomycin this operation is interrupted. Vancomycin, and other antibiotics in its family, binds to the cell wall mucopeptide precursors; to that very sequence of L-Lys-D-Ala-D-Ala that the transpeptidases recognise, competitively inhibiting their action [6, 7].

All glycopeptide antibiotics consist of a backbone of seven amino acids, with differing chemical groups attached to this central structure [5]. It is into this backbone pocket that the end of the mucopeptide precursor is bound. The two bind to each other due to a combination of hydrophobic interactions and the formation of five hydrogen bonds along the mucopeptide, as can be seen in figure (1.2.2) [6, 8, 9]. The hydrogen bonds on the terminal carboxylate group provide most of the binding energy. The other two work to align the mucopeptide so hydrophobic forces can properly come to bear on the complex, and to stabilise

the structure against motion that would weaken the binding effect of the COOH centred bonds [5].

However, Vancomycin's effectiveness does not remain unchallenged. It has lasted remarkably well, but due in part to overuse and misuse of antibiotics, resistance is on the increase [11, 12, 13]. With nothing as effective poised to fill Vancomycin's shoes, the impact on public health could be enormous [14].

Bacterial resistance to Vancomycin can occur through the deletion of a single hydrogen bond between the antibiotic and its binding site on the bacterial cell-wall precursor, when the D-Ala-D-Ala terminating sequence is replaced by D-Ala-D-Lac, as demonstrated in figure (1.2.1). The replacement of an ester linkage from an amide lowers the binding affinity of the antibiotic to the peptide terminating sequence by around 1000 [3] and leaves Vancomycin unable to perform therapeutically, see figure (1.2.2).

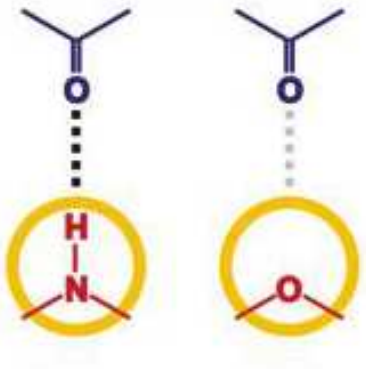

Figure 1.2.1: Showing how the substitution of an ester group for an amide results in the removal of one of the hydrogen bonds between the Vancomycin binding pocket and cell wall mucopeptide precursor. Figure adapted from [15] with permission from Macmillan Publishers Ltd.

All this through a seemingly simple substitution which, in fact, is the result of resistant bacteria, such as vancomycin resistant enterococci (VRE), having obtained five different new pieces of genetic information from other bacteria, leading to the expression of D-Lactate instead of D-Alanine at the very end of

the mucopeptide precursors [16, 17].

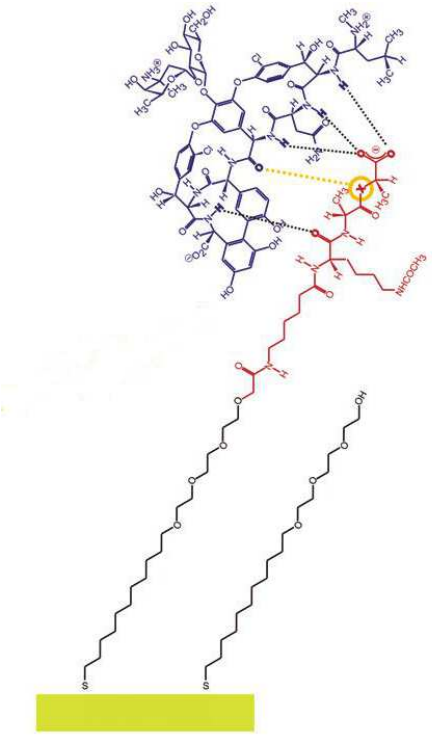

Figure 1.2.2: Showing the single hydrogen bond, the deletion of which renders Vancomycin therapeutically ineffective. Figure adapted from [15] with permission from Macmillan Publishers Ltd.

While the alteration to the bacterial binding site renders Vancomycin ineffectual, some Van derivatives have shown a remarkable effectiveness against enterococci resistant to Vancomycin [3]. The binding pocket of the derivatives does not vary from that of Vancomycin, but the chemical groups along their backbones differ from molecule to molecule. Speculation in the literature [18, 19] suggests that through a higher tendency towards dimerisation or an ability to anchor themselves to the bacterial lipid membrane, derivatives such as Chloroeremomycin [20] and Oritavancin [21] are stabilised against the disruptive effect of the deletion of that one binding pocket H-bond.

Oritavancin, synthetically modified from Chloroeremomycin through addi-

tion of a new hydrophobic group onto the backbone, is more active than Van by 50 times against VRE [22] and even, where resistance is not yet an issue, by up to eight times against MRSA. But, in solution, they both show the same low affinity for the resistant D-Ala-D-Lac terminating precursor [23]. It is on a surface, as the exterior of a bacterium, that the modifications to Oritavancin appear to make all the difference to its efficacy [21].

So, a sensing and measurement technology is required that can explore the antibiotics' action at a surface. If the solution phase binding constants don't directly reflect the drug's activity in vivo, then information on valid dosage amounts from minimum inhibitory concentrations and on their direct mode of action, that may lead to new avenues of rational design for new synthetic antibiotics, must come from a system that more closely replicates the reality of the bacterial cell wall surface.

The possibilities that these discoveries suggest for the development of novel antibiotics in an increasingly desperate market are driving research into this class of antibiotics and into new technologies that can reliably and accurately reflect their differences in antibiotic action.

1.3 Nanocantilevers

As a biosensing technology, nanocantilevers have been generating interest for over a decade for their robustness, ease of manufacture and ability to operate in real-time, providing their own experimental control. Now, interest is once again piqued around their potential ability not only to characterise and quantify different species of biomolecules, but also to probe the nature of those of their reactions and interactions that have a mechanical basis.

This is exemplified in this report by the example of the gram-positive glycopeptide antibiotic Vancomycin. In 2008 Ndieyira et al [15] published their findings for Vancomycin binding to both sensitive and resistant bacterial cell-wall precursor analogues immobilised on a cantilever's surface. They were able to demonstrate sensitivity at clinically relevant concentrations and in the bi-

ologically realistic environment of blood serum. With the benefit of existing information on the structural and binding properties of antibiotic-mucopeptide complexes, in free solution and at surfaces [24, 20, 6], the system could also be used to gain new insights into the transduction of stress through the cantilever setup. Their findings ultimately suggested the need to include a geometrical factor, as well as the accepted chemical binding dependence, in any theoretical framework that aims to describe a surface stress response.

The data suggest that the origin of surface stress due to specific binding events is short-ranged in nature, for example a steric nearest-neighbour interaction between adsorbed proteins. These results also serve to underline the importance of the structure of the underlying self-assembled monolayers (SAMs) to which analytes bind in the response one gets from cantilever sensors. It throws into sharp relief the suitability of cantilever sensors in this field, over other methods of measurement that operate with the analyte in solution. By providing a surface for the binding events, this sensor technology mimics the bacterial membrane upon which the actual petidoglycan precursors are attached. Diffusion and dissociation constants have been shown to vary significantly between events occurring in solution and on a surface [21]. There is also speculation in the literature [3] that antibiotics such as Vancomycin, in their mode of action against bacteria, disrupt cell walls collectively in much the same way as stress would appear to be transduced on a cantilever's surface, as represented in figure (1.3.1). With nanocantilever technology a viable way of quantifying not only the binding affinity of a drug-target complex, but also the antimicrobial efficacy of said drug, this would mean that nanocantilevers could provide both a quick and easy method of characterising many drugs at the same time and a method by which their action can be understood and improved upon.

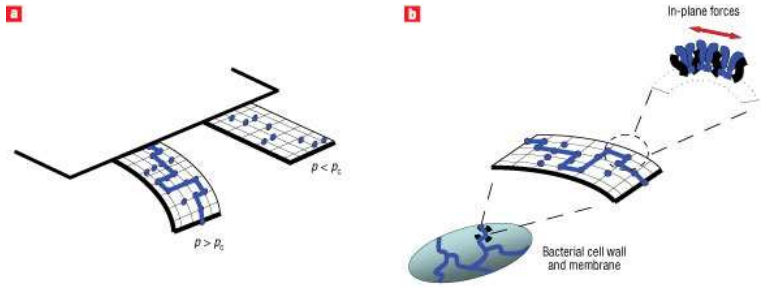

Figure 1.3.1: Schematics representing the idea that the proximity and connectivity of binding events factors into the stress response of a cantilever (a) and the antibiotic disruption of the bacterial cell wall (b). Figure reproduced from [15] with permission from Macmillan Publishers Ltd.

1.4 Modelling the nanocantilever system

For nanocantilevers to be a viable technology on which to base a biosensor it must be possible to accurately and repeatedly get a quantitatively well understood response from them. It must be possible to take individual chemical events, featuring molecules only tens of angstroms in diameter, and translate their effects to the observed mechanical motion of a beam thousands of times larger.

As such, theoretical study of nanocantilevers as biosensors has to give due attention to what is happening on several levels: the molecular origins of force generation; how these forces collectively combine across the cantilever's back; and how the cantilever beam itself responds to such an impetus. Within this thesis I make investigations into all of these.

To look at the molecular basis for surface stress I break down the contributions for each adsorbed molecule into those steric and coulombic interactions stemming from molecular proximity on the cantilever, and those due to adsorption induced reorganisation of charge at the cantilever's surface. In some cases, as for a monolayer of decanethiol (section (5)), these are relatively simple to approximate. But for a molecule as complex as Vancomycin I have used molecular dynamics simulation to explore the nature of their interactions.

By taking the likely arrangement of adsorbed molecules across the active area of a cantilever I calculate the net forces across the cantilever due to all the molecular contributions. I have tested the impact of varying molecular arrangement, or the connectivity between individual sites, using a model I wrote in Mathematica 8.0 [25] to sum the individual and pairwise force contributions and equate the result to the restoring force of the cantilever beam.

How the response of the beam itself affects the subsequent measurement is something I investigate through deriving analytic formulae for altered geometric and material properties of a beam. I also devote time to implementing models that describe the effects of complex fluids on a cantilever's operation, as the environmental influence is hugely important for a technology that will eventually be required to operate successfully in fluids such as blood.

1.5 Thesis outline

Laid out here for the purpose of clarity, there follows a short description of the sections comprising this thesis.

The next part of this thesis goes into more detail on the immediate motivation that led to this work and on the wider context in which my work is positioned.

Chapter (2) looks at nanocantilevers as a novel and promising technology for both sensing the presence of specific analytes and exploring chemical reactions. The section describes in detail the mode of action of nanocantilevers and their myriad applications in various fields.

The next chapter, chapter (3), goes into the theory and methods used for the simulations performed as part of the thesis. The necessary steps to achieving meaningful results from molecular dynamics simulation are explained; the particular model used for Vancomycin and the theory necessary to use calculations in the potential of mean force ensemble to quantify the mean force of interaction of two Vancomycin molecules.

Chapter (4) summarises an experimental investigation [15] into the stress response of cantilevers functionalised with gram-positive bacterial cell wall peptide analogues (both active and resistant) upon exposure to Vancomycin. The publication in question also looks into how changing the coverage of active peptides on a cantilever's surface alters the stress response, raising questions around a possible geometric, as well as chemical, contribution to the stress; questions which this thesis works towards answering.

From there on, each remaining chapter of the thesis describes a body of work, as completed by me, that aims to answer the questions and challenges raised in these introductory passages.

Chapter (5) uses the model system of a full monolayer of decanethiol on the sensing surface of a nanocantilever to explore the mechanisms by which surface stress is induced upon adsorption. The chapter outlines current thinking as to the basis for stress changes and introduces a model developed by me in Mathematica 8.0 [25] to quantify the contribution of each in the specific case of decanethiol and equate them to the elastic restoring force of the beam to yield a stress. The results are compared with previously reported experimental data for similar setups, from the literature.

Chapter (6) describes the extensions to the model discussed in chapter (5) necessary to elucidate the geometric nature of surface stress buildup. Percolation theory is introduced and used as a starting point to investigate how active monolayer coverage is linked to a cantilever's stress response.

In chapter (7) the theory and ideas developed thus far are applied to the case of Vancomycin binding to a cantilever coated in bacterial cell wall peptide analogues. The first half of the chapter details the molecular dynamics simulations run on two approaching Vancomycin-peptide complexes, the interpretation and analysis of the mean force between them at each separation and how the data can be developed into a force expression representative of their interaction. The second half discusses how the Mathematica model for stress must be evolved to better reflect this setup and provides the results of surface stress and cantilever deflection induced by the binding of Vancomycin and how it varies with active

peptide coverage. These results are compared with the experimental results introduced in chapter (4) and show good agreement considering the complexity of the system.

Chapter (8) returns to look at the nature of the elastic response of the cantilever to bending. In the interest of both understanding and maximising the sensitivity of the beam to events on its surface I consider what effect the geometric proportions and material properties of the beam have on a response. This is also extended to look at the consequences of differing how the active surface is patterned on the cantilever.

In chapter (9) I consider the issue of operating in complex or viscous media, from the perspective of the dynamic cantilever mode of action, and how to exploit this apparent challenge to measure the rheological properties of the operating medium.

The final chapter, (10), reiterates the discoveries and conclusions of the thesis and raises avenues of interest for future work in this area.

Chapter 2

Biosensors

'Biosensor' is quite a broad term, covering those devices that couple a bioreceptor that recognises the chosen analyte and a transducer that converts the information about that analyte to a measurable form that is easily quantified by the user.

The receptor's task is to bind to or otherwise chemically interact with the analyte. The key deliverable here is specificity and, as such, the type of receptor is tailored individually for each arrangement. Possible receptors are as varied as the biomolecules one is looking to isolate and are often taken directly from nature to exploit existing biochemical mechanisms for recognition. This biosensitive part of the device can utilise antibodies, enzymes or other proteins, single DNA strands; as long as the receptor and analyte demonstrate complementary behaviour.

The transducer part of a sensor is where the actual signal that will be measured is generated. A few widely used examples include the optical method of surface plasmon resonance (SPR) [26] which measures changes in the dielectric constant at a surface, electromechanical methods such as quartz crystal microbalance (QCM) [27] where changes to the resonant frequency of oscillation due to analytes is measured piezoelectrically, or by utilising the electron release from enzyme-analyte reactions in certain electrochemical sensors, as typified by

glucose sensors for monitoring diabetes [28].

When developing a technology for use as biosensor, top of every wish list are two words: sensitivity and specificity. The first, sensitivity, is a requirement that must be met by any biosensor. Clinically relevant concentrations of biologically important analytes can dip well below the μM range [29, 30, 31]. But sensitivity is a pretty useless concept without specificity. For a response to have meaning one must either be able to obtain a signal that corresponds to a single type of target molecule or system parameter, or have the requisite understanding to deconvolute the contributions to a signal from many, potentially competing, effects or analytes.

Nanocantilevers are appealing to the biosensor community due to their general robustness, ease of manufacture and their suitability for miniaturisation and incorporation into lab-on-a-chip (LOAC) devices. It is a versatile technology, able to operate in different modes of action (2.3.1,2.3.2), as in figure (2.3.1), and to be specifically functionalised with relative ease [32].

However, understanding of a cantilever's response often does not comprehensively extend beyond qualitative. For the potential applications in environmental monitoring, food standards and medicine, it is extremely important to be certain of a reliable, quantitatively understood response.

2.1 Nanocantilevers

Many features of nanocantilevers make them an extremely promising technology for application to the combined challenges of finding new antibiotics and of quantifying their efficacy.

With no need for secondary tags cantilevers operate as label-free sensors, allowing for measurement in one step, which speeds up and simplifies the process. The deflection signal from nanocantilevers is not specifically mass limited, such as SPR [33] and although, as I shall discuss in more detail in chapter (4) of the thesis, there is a limiting signal dependence on the degree of binding to the cantilever, this technology can be shown to respond to clinically relevant

concentrations of analytes.

The compatibility of cantilevers with miniaturisation and parallelisation [34] techniques has a twofold advantage. In a field where time is very much of the essence, this technology would be capable of high throughput drug screening, reckoned at thousands of drugs per hour, and integrated arrays can screen several different analyte-target interactions, as well as taking reference measurements, in identical conditions simultaneously, allowing for directly differential output and with applications to LOAC devices.

2.2 Development of the technology

The development of nanocantilevers as stand alone sensors begins with the the development of the Atomic Force Microscope (AFM) in the mid eighties by Binnig, Quate and Gerber [35]. The AFM setup incorporates a nanocantilever, on the end of which is situated a small tip of the order of nanometres in dimension. This tip, when scanned across the surface of a sample, will experience either a static deflection due to interatomic forces between tip and sample or, if the cantilever is resonating, a shift in frequency corresponding to the effect of said forces.

The deflection and frequency response, generally measured optically, is used to build up a topographical map of the sample with spatial resolutions down to the nanoscale.

The setup has proved to be versatile, with people able to use contact mode AFM to quantify mechanical and elastic properties of samples [36, 37], or utilising specialist magnetic or conducting tips to expose the magnetic patterns in thin films [38] and localised charge distributions [39] respectively.

Following the success of the AFM, the nanocantilever itself has been redeveloped as a functionalisable device in its own right, for use as a chemical, biological or physical sensor in medicine, industry and environmental monitoring [40, 41, 42, 43, 44, 45]. The technology relies upon the fact that any change in mass, stiffness, surface stress or the medium in which a cantilever is operating

will lead to a deflection away from its control position or a shift in its resonant frequencies and a change of quality factor.

The first published work that focused on this technology's potential for use as a biosensor was Butt's 1996 paper [46] showing the response of a cantilever to non-specific adsorption of bovine serum albumin. In the following years researchers tried different functionalisation and adsorbates to investigate the potential of nanomechanical biosensing.

2.3 Modes of action

2.3.1 Static mode

When analytes in the medium surrounding a cantilever interact with the surface of the beam, whether through physisorption or chemisorption via covalent bond formation, these events will alter the stresses on the surface of the cantilever. See (b) of figure (2.3.1) for a simple schematic of a cantilever in its static mode of operation.

If the beam is prepared such that these events can only occur on one side, e.g. the upper surface, a differential surface stress induces bending in the beam.

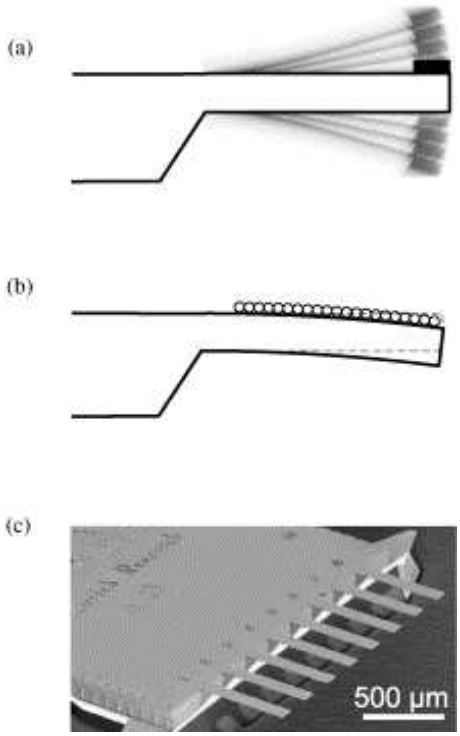

Figure 2.3.1: The two most common cantilever modes of action: (a) dynamic mode responding to changes in adsorbed mass, stiffness or changes to the rheology of the operating medium; (b) static mode responding to surface stress changes; (c) a scanning electron micrograph of an actual cantilever array. Image courtesy of [47] with permission from Elsevier.

The strain in the y-direction across the beam, as described in the schematic comprising figure (2.3.2), with a height h_0 to the neutral plane of the beam, can be written as,

$$\epsilon_{yy}(x) = \frac{x - h_0}{R}, \tag{2.3.1}$$

where in this instance we take the radius of curvature, R, to extend from the centre of the circle that would be described by the arc of a cantilever undergoing pure bending, to the lower surface of the beam. From Hooke's Law, the bulk stress through the beam in the same direction is,

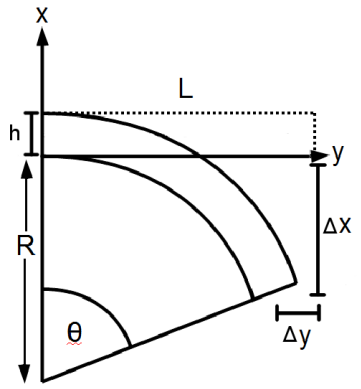

Figure 2.3.2: Schematic showing the axes and dimensions of a beam undergoing pure bending.

$$G_{yy}(x) = \frac{E}{(1-\nu)}\epsilon_{yy}(x), \tag{2.3.2}$$

where E is the Young's modulus and ν the Poisson ratio of the material comprising the beam.

In a system in equilibrium the total surface stress acting on the cantilever, which is the difference between that acting on the upper and lower surfaces, $\Delta\sigma$, must be equal in magnitude and opposite in sign to the bulk stress as integrated over the full height of the beam.

$$\Delta\sigma_{yy} = -\int G_{yy}dx \tag{2.3.3}$$

$$= -\int_0^h \frac{E}{(1-\nu)}\frac{(x-h_0)}{R}dx$$

From the expression above we can define the differential surface stress in the y direction as

$$\Delta\sigma_{yy} = \frac{-Eh}{(1-\nu)R}\left(\frac{h}{2} - h_0\right), \tag{2.3.4}$$

which can be rearranged to yield the expression

$$h_0 = \frac{h}{2} + \frac{\Delta\sigma_{yy}(1-\nu)R}{Eh}. \tag{2.3.5}$$

This leads to a definition of strain of

$$\epsilon_{yy} = \frac{\left(x - \frac{\delta\sigma_{yy}(1-\nu)R}{Eh} - \frac{h}{2}\right)}{R}. \tag{2.3.6}$$

In equilibrium, the bending moment inside the cantilever must be zero. So, for example, for the midplane of the cantilever:

$$\int G_{yy}(x)\left(x - \frac{h}{2}\right)dx - \frac{\Delta\sigma_{yy}h}{2} = 0, \tag{2.3.7}$$

which, upon working, collapses down to

$$\Delta\sigma_{yy} = \frac{Eh^2}{6R(1-\nu)}. \tag{2.3.8}$$

This form is widely known as Stoney's equation [48] and has been used to describe stress induced deflection since the early 20th century.

These expressions will need modification where the thin-film approximation is no longer valid, however as long as the ratio of layer thicknesses follows $\Delta h = \frac{h_a}{h_s} \leq 0.1$, where h_a and h_s are the adsorbate and substrate layer thicknesses, these assumptions do not cause serious errors in calculation [49]. This approximation is valid for the systems that we will be considering. While the micro-scale mechanical response of the beam in this mode is reasonably well characterised, the process by which individual molecular events induce the surface stresses is not fully understood and a matter of some debate in the literature [50, 51, 52, 53, 54, 55, 56, 57, 58]. I will be discussing possible origins of surface stress and some of the figures of merit of a cantilever's mechanical response later in this thesis.

2.3.2 Dynamic mode

In the dynamic mode cantilevers are generally modelled as harmonic oscillators, with the resonance frequency, ω_n, of the nth mode given by

$$\omega_n = \frac{C_n^2}{L^2}\sqrt{\frac{EI_y}{\mu}}, \tag{2.3.9}$$

where L is the beam length, I_y the moment of inertia in the y direction, μ the mass per unit length of the beam and the coefficients C_n which are derived in appendix (B). Any changes in the material properties or operating environment of such a cantilever will result in a shift in the resonance frequencies. Most often used as a mass sensor [59, 60, 61, 62], the effect of added mass on the resonance frequency of a beam oscillating in the dynamic mode can be simply written as

$$\Delta\omega = -\frac{1}{2}\frac{\Delta m}{m}\omega_n, \tag{2.3.10}$$

where Δm and m are the added mass and mass of the cantilever. In situations where adsorption events cover enough of the cantilever to form a layer, the mass increase can be coupled to a change in the stiffness of the cantilever, which will also affect the resonance behaviour of the device [63, 64]. For a homogeneous adsorbed layer the shifted resonance frequency is described by

$$\frac{\omega_n}{\omega_{n,0}} = \sqrt{\frac{\Delta D}{1+\rho_{\text{eff}}h_{\text{eff}}}}, \tag{2.3.11}$$

where ΔD is the change in flexural rigidity, a property of the beam that depends on the Young's modulus, the Poisson ratio and the thickness, and $\rho_{\text{eff}} = \frac{\rho_a}{\rho_s}$ and $h_{\text{eff}} = \frac{h_a}{h_s}$ are the ratios of adsorbed layer to substrate layer densities and thicknesses respectively. Recent work has developed models to deconvolute the contributions of mass and stiffness [63]; an important pursuit since the two can have opposing effects. The dynamic mode setup can be further complicated by the effects of the medium in which the cantilever operates. Changes to the operating medium's rheological properties, for instance, will affect the resonance

frequency of an oscillator.

Dense and viscous media also have a drastic effect on the limit of sensitivity for a vibrating cantilever, which is governed by the signal to noise ratio. The degree to which a resonance frequency shift, and thus the quantity one is seeking to measure, can be resolved is described using the dimensionless parameter Q, the quality factor. Defined as $Q = \frac{\omega_n}{\Delta\omega_{\text{fwhm}}}$, the ratio between the resonance frequency and the full width at half-maximum of the resonance peak, Q must be maximised to achieve the best sensitivity, but will decrease significantly if the damping in the system increases, say due to a more dense and viscous medium. This is discussed in greater detail in chapter (9).

2.4 Applications

Static

Perhaps the landmark publication of this time was the work undertaken by Fritz et al [65] who demonstrated measurable, relative deflection of two cantilevers responding to the hybridisation of DNA chains immobilised on the cantilever surfaces. The difference in signal between the cantilevers was solely due to the effect of a single base mismatch and really highlighted the possibility of using the surface stress technique to quantify not only the presence and concentration of an analyte, but also its interaction with other ligands and even the efficacy of the chemical reactions it is involved in.

There followed a series of papers further investigating sequence-specific DNA hybridisation events [66, 67, 68, 69] including the extension to being able to discriminate between single base mismatches at particular sites on the DNA chains [70], and the detection of DNA quadruplexes [71].

The importance of tailored and analyte-specific functionalisation of the cantilevers cannot be underestimated, and has been exploited in specific protein and chemical recognition experiments. Volatile compounds including chemical solvents, primary alcohols and natural flavours, like bitter almond, cherry, lemon

and vanilla, have been specifically detected using cantilevers [65], that respond to absorption induced polymer swelling. They are designed to operate as an 'artificial nose' by building a fingerprinted picture of the environmental contents from the differential response of an array of cantilevers. Environmental monitoring benefits from the real-time response of nanocantilever devices and they have been shown to respond to trace amounts of nerve agents [72], pathogens such as strains of Salmonella enterica [73], Cholera toxin [74] and explosives [75] with sensitivities comparable to that of a dog's nose [76].

The technology's suitability as a biomedical sensor has been researched, with focus centred on those molecules that are known to act as either therapeutic targets or as indicators of disease and disease progression. For example, as a potential marker for both viral infections and melanoma progression, the detection of interferon-alpha-induced 1-8U gene expression in total human RNA has been reported [69].

By discriminatingly functionalising cantilevers, it has become possible to detect the response of a single analyte, even in complex biological media. For example, the detection of the protein CDK2 in lysate cells [77], of prostate-specific antigens (PSA) in blood serum [78] or of the cardiac biomarker proteins creatin kinase and myoglobin in a non-specific protein background [79]. Surface stress responses have also been used to monitor conformational changes in systems such as adsorbed bovine serum albumim and Immunoglobulin G adsorbed onto Au surfaces [80] and protracted processes like the formation of protein aggregates in amyloid growth [81].

These examples of research in the field of nanomechanical biosensing show some impressive figures for sensitivity and reproducibility, but the actual processes by which the surface stress response is induced is still a matter of much debate in the literature [50, 51, 52, 53, 54, 55, 56, 57, 58]. In order to be an applicable technology in fields such as medicine and food and environmental monitoring, where results must be rigorously quantifiable, the link between the individual chemical and binding events on a cantilever's surface and the mechanical, continuum response of the cantilever beam must be fully understood.

Dynamic

Mass sensing in particular is a highly researched use for cantilevers in their dynamic mode [82, 83, 84]. In vacuum especially, this process is becoming well refined with cantilevers able to detect the specific binding of single viruses [41] or protein molecules [61]. Mass sensitivity in the sub-attogram range has been achieved [59]. Using super-cooling techniques and a 1 nm diameter carbon nanotube as a resonator, measurement of the adsorption of chromium atoms has been seen at 1.4 zeptograms [62].

On the introduction of a dense and viscous medium, however, the mass resolution suffers a great deal and other factors contribute to the shift in resonance frequency. Both dissipative and inertial effects of the immersion in the fluid must be accounted for in order to de-convolute the effect of the medium on the cantilever's action from the true signal.

It may seem counterproductive to look into cantilever operation in such media when sensitivity can be so clearly improved by letting the beam resonate in a vacuum [62, 59, 61, 85], but a lot of the interest around cantilevers is the potential for this technology to be incorporated into point-of-care devices. In order for this potential to be realised, several factors must be considered simultaneously; cantilevers must respond to clinically relevant analyte concentrations in real time, and in biologically appropriate environments. While for a lot of the gas sensing applications these criteria are being met already, in industries such as food and drink and for medical usage, 'biologically appropriate' often means working in dense, viscous media such as blood, serum or alcohol [86, 87]. The challenge presented by the surrounding medium is twofold; the signal to noise ratio must be amplified as much as possible, and the myriad potential contributions to that signal must be separated and understood.

For many applications the main aim is to minimise the effects of the medium. Burg et al [88] designed a novel cantilever that resonates in vacuum, with an internal reservoir of fluid, that can measure the mass of a single bacterial cell without removing it from a biological medium. In chapter (9), however, I will explore how these seemingly adverse effects can be instead manipulated to yield

information about the rheological nature of the medium.

Chapter 3

Methods

3.1 Molecular dynamics

Molecular dynamics (MD) follows from the premise that, given a sufficiently representative set of force fields, a system's behaviour can be extrapolated from the system's initial state. By calculating the forces of interaction between all the particles, the momenta and time evolved positions can be found. Repeatedly doing so will yield trajectories for each of the individual atoms comprising the system, whereupon time averages of the observable properties of the system may be calculated.

Based on the ergodic hypothesis [89], thermodynamic properties of the system can be determined by virtue of the fact that time averages can be equated to statistical ensemble averages. An ensemble used in MD denotes the trajectory in phase space along which the simulation can develop as a function of time. The set of points in phase space that correspond to a particular ensemble are dictated by those constant properties of the macrostate describing the system. Over a sufficiently long period of time, a simulation will have explored enough of the available microstates, enough of the available points on the ensemble hypersphere in phase space, for a time-averaged observable to be equivalent to an average of that observable in all the available microstates.

Simulation of a system of interest follows three main steps: construction of an appropriate but simplified model; calculation of particular trajectories; and analysis.

3.2 The model

The 'molecule' and its 'environment' in simulation must be explicitly defined by the user. There is a need to balance the complexity of the actual, real-world, situation one is trying to explore against the simplifications required to keep computing time manageable.

As such, we can describe the energy of a molecule in simulation as a combination of pairwise additive bonded and non-bonded atomic interactions, using empirical parameters for the different atomic species.

$$U_{tot} = U_{bonded} + U_{non-bonded} \tag{3.2.1}$$

Many model potentials exist that are tailored to the requirements of specific systems. For example Sutton-Chen [90] and embedded-atom method (EAM) potentials [91] for metals, Hautman-Klein models [92] for alkyl-thiols on a surface, or Tersoff potentials [93] describing carbon based systems. Within this chapter I shall only outline those potential forms used in this work.

The bonded interactions consist of descriptions of stretching, bending and torsional movement within a molecule as,

$$U_{bonded} = \sum_{i,j=1}^{N_{bond}} U_{bond} + \sum_{i,j,k=1}^{N_{angle}} U_{angle} + \sum_{i,j,k,l=1}^{N_{dihedral}} U_{dihedral}, \tag{3.2.2}$$

where,

$$U_{bond}(r_{ij}) = \frac{1}{2}k(r_{ij} - r_0)^2 \tag{3.2.3}$$

$$U_{angle}(\theta_{ijk}) = \frac{1}{2}k(\theta_{ijk} - \theta_0)^2 \tag{3.2.4}$$

$$U_{dihedral}(\phi_{ijkl}) = A[1 + cos(m\phi_{ijkl} - \delta)] \tag{3.2.5}$$

where k and A are force constants defining the shape of the potentials, δ is the phase and the other variables are as demonstrated in figure (3.2.1).

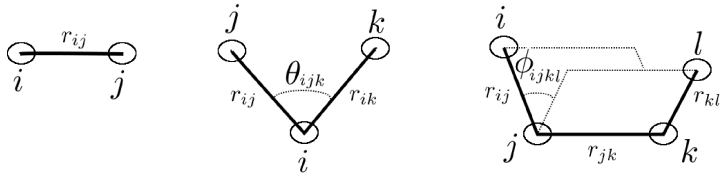

Figure 3.2.1: Diagram detailing the variables of the bond, angle and dihedral potential forms.

Non-bonded interactions are a sum of a short-ranged van der Waals and a long-ranged coulombic interaction which, for individual pairs of atoms, can be written as

$$U_{non-bonded} = \sum_{pairs} U_{VdW} + \sum_{pairs} U_{coul}, \tag{3.2.6}$$

where,

$$U_{VdW}(r_{ij}) = \left(\frac{A}{r_{ij}^{12}}\right) - \left(\frac{B}{r_{ij}^{6}}\right) \tag{3.2.7}$$

$$U_{coul}(r_{ij}) = \frac{1}{4\pi\epsilon_0}\frac{q_i q_j}{r_{ij}}. \tag{3.2.8}$$

$A = 4\epsilon\sigma^{12}$ and $B = 4\epsilon\sigma^6$ for a potential well depth of ϵ and finite distance at which the potential is zero of σ. q_i, q_j and r_{ij} are the charge on particle i, on particle j and the distance between the two, respectively.

The equilibrium topology of a molecule, the force constants that describe the

tolerances on atomic movement within that topology and the partial charges on each atom must be defined prior to simulation. Within this thesis, these values are taken from the CHARMM force field libraries [94, 95].

3.3 Initial conditions

Initial particle positions are provided as input by the user, and must be chosen so as to be compatible with the system that is being modelled. In many cases the initial coordinates are taken from those experimentally determined for the structures of interest, although generally these will require the addition of hydrogen atoms.

Initial velocities are either randomly assigned according to a distribution based on the desired temperature, T, of the system, or taken from previous simulations.

3.4 The ensemble

In this thesis, the simulations of Vancomycin, see chapter (7), are run within the microcanonical ensemble of constant particle number, N, volume, V, and energy, E. The microcanonical ensemble corresponds to an isolated system; there is no need for external, random input to determine whether a step in the evolution of the system is acceptable or not within the ensemble.

Other ensembles include the canonical (constant N, V and temperature, T), the isobaric-isothermal (constant N, pressure, P, and T) and the grand canonical (constant chemical potential, μ, V and T). These ensembles require some interaction with an 'environment' in the form of thermostats, barostats and particle reservoirs.

3.5 Calculating trajectories

In molecular dynamics the positions of the particles subsequent to the initial positions are obtained by numerically solving the equations of motion. This means the positions are temporally connected, unlike in other, stochastic, methods of simulation [96].

The Verlet algorithm, as described below, is one of the most simple but often most effective ways to integrate Newton's equations of motion. Other algorithms exist, but since the one I shall be using is an extension of the Verlet scheme, I am focusing solely on that in this document.

We start with Taylor expansions of the positions of a particle around time, t,

$$\mathbf{r}(t+\Delta t) = \mathbf{r}(t) + \frac{d\mathbf{r}(t)}{dt}\Delta t + \frac{1}{2}\frac{d^2\mathbf{r}(t)}{dt^2}\Delta t^2 + \frac{1}{3!}\frac{d^3\mathbf{r}(t)}{dt^3}\Delta t^3 + \mathcal{O}(\Delta t^4)\ldots \quad (3.5.1)$$

or,

$$\mathbf{r}(t+\Delta t) = \mathbf{r}(t) + \mathbf{v}(t)\Delta t + \frac{1}{2}\frac{\mathbf{f}(t)}{m}\Delta t^2 + \frac{1}{3!}\frac{d^3\mathbf{r}(t)}{dt^3}\Delta t^3 + \mathcal{O}(\Delta t^4)\ldots \quad (3.5.2)$$

and,

$$\mathbf{r}(t-\Delta t) = \mathbf{r}(t) - \mathbf{v}(t)\Delta t + \frac{1}{2}\frac{\mathbf{f}(t)}{m}\Delta t^2 - \frac{1}{3!}\frac{d^3\mathbf{r}(t)}{dt^3}\Delta t^3 + \mathcal{O}(\Delta t^4)\ldots. \quad (3.5.3)$$

Summing these two eliminates all odd-order terms, leaving

$$\mathbf{r}(t+\Delta t) + \mathbf{r}(t-\Delta t) = 2\mathbf{r}(t) + \frac{\mathbf{f}(t)}{m}\Delta t^2 + \mathcal{O}(\Delta t^4)\ldots, \quad (3.5.4)$$

or, ignoring higher order terms,

$$\mathbf{r}(t+\Delta t) \simeq 2\mathbf{r}(t) - \mathbf{r}(t-\Delta t) + \frac{\mathbf{f}(t)}{m}\Delta t^2. \tag{3.5.5}$$

So we have computed the new positions of the particles without explicitly including the velocity. Velocities are not necessary for time evolution, but we need them to calculate kinetic energy, and in turn monitor conservation of energy in the system. Values can be assigned from the above Verlet scheme using,

$$\mathbf{r}(t+\Delta t) - \mathbf{r}(t-\Delta t) = 2\mathbf{v}(t)\Delta t + \mathcal{O}\Delta t^3 \ldots \tag{3.5.6}$$

which gives

$$\mathbf{v}(t) = \frac{\mathbf{r}(t+\Delta t) - \mathbf{r}(t-\Delta t)}{2\Delta t} + \mathcal{O}\Delta t^2 \ldots. \tag{3.5.7}$$

An extension of the classic Verlet algorithm, the Velocity Verlet, explicitly treats the velocity as well which allows us to start a simulation from initial positions and velocities at the same time and to calculate kinetic energy at every step. It is this scheme that is used in my simulations in DL POLY 2.19 [97], and consequently in the work described in this thesis.

For the Velocity Verlet algorithm we begin by defining the velocity at the half timestep from the properties of each particle at the current time, t, as

$$\mathbf{v}(t+\frac{1}{2}\Delta t) \simeq \mathbf{v}(t) + \frac{1}{2}\Delta t\frac{\mathbf{f}(t)}{m}. \tag{3.5.8}$$

Using this velocity to define the new position of each particle as,

$$\mathbf{r}(t+\Delta t) \simeq \mathbf{r}(t) + \Delta t\mathbf{v}(t+\frac{1}{2}\Delta t), \tag{3.5.9}$$

from which the forces, $\mathbf{f}(t+\Delta t)$, are obtained and can be used to calculate the full step velocity as,

$$\mathbf{v}(t+\Delta t) \simeq \mathbf{v}(t+\frac{1}{2}\Delta t) + \frac{1}{2}\Delta t\frac{\mathbf{f}(t+\Delta t)}{m}. \tag{3.5.10}$$

The length of the timestep must be chosen so as to satisfactorily represent

the highest frequency motion of the system. In many cases, for proteins, this is the C-H stretching mode, which has a wavenumber of ~ 2900 cm^{-1} which corresponds to a frequency of $\sim 1 \times 10^{-14}$ s. Within this body of work all simulations are run using a timestep of 1fs, an order of magnitude smaller than the period of the C-H stretch, satisfying the assumption, used in the Velocity Verlet algorithm, that velocity and acceleration are constant over one timestep.

3.6 Equilibration

Before what is known as the production run, when statistics relating to the system are gathered, it is important to equilibrate the system. This ensures that any anomalously high forces due to the initial positioning of atoms, for example due to proximity leading to unfeasibly high van der Waals or coulombic interactions, can be accounted for. The atomic velocities are scaled during this period of the simulation to keep the system temperature close to the specified value in spite of the potentially high forces.

Plotting the thermodynamic properties of the system is a way of assuring an equilibrium is reached; the potential and kinetic energies etc. should fluctuate around an average value that does not drift over time.

3.7 Potential of mean force

Analysis of the system as a whole from molecular dynamics simulation outputs involves taking these individual trajectories and using them to evaluate macroscopic properties.

One way of building a global interaction force curve for the Vancomycin-fragment complex system that allows for the effects of entropy is through calculations of the potential of mean force (PMF). The PMF is defined as that potential which describes, as a function of one of the reaction coordinates in a system, the average force between all configurations of those particles comprising the system.

The algorithm that lets us calculate the PMF is an extension of that for imposing constraints between bonded atoms. The bond constraint algorithm initially calculates the new positions of all the atoms in the system considering it to be under no imposed constraints. It then uses the amount by which a constraint tolerance has been exceeded to calculate the force necessary to bring the specified bond length into line. This correcting force is then applied to the system, to give a new set of atomic positions.

In a system with more than two atoms, the conservation of the constraints is often an iterative process, as the act of correcting one bond can throw out another.

The tolerance for bondlength conservation can be defined by the user; in this work I require the PMF constraint distance to be maintained to within 10^{-5} Å.

In the case of PMF calculations, the force needed to constrain the system is the value of real interest. If the specified constraint is the separation along a single reaction coordinate of the system, this force is the negative sum of all the interaction forces at that point along the coordinate. In this way it is possible to find the mean force of interaction of two Vancomycin-fragment complexes, F_{PMF}, as a function of their separation, from the constraint virial as,

$$F_{PMF} = \frac{W_{PMF}}{d_{PMF}}, \tag{3.7.1}$$

where W_{PMF} is the constraint virial and d_{PMF} the constrained distance. This function can then be integrated with respect to the separation to give the potential of mean force which is a representation of the free energy of interaction of the two complexes.

Since the model that I develop in this thesis is based around equating those opposing forces on a cantilever-adsorbate system at equilibrium, the quantity I will be taking and analysing from the simulations is the mean force of interaction between analytes, F_{PMF}.

Chapter 4

Experimental motivation

The dire need to understand the process of bacterial resistance and to move towards replacing Vancomycin in the global health market has driven research around this drug. The 2008 study mentioned in the introduction [15], into the antibiotic action of Vancomycin, looked to quantify the binding efficiency to both sensitive and resistant bacterial cell-wall mucopeptide analogues.

The study used arrays of eight rectangular cantilevers measuring $500 : 100 : 0.9$ μm, with a silicon substrate, coated in a thin film of Au. The Au coating is employed to make advantageous use of thiol-Au chemical bonding when functionalising the cantilevers with biochemically specific surface layers and to enhance reflectivity of the cantilever surface when using the optical lever technique to take measurements.

In this case three specific layers were used. One, a self-assembled monolayer of antibiotic sensitive mucopeptide analogue, of chemical make-up $HS(CH_2)_{11}$ $(OCH_2CH_2)_3O(CH_2)(CO)NH(CH_2)_5(CO)$-L-Lys-($\epsilon$-Ac)-D-Ala-D-Ala, herein referred to as D-Ala.

The second, a similar SAM, but with the mutation, the exchange of an amide linker for an ester, that leads to antibiotic resistance. These mucopeptides have chemical make-up $HS(CH_2)_{11}$
$(OCH_2CH_2)_3O(CH_2)(CO)NH(CH_2)_5(CO)$-L-Lys-($\epsilon$-Ac)-D-Ala-D-Lac and will

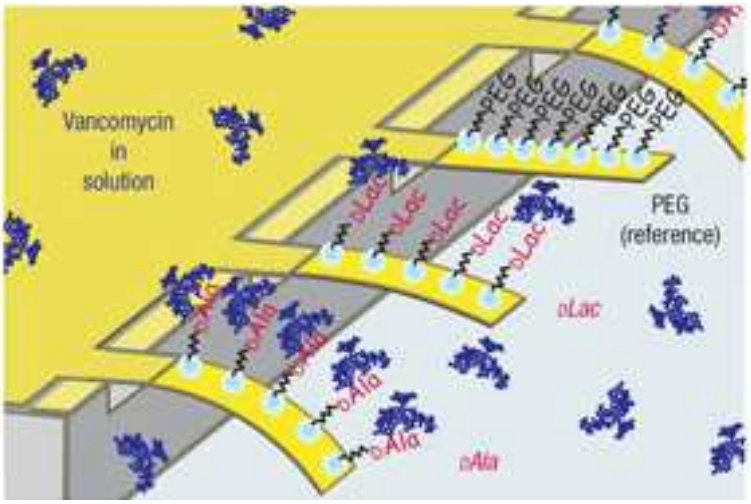

Figure 4.0.1: Representation of the specific response of D-Ala coated cantilevers to Vancomycin; also showing D-Lac and the reference PEG coated cantilevers in the array. Figure modified from that in [15] with permission from Macmillan Publishers Ltd.

be herein referred to as D-Lac.

Finally, to act as a reference coating in order to obtain differential, rather than absolute measurements, a passivating SAM of triethylene glycol, which should resist adsorption of the antibiotic, and indeed any biomolecules [98, 99]. Its chemical make-up is $HS(CH_2)_{11}(OCH_2CH_2)_3OH$ and it will be referred to herein as PEG.

The influx of different buffer and serum solutions and varying concentrations of Vancomycin (from 10 nM - 1 mM) was controlled using a specially built gravity flow system. Measurements of cantilever deflection were taken using a time-multiplexed optical detection system, with the laser spot focused at the free end of the cantilever and converted to surface stress values using Stoney's equation (2.3.1) with a biaxial Young's modulus for Au-Si of 180 GPa [15].

Figure (4.0.2) shows the absolute and differential deflection signals induced by Vancomycin-mucopeptide interactions on the cantilever arrays; the negative sign corresponding to a downwards deflection due to a compressive surface stress

on the upper surface of the cantilever.

The measurements showed significant differences in deflection and therefore stress between the antibiotic-sensitive and resistant peptide coated cantilevers. For example the average values across all arrays of -34.2 ± 5.9 mNm^{-1} and -3.8 ± 1.5 mNm^{-1} for D-Ala and D-Lac respectively, upon injection of 250 μM Vancomycin in sodium phosphate buffer (pH 7.4, 0.1 M).

Measurements were also taken in serum (a mixture of fetal calf serum with buffer at a ratio of 9:1) in order to ascertain the sensitivity of a nanocantilever response to clinically relevant concentrations of $3 - 27$ μM Vancomycin in a biologically relevant medium. A differential bending signal of 105 ± 4 nm was demonstrated for D-Ala at 7 μM Vancomycin.

These results are an extremely encouraging indication that cantilever sensors are able to distinguish quantitatively between two different analyte-target events, in this case corresponding to simply the deletion of a single hydrogen bond in the peptide-antibiotic complex, and able to make measurements in clinically relevant setups.

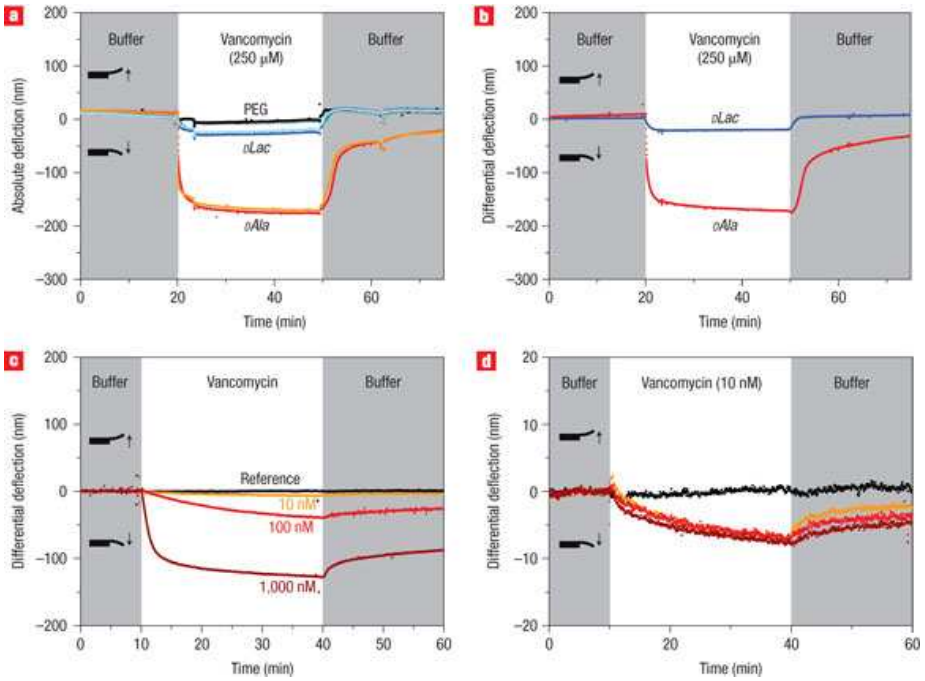

Figure 4.0.2: Deflection responses for different concentrations of Vancomycin, for antibiotic-sensitive; antibiotic-resistant; and 'inert' SAM coated cantilevers. (a) Absolute deflection signal to 250 μM of Vancomycin. (b) Corresponding differential deflections, once corrected for the in-situ PEG reference values. (c) Differential signals for D-Ala to 10, 100 and 1000 nM Vancomycin concentrations. (d) Closer look at the response to 10 nM of Vancomycin for the three D-Ala coated cantilevers in one array. Reproduced courtesy of [15] with permission from Macmillan Publishers Ltd.

4.1 Exploring connectivity

Since our knowledge of the method by which biochemical events induce a surface stress that leads to the beam's deflection is still incomplete, investigation was also made into how varying the coverage of the active, underlying peptide affects the stress response at different concentrations of Vancomycin.

Cantilevers were coated with mixed monolayers of sensitive D-Ala peptides and inert PEG peptides. The systematic variation of the coverage of the active peptides, p, on the surface was determined by X-ray photoelectron spectroscopy

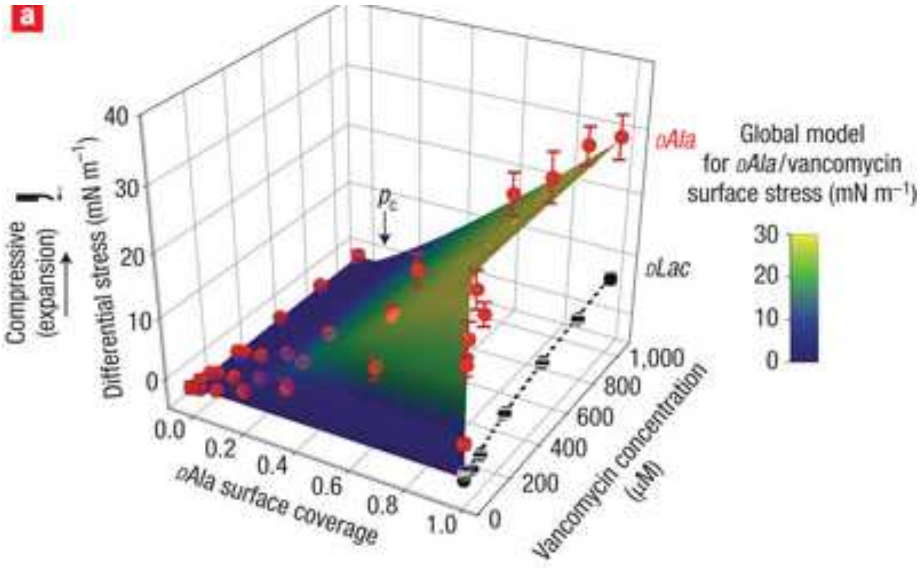

Figure 4.1.1: Graph showing the measured differential surface stress response for D-Ala- (red circles) and D-Lac- (black circles) coated cantilevers as a function of Vancomycin concentration in solution and D-Ala surface coverage, superimposed with the results of a global fit according to equation (4.1.1). Reproduced courtesy of [15] with permission from Macmillan Publishers Ltd.

(XPS). Where p = 0 corresponds to no D-Ala peptides, or a complete PEG monolayer, and p = 1 to a complete D-Ala monolayer. These mixed monolayer covered cantilevers were then exposed to different concentrations of Vancomycin, from $0-1000$ μM. Figure (4.1.1) shows a saturation of the stress response above 50 μM for a cantilever with a full D-Ala monolayer, above which the system has reached its binding equilibrium and most accessible binding sites on the monolayer are filled.

What is really interesting about figure (4.1.1), and what leads into the work I shall be discussing in the remainder of this chapter, is that, regardless of concentration of Vancomycin, there is no deflection response for an active peptide coverage of $p < 0.1$, from where the response increases approximately linearly. So a certain fraction of the cantilever must be subject to the specific chemical

events before a response is triggered. This suggests that a minimum degree of connectivity between those individual events is necessary; that the transduction of surface stress is actually a collective phenomenon.

In the 2008 paper, the first suggestion was made that the coverage fraction of chemical events on a sensor's surface must reach a 'percolation threshold' before eliciting a signal. In fact, that with knowledge of the maximum surface stress when all available binding sites are occupied, a, the cantilever's stress response can be deconvoluted into a chemical factor, based on a Langmuir adsorption isotherm, and a geometric factor, that follows a power law and represents the connective nature of the elastic response,

$$\Delta\sigma_{eq} = \frac{a\,[\mathrm{Van}]}{K_d + [\mathrm{Van}]} \left(\frac{\mathrm{p} - \mathrm{p}_c}{1 - \mathrm{p}_c}\right)^{\alpha}, \tag{4.1.1}$$

where a is the maximum surface stress signal, [Van] is Vancomycin concentration and K_d is the equilibrium dissociation constant on the surface of the cantilever.

Before exploring the geometric dependence of stress on chemical events on the cantilever's surface, it is necessary to gain an understanding of the origins of said stress. The various interactions of adsorbates that may contribute to a differential surface stress are explored in the next chapter for the formation of a monolayer of decanethiol. Since the model monolayer is full, any geometric dependence on coverage is irrelevant for these initial investigations. The chapter aims to quantify the contributions from both adsorbate-adsorbate and adsorbate-substrate interactions.

Chapter 5

Origins of surface stress

While there is much evidence in the literature of monolayer formation of many species, on varied substrates, causing a change in surface stress [100, 54, 101, 102, 103, 104, 32], the origins of said stress are still under question.

Simple intuition would suggest that the cause of the increased surface stress on adsorption should be a combination of interactions between the adsorbates themselves and interactions between the adsorbed species and the substrate atoms at the surface of the beam.

To investigate the validity of this assumption I will discuss approximate values for the various contributions for a model system of a self-assembled monolayer of decanethiol molecules adsorbed onto an Au coated cantilever. I chose decanethiol as a model system in this case as it is a relatively simple molecule which forms stable, ordered monolayers that are reasonably well-studied and documented [105] and there are several reported experimental values for decanethiol induced differential surface stress in the literature [106, 56, 107, 108], against which I can compare any theoretical values obtained.

5.1 Adsorbate-adsorbate interactions

To model the interactions between two adjacent adsorbed molecules I use the Lennard-Jones intermolecular pair potential. The repulsive part of this standard potential model represents the short-ranged steric repulsion due to electron cloud overlap upon close approach of two molecules, often viewed as a simple hard-sphere repulsion. In a Lennard Jones potential we adopt an inverse power law representation with a power of 12, to more realistically mirror the finite compressibility of atoms. The power law potential between two molecules, i and j, can be written as

$$U(r_{ij}) = A\left(\frac{\sigma}{r_{ij}}\right)^{12}, \tag{5.1.1}$$

where σ is the hard sphere diameter of the molecule, r_{ij} their separation and A an energy term. The attractive part of the potential is composed of three contributions due to angle-averaged dipole-dipole interactions (Keesom interaction), dipole-induced dipole interactions (Debye or induction interaction) and instantaneous dipole interactions (London or dispersion interactions) [109]. These three separate contributions to the van der Waals attraction between two similar molecules are defined as:

$$Keesom\ interaction:\ U(r_{ij}) = -\frac{\mu_i^2\mu_j^2}{3(4\pi\epsilon\epsilon_0)^2 kT r_{ij}^6}, \tag{5.1.2}$$

$$Debye\ interaction:\ U(r_{ij}) = -\frac{(\mu_i^2\alpha_j + \mu_j^2\alpha_i)}{(4\pi\epsilon\epsilon_0)^2 r_{ij}^6}, \tag{5.1.3}$$

$$London\ interaction:\ U(r_{ij}) = -\frac{3}{4}\frac{\alpha_i\alpha_j I}{(4\pi\epsilon_0)^2 r_{ij}^6}, \tag{5.1.4}$$

where μ_i is the dipole moment of the ith molecule, ϵ_0 and ϵ the permittivity of free space and the relative permittivity of the medium respectively, I is the ionisation potential, α_i the electronic polarisability of the ith molecule, k is the Boltzmann constant and T the temperature. These three expressions, in conjunction with the repulsive term above, are combined in the well-known

Lennard-Jones expression for intermolecular interaction of:

$$U(r_{ij}) = 4\varepsilon \left(\left(\frac{\sigma}{r_{ij}} \right)^{12} - \left(\frac{\sigma}{r_{ij}} \right)^{6} \right), \tag{5.1.5}$$

where ε is the well depth of the resultant interaction energy curve.

Because the molecules comprising the monolayer are spatially fixed, to an extent, it can be necessary to also consider a dipole-dipole interaction that is not angle-averaged, where the arrangement of partial charges on a molecule confers an intrinsic dipole moment. The resulting interaction can be described as,

$$U(r_{ij}, \theta_1, \theta_2, \phi) = -\frac{\mu_i \mu_j}{4\pi\epsilon_0 \epsilon r_{ij}^3} \left[2cos(\theta_1)cos(\theta_2) - sin(\theta_1)sin(\theta_2)cos(\phi) \right], \tag{5.1.6}$$

where μ_i is the dipole moment of molecule i, ϵ_0 is the permittivity of free space, ϵ the relative permittivity of the medium and θ_1, θ_2 and ϕ describe the relative orientations of the two dipoles. Their relative orientations obviously affect both the sign and magnitude of the interaction energy.

5.2 Adsorbate-substrate interactions

During the process of chemisorption, the formation of a covalent bond between the adsorbate head and surface atoms of the substrate involves a transfer of charge. This can result in an effective dipole corresponding to each adsorbate site, as the partial charge on the adatom is mirrored by its inverse charge on the surface of the substrate. In a monolayer consisting of only one type of adsorbate the dipoles are arranged with like charges in plane and thus are always repulsive. For the cases where the dipoles are parallel to one another the above expression for the dipole-dipole interaction energy reduces to,

$$U(r_{ij}, \theta_1, \theta_2, \phi) = -\frac{\mu_i \mu_j}{4\pi\epsilon_0 \epsilon r_{ij}^3}. \tag{5.2.1}$$

Adsorption onto a surface, with its associated charge transfer, also changes

the bonding configuration of those atoms at the substrate surface.

Clean metal surfaces, with no adsorbates, exhibit a tensile surface stress. This is presented as being the result of redistribution of electronic charge around the atoms comprising the metal surface layers [110]. At the surface of a solid the co-ordination of atoms differs from that of atoms in the material's bulk, this changes the nature of the bonding between surface atoms and therefore their interatomic distances. In the case of transition metals such as Au, Ibach [111] qualitatively describes the charge redistribution as being the shift of charge that would have been involved in bond formation to the now missing bulk neighbours to the interatomic spaces between the surface atoms, demonstrated pictorially in figure (5.2.1). As such, the attractive interaction between the surface atoms will increase and a tensile, or contractive, surface stress will be induced.

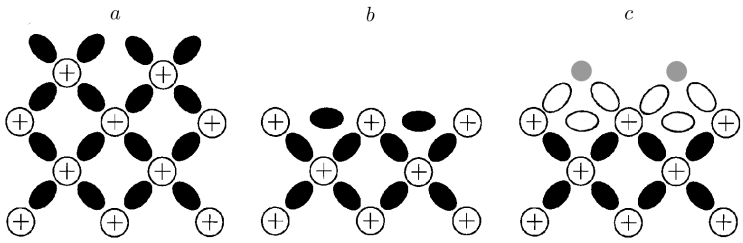

Figure 5.2.1: Outlining the organisation of charge between metal atoms in (a) bulk material, (b) at a clean surface and (c) at a surface in the presence of adsorbates.

Upon adsorption of an analyte the charge distribution will change again. The adsorption of electron donors will lead to an increase of the bond charge between the metal surface atoms and electron acceptors reduce the surface electron density, thereby leading to a more tensile stress or a release of the intrinsic tensile stress respectively.

The contributions from all these consequences of adsorption combine to produce a force, tensile or compressive, in the plane of the cantilever's surface. The degree to which the cantilever will bend upon adsorption depends both upon

the magnitude of these forces and the magnitude of the corresponding elastic restoring force in the beam.

5.3 The elastic response

In investigating the response of a cantilever beam to surface stress it is important to look both at the interactions inducing the stress, and at the continuum elastic response of the cantilever itself to the stress. In this chapter I derive analytical expressions for the strain energy of a bent beam and its relation to deflection, curvature and stress with a view to reproducing and predicting a cantilever response.

5.3.1 A simple beam under pure bending

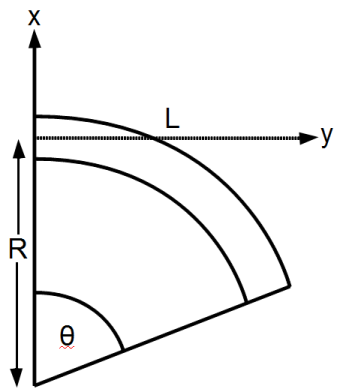

Figure 5.3.1: Schematic showing the axes and dimensions of a beam undergoing pure bending.

We have a cantilever beam of length L, thickness h and width b, as in figure (5.3.1). Consider a volume element X at a height x above the neutral plane of the beam, which falls at $\frac{h}{2}$. The beam is bent such that the angle of curvature is

θ and the neutral plane lies on a radius of curvature R. Element X will have an initial length of $L = R\theta$ and an increased length post-bending of $L_X = (R+x)\theta$. So, during bending, the element X has been stretched through an elongation of $x\theta$. (Were the element to have been chosen as lying below the neutral plane it would undergo compressive rather than tensile stretching and this elongation would be negative.)

The strain associated with this elongation is

$$\epsilon_X = \frac{x\theta}{L}. \tag{5.3.1}$$

Thus, the strain energy per unit volume for our chosen volume element X is

$$\frac{U_{st_X}}{V_X} = \frac{1}{2}E'{\epsilon_X}^2 = \frac{E'x^2\theta^2}{2L^2}, \tag{5.3.2}$$

with $E' = \frac{E}{1-\nu}$, where E is the Young's modulus of elasticity of the beam material and ν its Poisson ratio.

If the thickness of this volume element is dx then its volume is simply $V_X = L.b.dx$ so we can write the strain energy for element X as

$$U_{st_X} = \frac{E'x^2\theta^2 b dx}{2L}. \tag{5.3.3}$$

So, in order to find the strain energy due to the bending for the whole beam, we need to integrate this expression over the full thickness.

$$U_{st} = \int_{-\frac{h}{2}}^{\frac{h}{2}} \frac{E'x^2\theta^2 b}{2L} dx, \tag{5.3.4}$$

$$U_{st} = \left[\frac{E'x^3\theta^2 b}{6L}\right]_{-\frac{h}{2}}^{\frac{h}{2}} = \frac{E'b\theta^2 h^3}{24L}, \tag{5.3.5}$$

which, if we take $R = L/\theta$, we can write as,

$$U_{st} = \frac{E'bLh^3}{24R^2}. \tag{5.3.6}$$

Equated to the contributions to the increase in surface energy described in the previous sections, this gives an expression for the total energy of the cantilever-adsorbate system of

$$U_{tot} = U_{ads-ads} + U_{ads-sub} + U_{st}. \tag{5.3.7}$$

5.4 Calculating a stress

By virtue of the fact that $r = a(1 + \frac{h/2}{R})$, where h is the thickness of the cantilever, an expression for each contribution to the total forces on the surface of the cantilever can also be written in terms of the initial, pre-deformation, separation of adsorbed atoms, a, and the radius of curvature, R, associated with the increase/decrease in separation due to the various interactions.

The value of a obviously varies to some extent across adsorbate species; in most cases reasonably accurate values can be found in the literature. To convert the system specific a into that set of pairwise distances that come from the arrangement of adsorbates across a cantilever's surface and dictate the sum of forces due to adsorption I have written a model in Mathematica 8.0 [25], herein referred to as the lattice model.

The lattice model works simply by generating an array of points to represent the individual sites of adsorption, the coordinates of which correspond to the coordination (hexagonal, honeycomb, square etc) of the monolayer in question, spaced according to a for the particular adsorbate.

Coverage of the 'adsorbates' on this theoretical representation of the cantilever is controlled by assignation of one or zero, populated or vacant respectively, to each member of the lattice array.

In equilibrium, there will be no net force on the beam. So, differentiating equation (5.3.7) with respect to the radius of curvature, R, and setting equal to zero, we can solve for R.

As we have the elastic restoring force of the cantilever already in terms of the radius of curvature, we can equate them to give,

$$F_{tot}(R) = F_{ads-ads}(R) + F_{ads-sub}(R) + \frac{E'bh^3L}{12R^3} = 0, \tag{5.4.1}$$

where $F_{ads-ads}$ and $F_{ads-sub}$ are the forces due to the interadsorbate interactions and the adsorbate-substrate interactions respectively.

Once a value for R is established, it gives us a corresponding value for the angle of curvature and, as can be shown from the schematic in figure (5.3.1), the deflection, δz, of the beam, which is obtained using

$$\delta z = R(1 - cos(\theta)). \tag{5.4.2}$$

Using this result, with the known geometric and material properties of the cantilever we can use Stoney's equation (2.3.8) to estimate the value of the surface stress induced by a specific system. Knowing that the radius of curvature of the cantilever can be approximated as $R = \frac{L^2}{2\delta z}$ enables us to rewrite (2.3.8) in terms of the deflection of the free end of the beam, δz, as

$$\Delta\sigma = \frac{1}{3}\frac{E}{(1-\nu)}\frac{t^2}{L^2}\delta z.$$

As an example here, the next sections will look specifically at the system of a decanethiol monolayer. I will perform these calculations for a full monolayer of decanethiol, so in the lattice model each member of the array will be assigned the value of one, corresponding to an occupied adsorption site on the cantilever.

The lattice model I designed in Mathematica [25] is used to calculate all contributions to equation (5.4.1) for the particular specifications of decanethiol, as detailed in the following sections. The restrictions on the size of lists that can be manipulated, imposed by the memory limitations of the computer used to perform the calculations, meant that the inter-event distances were calculated from a model lattice of 2000 sites. In comparison to an actual cantilever which, for molecules of decanethiol's size, can hold of the order of 10^{11} molecules, the edge effects will be more significant. As those molecules at the edges are of a lower coordination, this will manifest as an underestimation of the overall stress

response.

5.5 Alkanethiol monolayer

Alkanethiols, apart perhaps from methanethiol about which there is much discussion in the literature [112, 113, 114, 115] and which is a point of some contention, readily adsorb from either gas or liquid phase onto an Au surface [116, 117, 118, 119]. Alkanethiols consist of a thiol head group, which takes advantage of the stable covalent bond formation between S and Au to anchor the molecules, a carbon chain which can be varied in length, and a terminating, or tail, group that can be chosen in order to target specific binding proteins or chemical reactions [120, 121, 122, 123, 124, 125, 126, 127] or to give the monolayer different properties. For example an alkanethiol monolayer terminating in CH_3 will be hydrophobic and anti-fouling, whereas an OH terminating SAM will be hydrophilic and demonstrate a good binding affinity to proteins [116]. They are relatively simple to prepare and form stable, reasonably well understood monolayers, making them very attractive to the nanodevices industry.
On a (1×1) Au(111) surface with interatomic separation of 0.29 nm, alkanethiols with long carbon chains will generally form a $(\sqrt{3} \times \sqrt{3})R30°$ lattice, corresponding to a sulphur separation of 0.499 nm and a chain tilt angle of 30° away from the surface normal.

At room temperature, alkanethiols with less than six carbons have been shown to preferentially form a $c(4 \times 2)$ superlattice [128]. Exact details of this structure are disputed in the literature [129, 130, 131], but may involve much smaller S separations [132], where the orientation of the headgroup S-C bond is altered to compensate to hexagonal close-packing of the chains. As I'm making comparison with experimental results for chain lengths greater than this, I will be performing calculations based on a straight $(\sqrt{3} \times \sqrt{3})R30°$ lattice, which dominates for the longer alkanethiols, and is explained diagrammatically in figure (5.5.1).

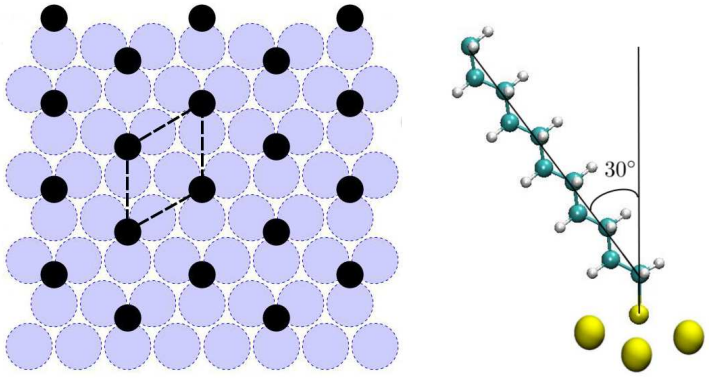

Figure 5.5.1: Showing the $(\sqrt{3} \times \sqrt{3})R30°$ lattice formed by alkanethiol molecules on the Au (111) surface, where the Au atoms are represented by the large blue circles and the S atom at the head of the alkanethiol by the smaller black circles, and the tilt of 30° reportedly due to the van der Waals interactions between adjacent chains.

The thiols initially physisorb at terrace edges and defects and then across the Au surface. The S-H head of the alkanethiol will then undergo bond scission in order to chemisorb to the Au atoms. The exact adsorption sites on the surface are still under discussion, with investigations in the literature debating suggestions including hollow [133, 134], bridge [113, 135] and atop sites [136, 137], and combinations of all three [105, 118].

They initially adsorb into a lying down configuration at low densities, until denser areas on the gold surface form which can nucleate into vertically configured, or 'standing', domains, from which a full, well-ordered monolayer can form [105] at a coverage of ~ 0.33 ML. In reality, on an Au surface, the monolayer will never be truly 'full' due to the well documented [116] formation of etch pits and vacancy islands, but that should just translate to the theoretical values here slightly overestimating the response as they assume a complete, flat monolayer covering the entire surface.

Atom	$\frac{q}{e}$	σ (Å)	ε $(kJmol^{-1})$
S(SH)	-0.45	3.550	0.250
CH_2(CSH)	0.18	3.905	0.118
CH_2	0.00	3.905	0.118
CH_3	0.00	3.905	0.175

Table 5.6.1: OPLS parameters from the liquid phase, taken from Fartaria et al [138].

5.6 Stresses for decanethiol

Adsorbate-adsorbate interactions

For decanethiol, using known literature values for the constituent atoms [138] which can be seen in table (5.6.1), and using the Lorentz-Berthelot combination rules for unlike atomic types, $\sigma_{ij} = (\sigma_{ii} + \sigma_{jj})/2$ and $\varepsilon_{ij} = \sqrt{\varepsilon_{ii}\varepsilon_{jj}}$, the molecular interaction Lennard-Jones potential can be well estimated by summing all intermolecular pairwise interactions of the individual atoms and including the dipole-dipole interaction of $\mu \approx 1.6\ De$ [139] for decanethiol. The separations of the atoms between each pair are calculated using literature values of C-C, C-S and C-H bond lengths and angles [140].

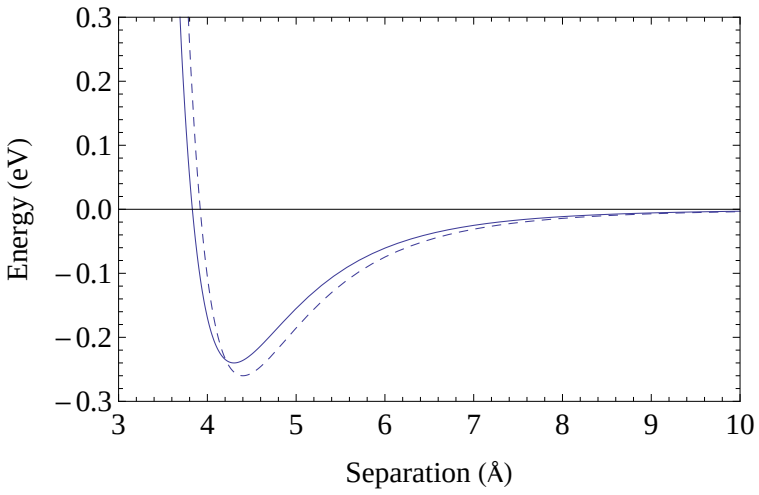

Figure 5.6.1: Interaction potential between two decanethiol molecules as calculated by summation of pairwise atomic Lennard-Jones interactions and dipole-dipole repulsion. The potential as calculated (continuous line) is compared with Pertsin et al's [141] calculated potential (dashed line).

The resulting interaction curve for two decanethiol molecules can be seen in figure (5.6.1), which gives a well depth of $\varepsilon = 0.24$ eV and an equilibrium separation of $r_{min} = 4.30$ Å, which are comparable with previously calculated literature values of 0.26 eV and 4.40 Å as obtained by Pertsin et al [141]. It is well documented [105, 116] that a full, ordered monolayer of long chain alkanethiol molecules adsorbs onto an Au (111) surface into a $(\sqrt{3} \times \sqrt{3})R30°$ lattice, which translates to a S-S distance of 4.99 Å. As this is a considerably larger separation than the equilibrium separation of the Lennard-Jones potential for decanethiol, this would suggest a contraction of the surface layer of the cantilever were the alkanethiols interacting in an upright, parallel attitude, leading to a tensile surface stress. However, experimental values of absolute surface stress due to alkanethiol monolayer formation are compressive suggesting that the interchain decanethiol interaction is not responsible for the surface stress transduction. A tilt of 30° is observed in full alkanethiol monolayers [118, 142, 143, 144], bringing the majority of the adsorbed chains within the proximity dictated by

the Lennard-Jones potential [145].

The sulphur atoms on the surface are not explicitly fixed, in a number of scenarios they have been reported to diffuse upon the Au surface [146, 147]. Were the chain-chain interaction exerting a significant force pulling the alkanethiols towards one another there is no reason why they wouldn't adopt a closer packed lattice upon formation of the monolayer. In fact, given the uncertainty over where the S atoms prefer to chemisorb, there appear to be hexagonal lattice opportunities at S separations of 4.35 and 4.43 Å that are commensurate with the underlying Au surface.

Consequently, I will assume that, in the case of these monolayers, the direct intermolecular interaction does not significantly contribute to the observed change in surface stress.

Adsorbate-substrate interactions

Gold is often used to coat cantilevers due to the stability afforded by the covalent bonding of thiols to Au. This process results in a polar bond, with the electron density shifted more towards the sulphur atom. Density functional theory calculations performed on alkanethiols adsorbed onto gold report [148, 149] a charge transfer of $0.2e$ onto the sulphur atom, where e is the electronic charge, 1.6×10^{-19} C. Bearing this in mind and taking the S-Au distance as 0.24 nm, an average value of those reported in the literature separately by [137, 150, 151, 152, 114], this charge transfer can be represented as a electric dipole, normal to the cantilever surface, of $q = 0.2e$ and $d = 0.24$ nm sitting at the site of each adsorbate-substrate bond.

Assuming a density of bond dipoles dictated by sulphur separations and an hexagonally close-packed monolayer results in a compressive stress of ~ -0.14 Nm^{-1} due to dipole-dipole interactions.

There are various literature values for the tensile surface stress on a clean Au(111) surface with no adsorbates, that vary somewhat in magnitude, but correspond qualitatively. First principles calculations have presented a value

of 2.77 Nm^{-1} [153] in comparison with 1.51 Nm^{-1} for semi-empirical methods [154]. While it is extremely difficult to determine experimentally the surface stress of a solid, some experimental work has been performed, observing the lattice contraction of small particles, yielding stress values of 1.18 Nm^{-1} [155] and 1.54 Nm^{-1} [156] for an Au(111) surface. The mechanism by which this relates to adsorbate induced surface stress as we are considering it is as follows. The initial deflection of an Au(111) coated cantilever, whether under a tensile stress of its own or not, is taken as the zero baseline. When molecules chemisorb to the Au surface, some of that redistributed charge that is causing the attractive Au surface atom interaction is once again shifted away from the bulk, to form the covalent bond between Au and adsorbate head group. This relieves the intrinsic tensile surface stress associated with the clean Au(111) surface, which, taken from the pre-adsorption zero baseline, would register as a compressive surface stress. So, depending on the initial state of the Au surface, an amount of this intrinsic stress will be relieved by the presence of the electronegative S atoms, effectively adding to the compressive stress due to the dipole-dipole interactions.

5.7 Comparison with experiment

Source	σ Nm^{-1}
Model	-0.14 +
Berger et al [56]	-0.15
Desikan et al [107]	-0.14
Shrotriya et al [108]	-0.15
Hanson et al [100]	-0.25/-0.8
Godin et al [106]	-0.51/-15.9

Table 5.7.1: Table showing calculated values of surface stress for a decanethiol monolayer as a resultant stress to be compared with literature values.

In most situations a theoretical value for total surface stress predominantly derived from the Au-S bond dipole interactions appears to agree quantitatively

with the values from the literature for the stress of alkanethiol monolayer formation on cantilevers, listed in table (5.7.1). The results are all for the adsorption of either hexanethiol, decanethiol or dodecanethiol, which, given that the chain interaction can be neglected, are of a reasonable similarity of length to be compared.

The stand-out values in table (5.7.1) are the larger value from Hanson et al [100] and both values from Godin et al [106]. These differences in magnitude can only be speculated on at present, but there are some complementary ideas in the literature. I suggest that the variation in the magnitude of observed stresses may be dependent on the release of the tensile stress intrinsic in the Au surface, to varying degrees.

The amount to which this effect contributes to the measured compressive surface stress, in each individual experiment, depends upon the state of the Au surface when the zero baseline calibration is made. If the Au surface is clean to begin with there will be an increased observed stress due to the release of the intrinsic tensile stress. If, however, the Au surface has contaminants adsorbed on it, those contaminants may already have relieved the clean Au stress to an extent, and the adsorption of the monolayer molecules will simply displace the contaminants [157], resulting in a lower measured compressive stress overall. Alkanethiols have a high affinity for Au, and can displace contaminants [158].

Indeed, in the work of Hansen et al [100], the values for the surface stress of alkanethiol formation on an Au(111) surface, which can be seen in table (5.7.1) are for different methods of pre-measurement cleaning. The higher stress of -0.8 Nm^{-1} corresponds to cantilevers cleaned with Aqua Regia (a mixture of hydrochloric acid and nitric acid), whereas the lower stress of -0.25 Nm^{-1} is for cantilevers either cleaned with the less effective oxygen plasma method and for those left exposed to an ambient air environment for up to 19 days prior to adsorption.

The values for surface stress obtained by Godin et al [106] were taken from measurements made within a few hours of the Au layer being evaporated onto the cantilever, which would, one can assume, provide a clean surface for ad-

sorption, giving a relatively high $\sigma = -0.5$ Nm^{-1} value for small grained Au. They also investigated the effect of ambient adsorbates by exposing Au covered cantilevers to the lab environment for a week, after which time they measured a compressive surface stress of ≈ -0.13 Nm^{-1} on small grained Au. Although Au's chemical inertness means it stays cleaner than some surfaces, X-ray photoelectron spectroscopy (XPS) measurements revealed the presence of contaminants including C and O on the surface of the exposed cantilevers. While Godin suggested that these findings indicate an increased difficulty in displacing contaminants after prolonged exposure to air, they may also in fact be evidence of the release of Au(111) intrinsic tensile stress prior to adsorption of the alkanethiol monolayer.

This idea is in some part strengthened by reports of sulphur and thiol adsorption relieving the surface reconstruction of Au. Clean Au(111) often shows a reconstruction to a $(23 \times \sqrt{3})$ lattice, corresponding to a 4.3% contraction of the surface, which is believed to be a response to the tensile stress of surface formation [110]. Even a relatively low coverage of adsorbed sulphur, of 0.1 ML (a tenth of a full monolayer), and of alkanethiols at 0.33 ML, has been shown, by ultra-high vacuum scanning tunneling microscopy (UHV-STM) studies, to lift this $(23 \times \sqrt{3})$ reconstruction from the Au surface [159], suggesting that the process of adsorption is in itself enough to relieve the tensile stress that led to the surface contraction.

The massive leap in stress from our value of -0.15 Nm^{-1} to that reported for dodecanethiol, by Godin et al, of -15.9 Nm^{-1} is purported to be due to the size of the Au grains on the cantilever's surface. They postulate that on smaller grains of 90 nm diameter, where they record stresses of -0.51 Nm^{-1}, the available areas of Au where a monolayer could develop are not large enough to lead to the formation of fully ordered monolayers. The c(4×2) superlattice is observed on the larger grained surface, using ex-situ STM imaging of molecular resolution. On the smaller grains, there is no such evidence.

5.8 Conclusions

This chapter has explored the potential sources of surface stress for a cantilever system with a simple decanethiol monolayer as its analyte. I developed an analytic model to return an approximate stress range that covers many of the reported experimental results for such a system available in the literature.

Each individual system of cantilever and adsorbate is different, and while stresses may have their origins in the same combination of adsorbate-adsorbate and adsorbate-substrate interactions, the degree to which each contributes to the final stress profile is highly variable. This chapter has raised the effects of the state of the underlying substrate, including the cleanliness of the surface and grain size, but other chemically, structurally and environmentally dependent factors can exert an influence.

Investigations into the effects of pH look at deprotonation of the analyte layer, for example carboxylic acid terminated SAMs [54], suggest that the majority of the surface stress measured is due to the repulsive coulombic interactions between, now charged, tail groups. Differences between the stress response to double-stranded and single-stranded DNA [101] suggest entropic effects, as different configurations lead to different steric forces. Bulkier analytes than the simple carbon chains mentioned here may exert steric forces on each other that repel, rather than attract, nearest neighbours; an effect possibly compounded by the 'water shell' that results from hydration forces [51, 160].

As in all biological systems, the net effect is only to be found by deconvoluting many components of the forces involved, that often work in opposition to one another. This chapter of the thesis highlights the importance of the gold substrate's influence on measured stress. It means an extra level of complexity is involved in ascertaining absolute values of stress for direct adsorbates. It also underlines the need to make simultaneous measurements and closely monitor the entire device setup. In many cases, however, the effect of the SAM is included in the baseline from which stress is measured, so the initial state of the substrate becomes less important.

In chapter (7) of this thesis, I will explore a system that takes a full monolayer as its measurement baseline; that of the antibiotic Vancomycin binding to monolayers of bacterial cell-wall peptide analogues. In this case, the focus of interest is on how the Vancomycin interactions drive experimentally measured changes in surface stress.

Chapter 6

Connectivity and stress

The previous chapter looked at the potential chemical origins of surface stress in the formation of an adsorbate layer on the surface of the cantilever. As outlined in chapter (4), however, there are cases where the stress is the result of a further layer of analytes binding to the underlying monolayer. In these cases coverage of the stress inducing events is not necessarily complete across the cantilever's surface and the positioning and proximity of the individual events becomes important; the stress also depends on a geometric factor.

In order to explore how the connectivity of Vancomycin binding sites on monolayers of D-Ala mucopeptides affects deflection of a cantilever, the lattice model must be extended to account for coverage of the analytes; allowing each site to be randomly 'occupied' with a probability p.

The rest of this chapter shows preliminary calculations of site percolation thresholds for the extended lattice model. While forming stress producing networks of individual events on a cantilever's surface is not truly subject to the strict laws that govern transport percolation, as outlined in the next section, we believe that it does rely to a great extent on the connectivity of those events. The percolation results were used to initially test the extended lattice model and are presented here to highlight some of the important points to remember when using the lattice model for stress calculations.

6.1 Percolation

Percolation is the formation of long-range connectivity in random systems. A classic example is to consider a porous material with some liquid poured on top of it. Percolation theory aims to understand the factors that will influence whether or not the liquid will be able to make its way through the material.

This example can be modelled as a 3-D network of vertices (n by n by n) the connections between which may be open or closed; situations with probabilities of p and 1−p respectively. What is the probability that, for a given p, there exists an open path right through the material?

For an infinite network of vertices the probability that an infinite cluster (a connected path of open vertices right through the network) exists obeys Kolmogorov's zero-one law in that it can have a value of only one or zero. In this case there must be a critical probability of openness, p_c, at which the probability of an infinite cluster forming flips from zero to one. In practice, even in small networks, this criticality is observable as the probability of an open path increases rapidly from very near to zero to very near to one, and is known as the percolation threshold.

6.2 Percolation thresholds

To test out the lattice model setup I attempt to reproduce the site percolation thresholds of the 2-D square and honeycomb lattices, which are well documented in the literature [161] as 0.59 and 0.70 respectively. As my lattices are not infinite in size, I have taken the average of 100 runs at various coverages which should give me a slight spread around the percolation threshold rather than a discrete transition from 0 to 1. This spreading effect can be seen in figures (6.2.1,6.2.2) showing the average of 100 runs for percentages of occupied lattice points from 0 to 100 %. This spreading is not huge and lies around the literature values for percolation thresholds in both cases.

These calculations only return an integer value depending on whether the

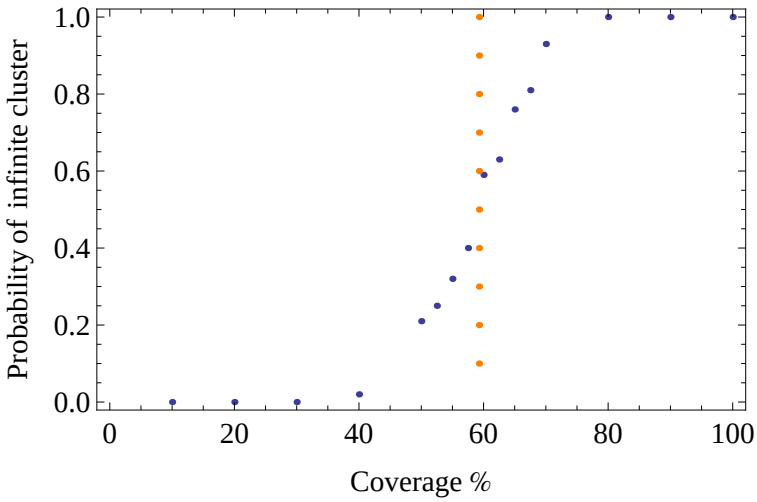

Figure 6.2.1: Degree of site percolation for 100 configurations at different percentages of occupied sites on a square 2-D lattice. The orange points show the actual percolation threshold of 0.59.

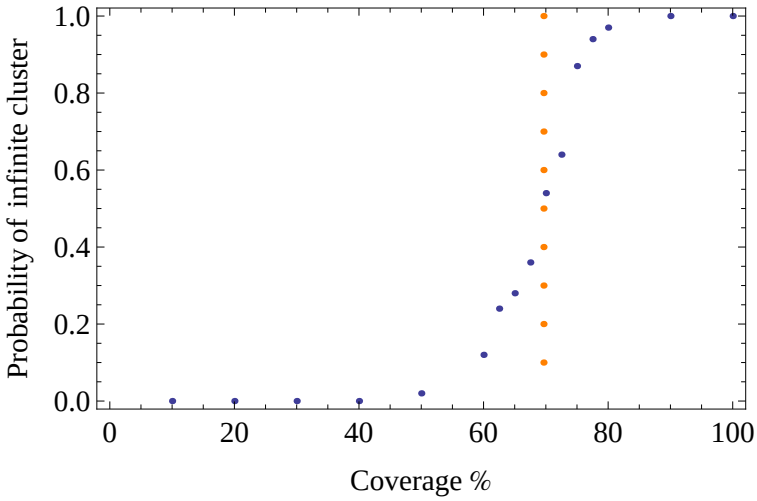

Figure 6.2.2: Degree of site percolation for 100 configurations at different percentages of occupied sites on a honeycomb 2-D lattice. The orange points show the actual percolation threshold of 0.70.

lattice has a cluster of occupied sites of infinite connectivity; one that spans the entire length of the lattice neighbour to neighbour. However, due to the random population of the occupied vertices it is possible with a finite lattice to have an extremely highly populated lattice with a lot of connected clusters that is non-percolating, and at the other extreme a very sparsely populated lattice with one percolating cluster, as demonstrated for a triangular lattice in figures (6.2.3) to (6.2.7).

As mentioned in chapter (5), the lattice I will use to calculate the Vancomycin stress response has only 2000 available sites. Variation in connectivity, and thus variation in stress, as showcased in figures (6.2.3) to (6.2.7), may have a significant effects on the results. On the much larger lattice that is afforded by the surface of the actual cantilever, these effects of variation will be somewhat smoothed out. For my model, it will be necessary to take the average of many calculations at the same coverage to find an appropriate estimation of the stress response. This requirement is further discussed in chapter (7).

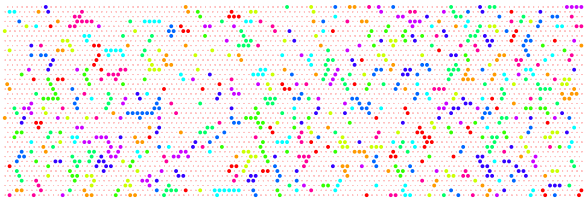

Figure 6.2.3: Triangular lattice at an occupation probability of 0.2 showing many tiny disparate clusters of occupied sites.

What also becomes extremely important when we are thinking about the connectivity of interacting events is the direction and distance over which those interactions produce a force. So, in the case of adsorbates that will be exerting both steric and charge driven forces on each other, the lattice model must be able to return the number of interactions (viewed as being like the bonds in straight percolation theory) in each direction (i.e. laterally and longitudinally) and the distances over which the adsorbates interact, which will depend on how

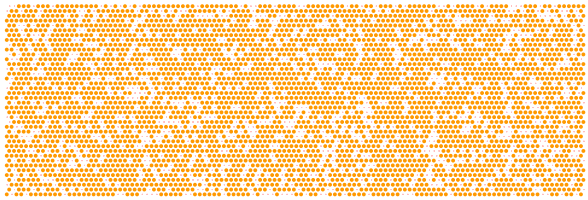

Figure 6.2.4: Triangular lattice at an occupation probability of 0.8 showing an 'infinite cluster' containing all occupied sites.

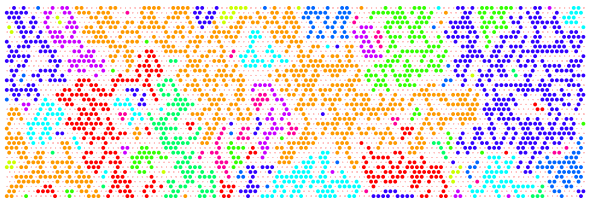

Figure 6.2.5: Triangular lattice at an occupation probability of 0.5 showing many clusters.

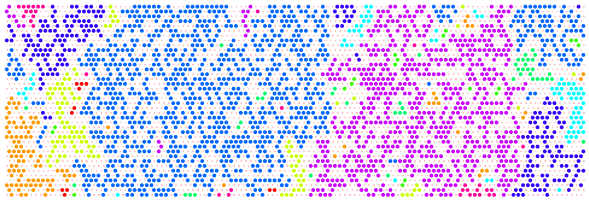

Figure 6.2.6: Triangular lattice at an occupation probability of 0.5 showing two dominant clusters but no percolation.

many neighbours each interaction type will encompass.

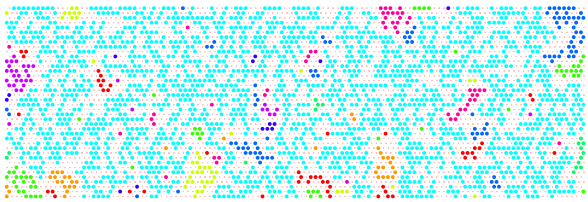

Figure 6.2.7: Triangular lattice at an occupation probability of 0.5 showing an 'infinite cluster'.

6.3 Application to Vancomycin

How is it then possible to take a complex real-life system, such as the interaction of Vancomycin on a cantilever's surface, to make a first step towards understanding how those individual chemical events are transduced to a large scale mechanical action that responds to the geometrical connectivity of those events?

The system under scrutiny must be deconvoluted into those factors that likely contribute to the stress, and simplified models of those factors developed and tested in predicting stress responses.

In the case of Vancomycin bound to a monolayer of bacterial cell wall peptide analogues many factors no doubt contribute to the final result: long-ranged coulombic repulsion due to the charges on a Van molecule at neutral pH; short-ranged steric repulsions between the individual Van molecules; interactions between Van and the monolayer which may be both local to the point at which the antibiotic is semi-inserted into the peptide layer and longer ranged and monolayer mediated, depending on the nature of the underlying peptides and their ability to communicate stresses.

Since the experimental investigations seem to suggest that the connected networks of events that induce a stress are likely steric and short-ranged in origin, the next chapter of this thesis will focus on the direct in-plane interaction of Vancomycin molecules bound to the terminal fragments of the peptide analogues. The approximate diameter of a bound Vancomycin molecule, as taken

from the crystallographic data [162], of $\sim$ 13/14 Å when compared to the reported intersulphur separation of D-Ala peptides of $\sim$ 7 Å [15] would support a repulsive interaction due to steric overlap, the extent of which will be determined by the ability of the bound Van molecules to structurally rearrange themselves at room temperature. The next chapter reports how molecular dynamics simulations were employed to investigate the validity of these assertions.

Chapter 7

Vancomycin

The first step must be to formulate a force representative of the in-plane interaction of Vancomycin molecules. This form can then be worked into the lattice model, as described in previous chapters, in order to gain a first approximation of how varying coverage of bound Vancomycin impacts upon the surface stress generation and the subsequent deflection of a cantilever.

7.1 The Vancomycin mean force of interaction

The true expression describing the force of interaction of Vancomycin molecules would be a complicated formulation of all the individual coulombic and steric contributions from all the atoms involved. Instead, it is possible to use molecular dynamics to describe a force curve between two Vancomycin molecules, by equilibrating the system at each separation and then allowing it to explore the configurational space available at a realistic temperature, and thus evaluating their mean force of interaction at decreasing separations, see chapter (3).

The focus of my interest is on how Vancomycin behaves and interacts with other molecules of its kind when it is bound to a bacterial cell wall peptide analogue. It is of interest to me how Van is structured when bound to said peptide. The file from which I take the structure of what I will refer to as the

Vancomycin-fragment complex, or simply 'the complex', is from the Research Collaboratory for Structural Bioinformatics Protein Data Bank (RCSB PDB); from a file that shows the crystal structure of several Vancomycin molecules either bound to diacetyl-Lys-D-Ala-D-Ala, acetyl-Lys-D-Ala-D-Ala or diacetyl-Lys-D-Ala-D-Lactate [162]. The first two fragments are Vancomycin sensitive and the third Vancomycin resistant. I take my initial input geometry from the second complex: Vancomycin bound to acetyl-Lys-D-Ala-D-Ala, as seen in figure (7.1.1). The structures here were determined using X-ray crystallography, which is generally unable to resolve the hydrogen atoms in protein crystals, so these were added using DS ViewerPro [163] prior to simulation.

Molecular dynamics programs rely on accurate parameters for those charges and force constants that describe the specific bonded and non-bonded interactions of atom types.

The structure is taken, as mentioned previously, from the Protein Data Bank [164]. Partial charges were taken from specifications in the literature describing a close structural relative of Vancomycin [165]. In the case of Vancomycin, the majority of the parameters describing the bond lengths, angles, etc. can be found within the force field specification lists provided with molecular dynamics programs - parameters previously optimised for similar configurations of atoms. For consistency, all the parameters I used to develop a FIELD file for the Van-fragment complexes were taken from the CHARMM topology files, which can be found on the Mackerell website [94, 95]. The FIELD file itself was compiled from the necessary parameter and structure input files using DL FIELD [166].

There are some sections of the molecule that are not explicitly parametrised in the existing literature; ether linkages between benzene rings and between the main backbone and the glucose group, an amide group attached to a benzene ring via an aliphatic carbon atom and the methyl group attached to the N-Leucine residue. There are similar systems described in the literature from which first approximations can be taken, a full list of which is in appendix (D). Since I am not using the simulations to explore the dynamics of the complexes and the sections are also limited to some extent by those explicitly parame-

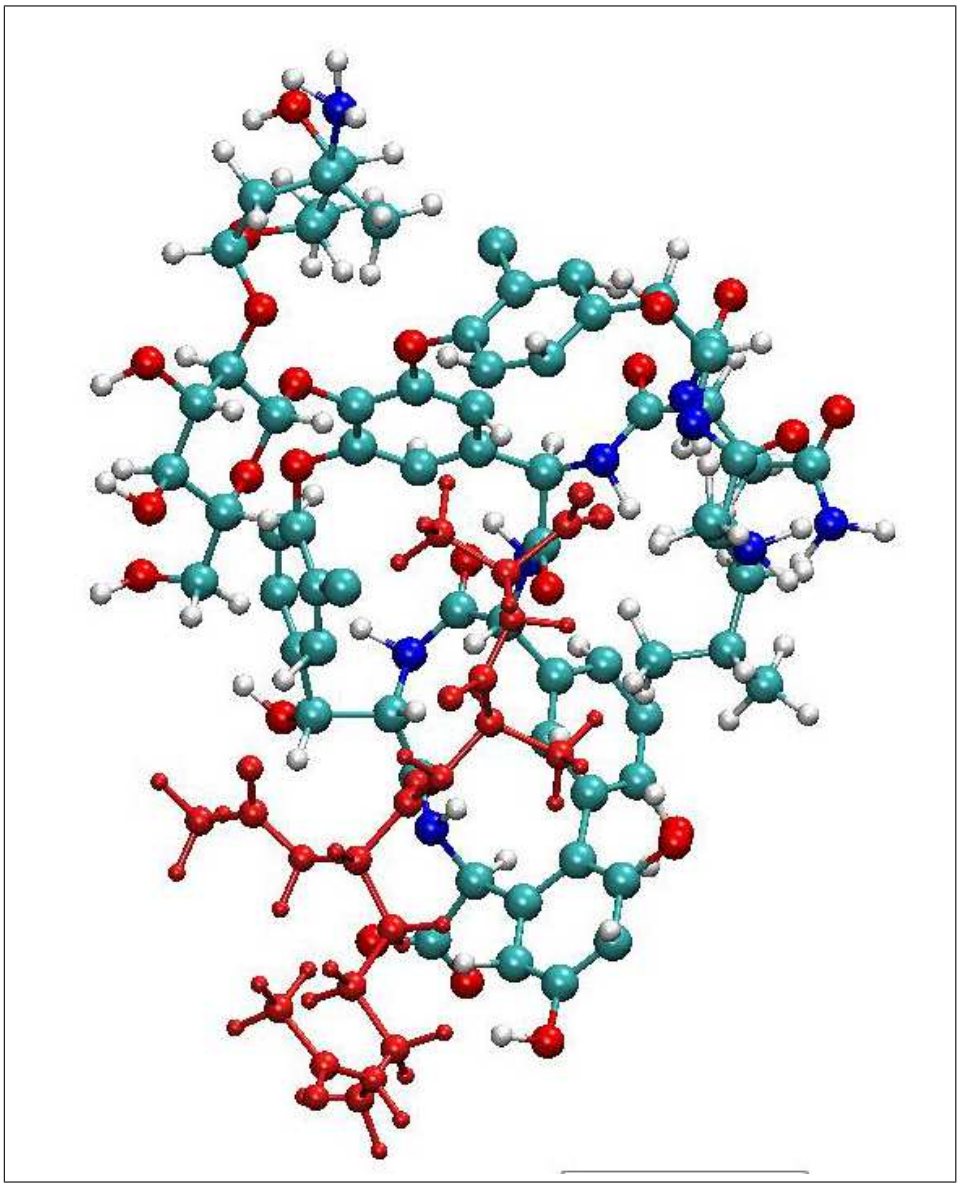

Figure 7.1.1: Structure of Vancomycin from RCSB PDB, shown with acetyl-Lys-D-Ala-D-Ala (in red). Coordinates from [162].

terised sections around them, I will accept this approximation in the simulations. Future work on this project, given more time, would involve validation and, if necessary, further optimisation of these parameters, following the process described in detail in [95].

In order to gather information on the energetic interaction of two adjacent complexes, I explore their behaviour as a pair up to a separation of ~ 50 Å, at which distance their effect on each other is relatively minimal.

The separation of the complexes is taken as being between the sites that dictate the constraint of the force calculations. I have taken these sites as the carbon atoms at the base of the peptide fragment in each complex; the point where the fragment would connect to the PEG chain that attaches the whole to the cantilever surface. This is chosen to represent the tethering effect afforded by said chains, which most likely form the relatively stable, upright layer of the full monolayer system.

I was first interested in the repulsive forces due to close proximity of the complexes. As such I placed two complexes in simulation at a distance apart where they experienced no overlap, at 13.4 Å, for the first run. The complexes were simply shifted so that the constrained carbon atom for the second complex remained in plane with the first. Subsequent simulations at shorter distances of separation were then run from the final configuration of this initial run. The remainder of the force curve was built up by also taking this initial run final data set and moving the complexes apart with each new simulation.

By using this method of approaching the run of simulations we possibly find the complex pair in a local energetic minimum corresponding to their configuration in the first run. A way to explore the energetic landscape that might expose the global minimum of a pair could be to take the complexes to a separation where their interaction is negligible and incrementally bring them together from there. However, the global minimum for an isolated pair of complexes is not necessarily the best representation of a pair of Van molecules on a monolayer. Other sources of energetic impetus will be provided by the surrounding environment and will affect the configurations that the Van molecules can assume,

as further discussed in the next section.

The simulations will give me a set of values for the forces between the complexes at each separation. The force curve, plotted against separation, is unlikely to be a smooth one, due to the size and flexibility of the complexes. With each step it is not only the distances between the atoms of the complexes that changes, but also their configuration. As the complexes move in relation to one another, local minima afforded by conformational changes become more or less available. For a molecule as complex as Vancomycin, with flexible outlying groups, there are surely many different avenues of approach between a pair of them. With that in mind, in order to produce a reasonably coherent force curve, when the complexes are close enough to physically limit each other's movement (taken as up to 22 Å) each simulation is started from the final configuration of the previous run. I've also kept the separation steps small within this proximity range, to try to ensure that the pair of complexes is following one particular path of approach. As the separation between the complexes increases, so does the size of the step, from 0.1 Å, to 0.2, to 0.4, to 1.0 and finally to 2.0 Å.

Each simulation was run in DL POLY 2.19 [97] using the pmf ensemble (NVE) to calculate the mean force of interaction between the two. At each separation the pair of Vancomycin molecules plus their D-Ala fragments were simulated in a vacuum at a temperature of 300K for 2 ns. The first 500000 fs timesteps used temperature scaling to equilibrate the molecules in their new positions, and statistical information was gathered over the remaining timesteps.

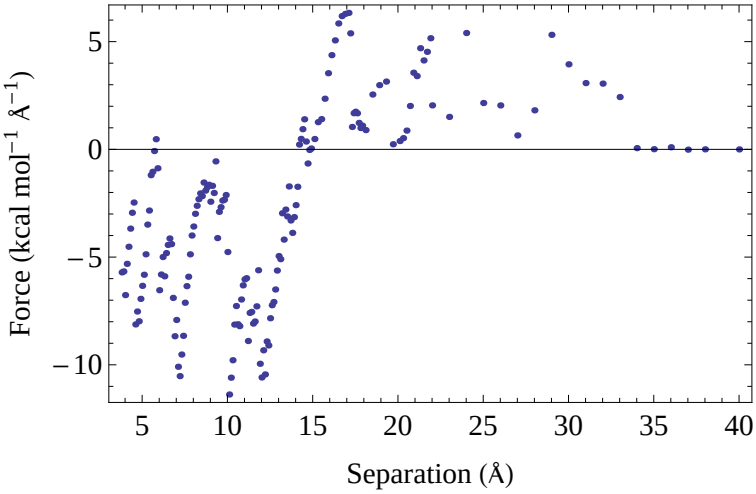

Figure 7.1.2: Plot showing the mean force of interaction between two complexes of the antibiotic Vancomycin and acetyl-Lys-D-Ala-D-Ala at varying separations, as calculated using the pmf ensemble in DL POLY 2.19.

7.2 The force curve

The statistical data I am interested in from the constrained simulations in the pmf ensemble is the mean force of interaction of the two approaching complexes, rather than the potential of mean force itself. This mean force can be calculated from the system constraint virial as described in chapter (3).

The plot in figure (7.1.2) does not show a continuously smooth force curve describing the interaction of two Vancomycin-peptide fragment complexes, as was expected due to the energetic landscape surely available to such large and flexible molecules at room temperature.

The smooth section of the curve, from $r \sim 12$ to 17 Å, well describes the interaction around their energetic minimum as a pair. Here the complexes in simulation are in close enough proximity to hinder one another's movement, but not so close as to make large configurational changes energetically favourable. So, as mentioned in the previous section, this minimum is likely to be a local one, a point supported by the large changes in mean force of interaction at ~ 12

and ~ 17 Å.

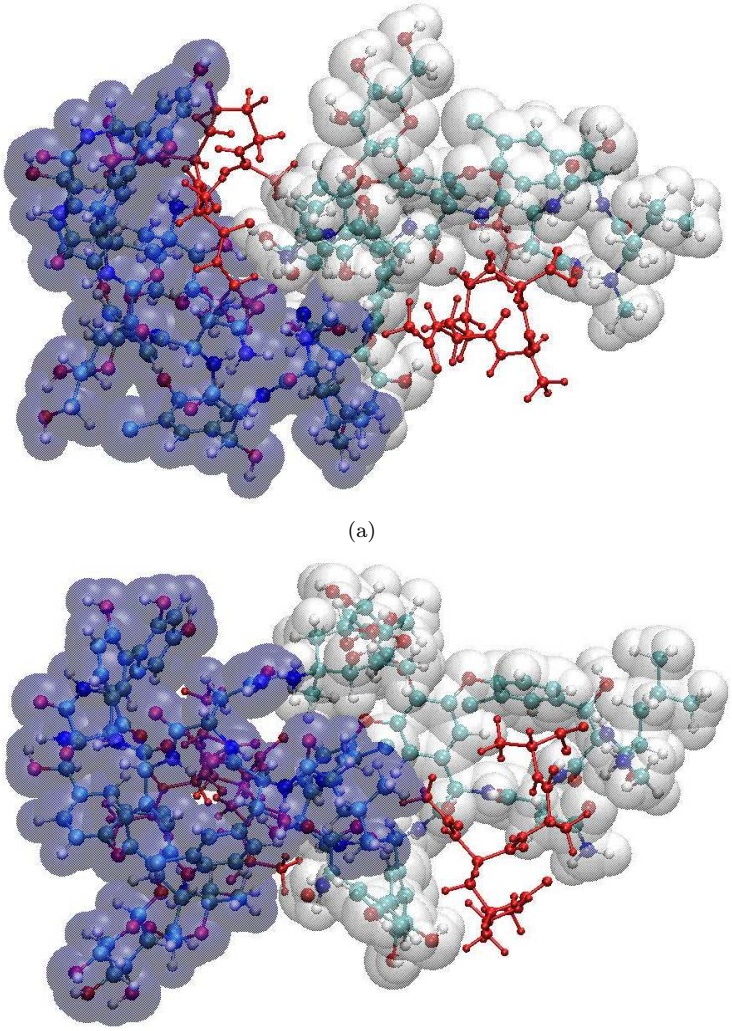

(a)

(b)

Figure 7.2.1: Conformation of the Van-complex pair at a separation of 14.2 Å, which corresponds to their equilibrium separation, as seen from above (a) and from the side (b).

Within this separation range the two complexes are in a back-to-front configuration, as seen in figure (7.2.1); one possible orientation of a pair of Van

molecules bound to the monolayer. Beyond this range, due either to an increase in configurational energy of the system making new energetic minima available, or to more space between the complexes allowing thermal excitations to reorganise the molecules, the complexes explore other configurations. An example of one of the configurational shifts that leads to a large jump in the force curve can be seen in figure (7.2(a)). This corresponds to the separation between the two Van-complexes being increased from 17.1 Å, in blue and cyan, to 17.3 Å, in red and green; to those values of intermolecular force as highlighted in figure (7.2(b)). The biggest change in conformation is the movement of the leucine group on the right hand Vancomycin closer towards the peptide fragment of the same complex. The vancosamine group on the left hand Vancomycin has also shifted towards the centre of mass of that complex.

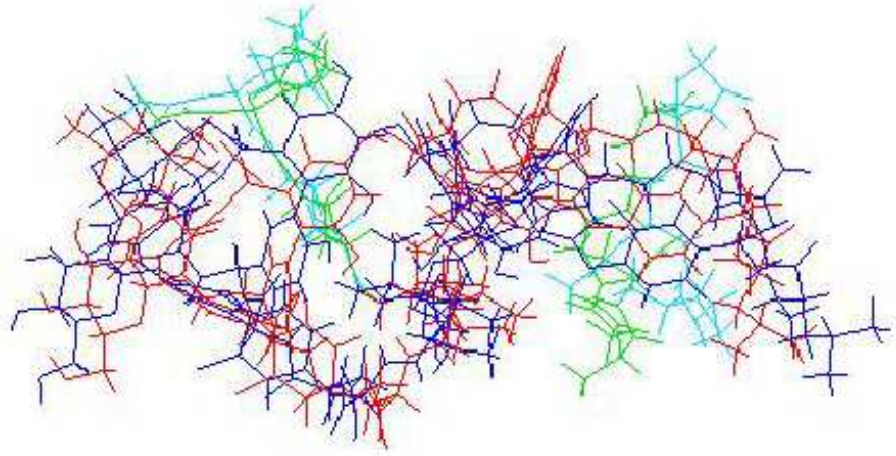

(a)

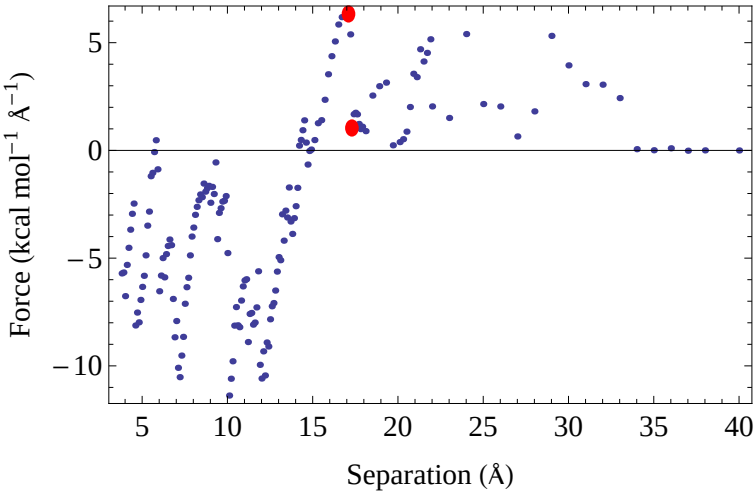

(b)

Figure 7.2.2: Conformational changes of the Van-complex pair in moving between separations of 17.1 Å and 17.3 Å and the corresponding points on the intermolecular force curve (highlighted as red discs).

As the complexes are only constrained by the distance between a carbon atom in each they are able, particularly under the energetic drive at the closer separations, to assume configurations that would be physically improbable as part of a monolayer system. In reality bounds would be imposed on a molecule

by the tightly packed peptide chains beneath and by the other D-Ala tailgroups and bound Vancomycin surrounding this adjacent pair.

In actuality, the interaction between two Vancomycin likely lies somewhere between the sprawling force curve described in the first half of figure (7.1.2) and that extrapolated from the smooth section of interaction between the back-to-front complexes around the energetic minimum.

As such, and because the force curve is well-defined around this r_{min}, I will take my fit from this part of the data set and in assuming that any such fit corresponds to the quite constrained back-to-front configuration, will take results from this fit as something of a first approximation.

Future work will involve simulating Vancomycin molecules within an environment more closely resembling the complete monolayer and will explore the behaviour at close separations in a more realistically constrained environment.

7.3 Fitting the force curve

The simplest way to reproduce the main repulsive and attractive features of an interaction energy curve is using an n-m potential, as in equation (7.3.1) [97].

$$U(r_{ij}) = \frac{\epsilon}{(n-m)} \left(m \left(\frac{r_{min}}{r_{ij}} \right)^n - n \left(\frac{r_{min}}{r_{ij}} \right)^m \right) \tag{7.3.1}$$

Where r_{min} is the equilibrium separation, ϵ the well-depth of the subsequent potential and r_{ij} the distance between the two complexes.

Differentiating with respect to r_{ij} gives the force,

$$F(r_{ij}) = \left(\frac{\epsilon n m}{(n-m)} \right) \left(\frac{r_{min}^m}{r_{ij}^{m+1}} - \frac{r_{min}^n}{r_{ij}^{n+1}} \right), \tag{7.3.2}$$

which was used for initial fits to the Vancomycin force data.

The equilibrium separation corresponds to that point where the forces between the complexes are zero; where the force curve in figure (7.1.2) crosses the x-axis. The straight line in the force curve around this point, corresponding to the harmonic section of a potential representative of the interaction of two

complexes is well-described in figure (7.1.2). If an n-m curve is appropriate as a first description of the interaction profile, this section of the curve can yield n and m as well as the equilibrium separation.

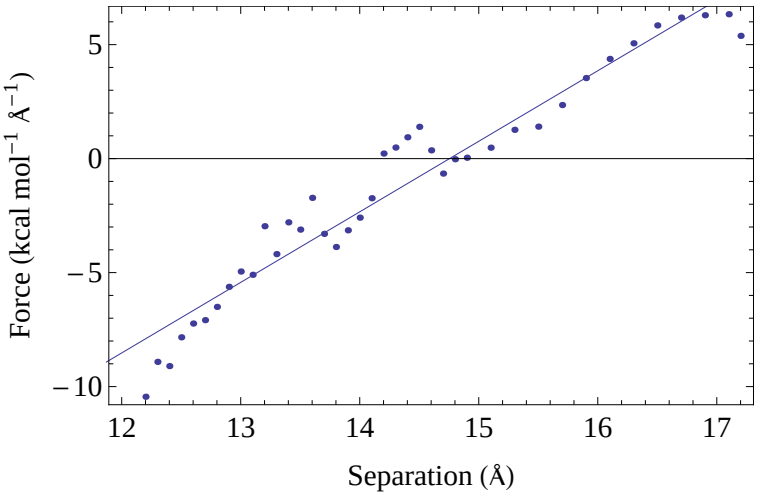

Figure 7.3.1: Figure showing a straight line fit to the force curve around the point at which it crosses the x-axis. This fit gives an equilibrium separation for the Vancomycin-peptide fragment complexes of 14.75 Å.

A straight line fit to those data points that lie around the point at which the x-axis is crossed, as seen in figure (7.3.1), gives an equilibrium separation of 14.75 Å.

This value for r_{min} was then kept constant and least-squares fits to this continuous part of the force curve for various integer values of n and m. All fits were performed using Mathematica 8.0 [25].

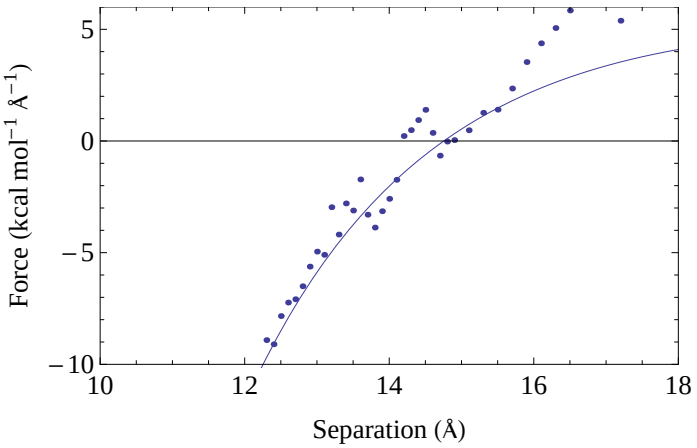

(a)

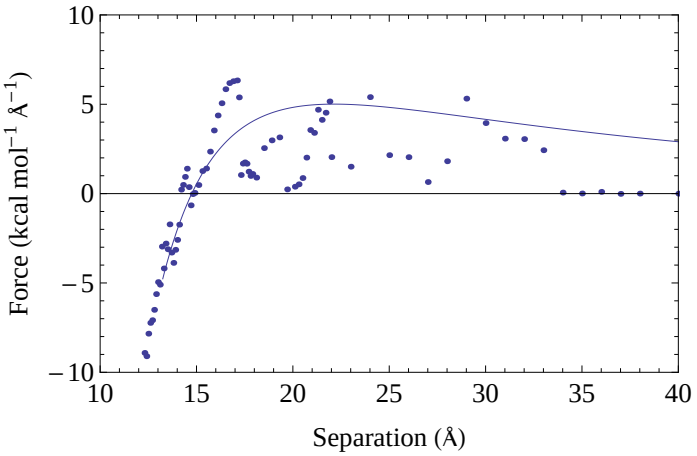

(b)

Figure 7.3.2: Figures showing the 3-2 curve fit to the PMF data.

The flexible, extended nature of the Vancomycin molecules makes for an approach between two complexes that is much softer than the 'hard-sphere repulsion' of smaller molecules. The n-m curve that best describes the curve around r_{min} is a 2-1 curve, see figure (7.3.2), as dictated by the magnitude of the sum of the residuals.

Which gives an analytic expression for the interaction force between the two complexes of,

$$F(r_{ij}) = 2\epsilon \left(\left(\frac{r_{min}}{r_{ij}^2} \right) - \left(\frac{r_{min}^2}{r_{ij}^3} \right) \right). \tag{7.3.3}$$

7.4 The stress response

Now that an analytic form of a force curve that approximately fits the calculated data points has been found, this can be incorporated into my Mathematica lattice model in order to find a first approximation of the stress associated with the interaction of Vancomycin molecules bound to a D-Ala monolayer.

The Mathematica model is fundamentally the same as in chapters (5) and (6), but in this case the lattice must be parameterised to, as accurately as possible, represent the monolayer to which Vancomycin binds.

7.5 Approximations and assumptions

Work undertaken by M. Vogtli using surface plasmon resonance to characterise the degree of Vancomycin binding to available D-Ala sites gives a value of $\sim 40\%$ for a full, standing monolayer, where 100% would correspond to a one-to-one ratio of D-Ala to Vancomycin. So when calculating the stress for Vancomycin binding to a full monolayer of D-Ala, rather than using p = 1 in the lattice model, I use p = 0.4, and scale the other coverages accordingly.

As mentioned in chapter (6) the diameter of a bound Van molecule can be approximated to $\sim 13/14$ Å. The corresponding radius would suggest that Vancomycin molecules are able to bind to immediately adjacent D-Ala sites (see next section for peptide separation details); the slight discrepancy that may exist between the D-Ala separation and the repulsive dimensions of the complexes supports a steric mechanism for stress induction.

In the model the lattice represents a complete, hexagonally close-packed monolayer of D-Ala peptides. While there much support in the literature for alkanethiols forming hexagonal lattices [145, 167, 168], the much bulkier and asymmetric tail group on the D-Ala peptides raises questions around whether

they would find their lowest energy configuration in such an arrangement. However, until further research, both theoretical and experimental, is done on the precise nature of monolayers of these bacterial cell-wall peptide analogues, I shall assume an hexagonal lattice.

A theoretical lattice construct that corresponds to a complete, standing monolayer is not wholly accurate either. In reality, as mentioned in previous chapter (5), the surface will be comprised in part of etch pits, vacancy islands and the discontinuity of Au grain boundaries [169, 170]. The effects of these features on the stress response [106, 107] warrants closer investigation, but is beyond the current scope of this thesis. For the time being I will assume that their presence will predominantly be a matter of altering the magnitude of the surface stress, rather than significantly changing its nature.

I have also assumed within this iteration of the lattice model that the active D-Ala sites can occupy any vertex on the lattice completely randomly. In actuality the mixing of the PEG and D-Ala on the cantilever's surface may be subject to preferential or cooperative adsorption behaviour that results in clumps of active and inactive monolayer. Increased knowledge about the nature of the underlying monolayer is really important in the development of a truly representative surface stress model.

7.6 Peptide separations

XPS measurements made by Ndieyira et al [15] of a D-Ala monolayer show an inter-sulphur separation of $\sim$ 7 Å for a peptide footprint of 44 Å^2, when the peptides are chemisorbed in a close packed hexagonal configuration, which corresponds to around 2×10^{11} peptides per cantilever at a full coverage of p = 1. Subsequent XPS measurements and calculations performed by M. Vogtli show some variation in the density of peptides packed on gold, placing the separation of adjacent D-Ala within a standing monolayer as being between 6 and 8Å.

The intermolecular distance of two adjacent D-Ala molecules within a range suggested by these experimental investigations are in good agreement with val-

ues I have obtained from preliminary simulations.

As a starting point in investigating the nature of the monolayer I have simply run simulations on two adjacent D-Ala molecules in vacuum at increasing separations from 4 Å to 17 Å in order to build up an interaction curve between them.

All calculations were performed using the molecular dynamics package DL POLY 2.19 [97]. The equilibrium atomic configuration of D-Ala as it would be in a monolayer was taken from energy minimisation calculations performed by M. Sushko. The force field for the D-Ala molecules again used CHARMM [140] parameters and was constructed using the program DL FIELD [166]. In order to get an idea of the interaction curve for two molecules in a monolayer, the head group S atom, the uppermost C atom, and the C atom of the CH_3 group at the end of the lysine arm were held frozen in order to hold the molecules roughly in the shape they would adopt in the monolayer. See figure (4.0.1) for the structure of D-Ala. Each setup is equilibrated for 1000 steps and then further run for 40,000 steps at a temperature of 300K, resulting in the interaction potential that can be seen in figure (7.6.1). Each value for interaction energy here is taken as the energy of two D-Ala molecules together minus twice the energy of a single isolated D-Ala, i.e. $E_{int} = E(\text{2D-Ala}) - 2(E(\text{D-Ala}))$. The curve suggests an energy minimum between the two peptides in a separation range of $\sim 6.5 - 7.5$ Å.

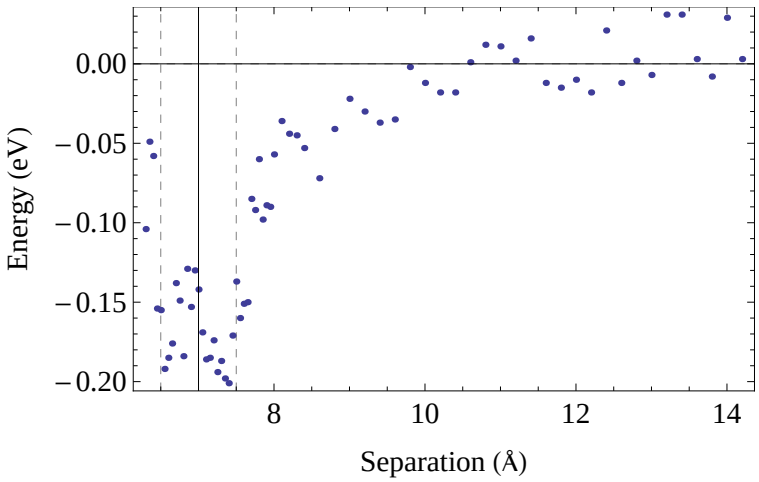

Figure 7.6.1: Interaction curve for two D-Ala molecules in a vacuum, as calculated by DL POLY 2.19. [97].

7.7 Commensurate separations

If the D-Ala peptides form a hexagonally close packed monolayer, with a separation of $a \sim 7$ Å it makes sense to find out which separations lying within a range around that value can form hexagonal lattices that are commensurate with binding sites in the underlying Au substrate.

As mentioned in chapter (5), the preferential adsorption position for S on a (111) Au surface is a subject under ongoing investigation. So for the purposes of these calculations I will be assuming that the S atom at the head of the D-Ala peptides is able to adsorb to any one of the suggested hollow [133, 134], bridge [113, 135] or atop [136, 137] sites on the Au (111) surface, as they seem to differ little in energy [105].

Allowing for some uncertainty in the calculations to find the molecular area of a standing D-Ala peptide, I calculated a list of all those separations on the lattice that fall between 6 and 8 Å, see appendix (C). By plotting the occupied positions that yield the allowed separations, it is possible to see immediately those that can form a hexagonal arrangement of adsorbates.

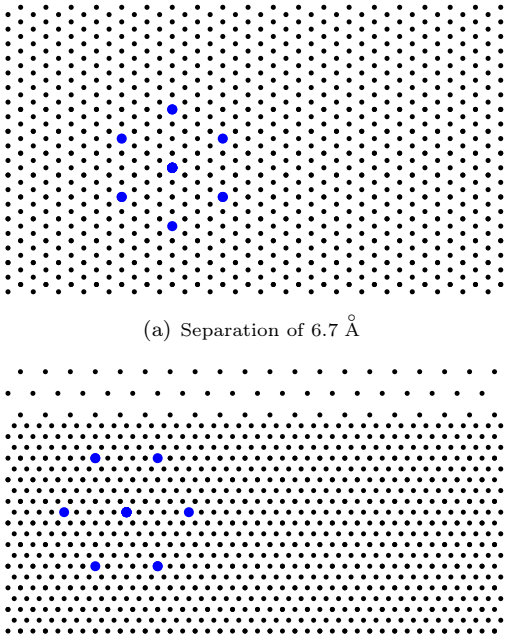

(a) Separation of 6.7 Å

(b) Separation of 7.3 Å

Figure 7.7.1: Hexagonal patterns of adsorbed S on an Au (111) surface, commensurate with binding to the available substrate sites.

The interpeptide separations of 6.7 Å and 7.3 Å, see figure 7.7.1, falling as they do within the predicted range from experiment and simulation, are the distances between vertices that I will use in the following calculations with the lattice model.

7.8 Calculation details

The results are obtained in the same way as for the decanethiol monolayer, although in this case the monolayer substrate interactions play no part in transducing the measured differential stress, as the system is already in equilibrium with a full D-Ala monolayer. Any bending resulting from that equilibration is taken as the baseline from which Vancomycin induced bending will be measured.

Stress values were calculated for lattice occupation values of 0.01, 0.02, 0.03,

0.04, 0.05, 0.06, 0.07, 0.08, 0.09, 0.1, 0.2, 0.3 and 0.4.

One point to be remembered when looking at these theoretical results is that they are averages of many calculations. This is necessary as, as previously mentioned, when 'events' are able to occur randomly on a lattice, and the coverage is less than p= 1, then different configurations will lead to quite different interaction connectivity for the same coverage. This is an issue because the program provides a rather small, let alone finite sized, lattice environment, and so these variations in configuration are not averaged out within the system itself, as is the case in purely theoretical, infinite percolation [161].

In order to get statistically valid results from the lattice model I have taken the average value for stress over many runs at each coverage. 600 runs for each data point was enough to bring the standard error for each stress value within $5 \pm 2\%$.

7.9 Fitting the stress results

The average value, from 600 different random configurations, of total stress at a Vancomycin coverage of p= 0.4, taken as corresponding to a full underlying D-Ala monolayer with a peptide separation of 6.7 Å, is $\sigma = -110.06$ mNm^{-1}. This is in reasonable agreement, within an order of magnitude, with the experimentally determined value of $\sigma = -34.6 \pm 0.9$ mNm^{-1} as averaged over more than 100 measurements for a full D-Ala monolayer and a Vancomycin solution concentration of 250 μM.

When run with a peptide separation of 7.3 Å, however, the model shows no bending of the cantilever, even at those configurations at full coverage that yield the highest stress values for the 6.7 Å setup.

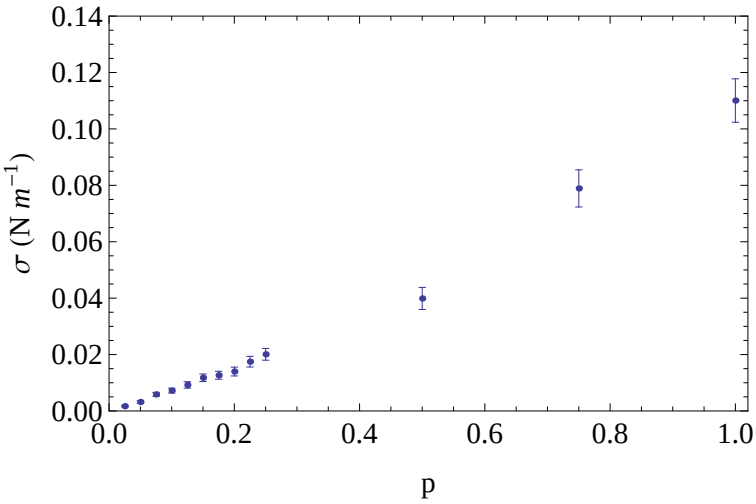

Figure 7.9.1: Calculated stress, and standard error, induced by varying coverage of D-Ala peptides in a mixed monolayer, upon exposure to Vancomycin.

Those averaged stress results for the peptide spacing of 6.7 Å and decreasing coverage, p, can be seen in figure (7.9.1).

I fitted equation (4.1.1) to the theoretical values obtained from the 6.7 Å peptide spaced monolayer, using parameters defined in [15]. Fitting with a maximum stress response at saturation of $a = -110.06$ mNm^{-1} and a dissociation constant of $K_d = 1.0 \pm 0.3$ μM gives a percolation threshold of $p_c = 0.003$, compared to that obtained by Ndieyira et al, of 0.075 ± 0.09 , and $\alpha = 1.15$, compared to $\alpha = 1.3 \pm 0.3$, as can be seen in figure (7.9.2). The theoretical values for p_c and α fall within the experimental uncertainty of Ndieyira et al's findings, and what small differences there are between my results and those in [15] I believe to be a consequence of the current simplicity of the model.

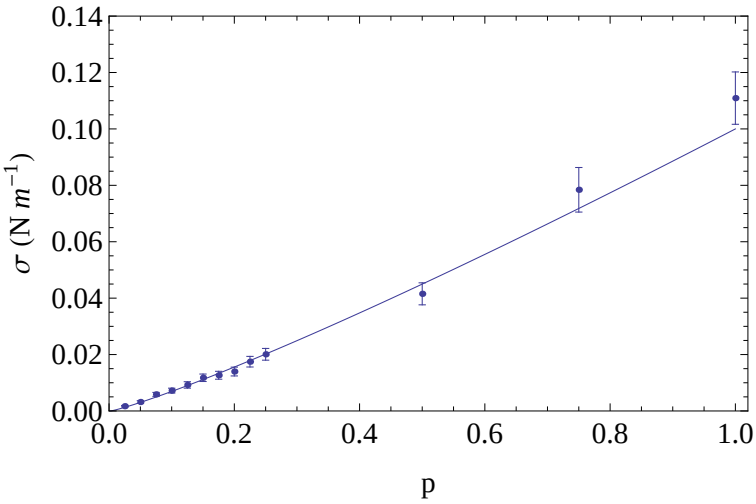

Figure 7.9.2: Showing the fit of equation (4.1.1) to the calculated stress values for Vancomycin.

7.10 Conclusions

Using the inter-complex force curve from MD simulation and the lattice model for cantilever site coverage, I obtain a saturation stress for a full D-Ala-Vancomycin covered cantilever, $\sigma = -110.06$ Nm^{-1}, a percolation threshold, $\mathrm{p}_c = 0.003$, and an exponent for the power law describing the stress signal increase with coverage beyond p_c, $\alpha = 1.15$.

The surface stress result, σ, is within an order of magnitude of that determined experimentally for the system in question and p_c and α both lie within the range postulated from experimental observation in conjunction with model represented by

$$\Delta\sigma_{eq} = \frac{a\,[\mathrm{Van}]}{K_d + [\mathrm{Van}]} \left(\frac{\mathrm{p} - \mathrm{p}_c}{1 - \mathrm{p}_c}\right)^{\alpha}$$

The stresses documented above are the result of an interaction potential that can be decomposed into two main contributions: steric and electrostatic. These contributions differ in the way they behave across the lattice. The electrostatic

interaction is long-ranged, whereas steric interactions take place over the range of nearest neighbours.

As the force curve was obtained from simulation in vacuum there is the possibility that the electrostatic contribution is overemphasised. In buffer, the strength and reach of the electrostatic interaction would be tempered by a degree of screening due to ions in the solution surrounding the cantilever. A reduction in the electrostatic part of the force of interaction at the surface may reveal a larger p_c.

Any more detailed representation of the interaction of bound Vancomycin however, must also acknowledge that the 'nearest-neighbour' steric Van to Van repulsion will be coupled with a longer range, monolayer mediated effect due to insertion of the antibiotic into what is after all not a static, rigid lattice, but an extremely flexible layer of biological molecules. The magnitude of this effect will depend on the orientation of the Van on the monolayer and the configuration of the peptide layer.

The change in response from the 6.7 Å lattice spacing to 7.3 Å highlights the predominance of steric repulsive forces in eliciting a beam response. It also underlines how knowledge of the structure and spacing of the underlying D-Ala monolayer is crucial to calculating a realistic stress response and yet this is something that remains fairly uncertain.

All the above being said, as a first approximation, this simplified model returns a saturation surface stress within an order of magnitude of that measured experimentally, and a stress to active peptide coverage relationship that agrees with the model postulated in [15], accounting for experimental error. This is an encouraging start to theoretically quantifying and predicting stress responses of cantilever-adsorbate systems, and another step towards true understanding of what governs the process at a molecular level.

The next steps in refining this model and further avenues of investigation suggested by this work are outlined in chapter (10).

The strength of a final model will come from accurately representing each part of the whole cantilever sensor setup, biosensitive active layer, beam, envi-

ronment and measurement system included. With this in mind the next two chapters look, respectively, into the elastic response of the beam to a differential surface stress in greater detail, and into some of the challenges and opportunities presenting by the operating medium for a cantilever in its dynamic mode.

Chapter 8

The beam response

While the main thrust of this thesis is towards better understanding the molecular basis for stress propagation on the surface of a cantilever, modelling the elastic response of the beam accurately is just as important in developing a truly representative model; both for quantitative analysis of any response, and to maximise said response for measurement.

In this chapter, I make some initial investigation into how the materials and active surface patterning can be exploited to increase a cantilever's sensitivity to surface stress.

I look at the geometric and material 'figures of merit' for the sensitivity of a beam to simple, pure bending, and to torsional bending. I then explore how changing the pattern of the Au active surface on a beam can affect the ultimate deflection, either positively or negatively in terms of the magnitude the response.

8.1 Maximising the bending response

The analytic formulation for a bending beam, in chapter (5), can be explored quite simply to uncover some geometric or material 'figures of merit' for improving the sensitivity of a cantilever to surface stress. In this section I derive

analytical expressions for the deflection, curvature and sensitivity to stress for a beam undergoing pure bending along its long axis and look at those geometric and material factors that can immediately improve a cantilever's performance.

We look again at the expression for the strain energy of a bent beam,

$$U_{st} = \frac{E'bLh^3}{24R^2}, \tag{8.1.1}$$

which we can write as β/R^2, and define β as

$$\beta = \frac{E'bh^3L}{24}. \tag{8.1.2}$$

We now consider a layer (surface) added to the top of the beam. The layer's unstretched length is $L = R\theta$ as before, but this time the stretched length will be $L_L = (R + \frac{h}{2})\theta$ giving an elongation of $\frac{h}{2}\theta$.
The elongation of layer L leads to an increase in area of $b\frac{h}{2}\theta$ so the increase in energy corresponding to the stretching of the surface is

$$U_{su} = \frac{bh\theta\sigma}{2}, \tag{8.1.3}$$

where σ is the surface stress. The expression, as before, can be written as α/R with $\alpha = \frac{bhL\sigma}{2}$.

So, for the beam, the total energy increase due to bending is

$$U_{tot} = U_{su} + U_{st} = \frac{\alpha}{R} + \frac{\beta}{R^2}. \tag{8.1.4}$$

We can determine the expressions for the radius and angle of curvature of the beam by minimising U_{tot} with respect to R,

$$\frac{dU_{tot}}{dR} = \frac{-\alpha}{R^2} - \frac{2\beta}{R^3} = 0, \tag{8.1.5}$$

$$\rightarrow \frac{2\beta}{R} = -\alpha. \tag{8.1.6}$$

Giving us the following expressions:

Substrate material	E (GPa)	L:t (μm)	$\frac{d\theta}{d\sigma}$ mN^{-1}
Silicon	165	500:0.9	0.0150
Silicon dioxide	75	250:0.5	0.080
Silicon nitride	200	250:0.5	0.030
Gallium arsenide	85.5	250:0.5	0.070
Tungsten nanorod	410	45:0.1	0.067
SU-8	4.02	200:2	0.075
Polyimide	7.5	375:2	0.075
Poly-methyl methacrylate	4	375:2	0.141
Polypropylene	1.45	375:2	0.388
Polystyrene	3	375:2	0.188
Nanoclay and Nylon composite	2.83	375:2	0.245
Single carbon nanotube 1	1000	2:0.0012	8.333
Single carbon nanotube 2	1000	100:0.0011	495.868

Table 8.1.1: Table of commercially available or literature referenced examples of materials for use as nanocantilevers, with their corresponding sensitivities to surface stress.

$$R = \frac{E'h^2}{6\sigma}, \tag{8.1.7}$$

$$\theta = \frac{6L\sigma}{E'h^2}. \tag{8.1.8}$$

These expressions can be manipulated to yield important information about the usability of a cantilever. For example, the sensitivity of a cantilever response to changes in surface stress is

$$\frac{d\theta}{d\sigma} = \frac{6L}{E'h^2}. \tag{8.1.9}$$

8.1.1 Maximising deflection for a simple beam

Values for the sensitivity of nanocantilevers developed using some of the currently commercially available materials are listed in table (8.1.1).

The values for Young's moduli (E) and aspect ratios are taken from the references [171, 172, 173, 174, 175, 176]. The length to thickness aspect ratios

that I have listed are either typical from the literature or those commercially available.

Sensitivity of a nanocantilever to changes in surface stress is primarily dependent upon the elastic modulus and thickness of the substrate material.

Due to their relatively low E and advances in affordable and repeatable manufacturing processes such as injection molding, polymers would seem to be ideal candidates for microsensors. Polymeric cantilevers can be produced with a thickness of $\approx$ 2 μm and with many polymers exhibiting Young's moduli less than 50 times that of those materials generally used for nanocantilevers (silicates/gallium-arsenide)[171, 173], yield a much higher sensitivity to surface stress. However polymers are, on the whole, much more sensitive to changes in their environment, for example nylon demonstrates a reduced elastic modulus on prolonged exposure to water and photopolymers can become brittle after exposure to E-M radiation. The biggest challenge to overcome with polymeric cantilevers is the effects of temperature. While the thermal expansion coefficient of silicon is on the order of 3.2 ppm per °C, a typical polymer ranges from around 50-100 ppm per °C [174], so fluctuations in a response due to temperature variation becomes significant.

Another integral requirement of microsensors is a high degree of specificity dependent on the cantilever surface. Polymeric cantilevers, advantageously, can be directly functionalised. For example SU-8 is an epoxy photoresist that crosslinks via photon-initiated epoxy group ring opening on the monomers. Unreacted epoxy groups on the surface of the SU-8 structure can then be utilised as binding sites [175].

General practice with silicon-type cantilevers is to coat the substrate in a thin layer of gold, as thiols (which act as linking molecules to bind the appropriate analyte) have a high affinity for gold surfaces. The addition of a gold layer leads to a stiffer cantilever and more pronounced temperature instabilities due to lattice mismatch between the layers. An opportunity to move away from this practice could lead to improved microsensor performance. However, processes such as the self-assembly of thiol monolayers directly onto a polymeric surfaces

are potentially less controlled than onto gold and the effects on sensor response would have to be fully investigated.

Two sensitivity values in the table above obviously stand out; those for the single carbon nanotubes (SWCNTs) are so much higher than for the other materials. This seems odd considering how stiff SWCNTs are, with a Young's modulus of around 1000 GPa, but arises from their extraordinary stable aspect ratios [172]. CNTs can be used as AFM tips, where the end of the CNT is functionalised directly using the carboxyl groups present at the open ends [176]. One of the major problems with using CNTs is the lack of control over their growth. The interpretation of results from microsensors is often largely based on assumptions of fixed conditions between sequential experiments, which might be difficult to achieve using CNTs. However, the potential of lesser used materials such as those mentioned here certainly warrants further investigation.

As mentioned briefly before, another potential way of maximising a cantilever's response lies in manipulating the bending response of a cantilever through patterning of the gold or the analyte-specific layer on the surface. There has been some investigation in the literature into how the positioning and length of the active strip along the long axis of the beam affects its simple bending response [177], and this is something I will be looking at in more detail in section (7.1(b)). First, though, I will look at how moving away from the simple beam bending setup and instead inducing a twist of the cantilever due to adsorption comes to bear on the measurable deflection and sensitivity to stress.

8.2 A simple beam under bending: surface patterning leading to twisting

Consider a square cantilever of diagonal length L (a side length $\sqrt{2}L/2$ and thickness h, as represented in figure (8.2.1)). Patterned with gold on the upper surface in a stripe across the diagonal, such that the gold extends a distance w up and across the cantilever from the left-hand bottom corner and a distance w

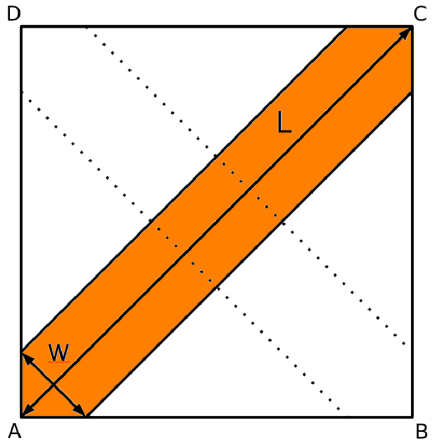

Figure 8.2.1: Schematic showing the axes and dimensions of a selectively patterned beam.

across and down from the right-hand top corner. Patterned on the lower surface with a stripe on the diagonal of the same area, joining the opposite corners.

I assume that an addition of energy resulting from adsorption to the gold stripe AC will result in an increase in surface stress across the whole beam and therefore pure bending across the whole beam in the direction A to C. Let us consider the bending on this square along the diagonal AC, ignoring for a moment any contribution from the stripe BD.

Let us adopt a coordinate system where the y-axis is along the diagonal AC, the x-axis is perpendicular to the neutral plane of the beam and the z-axis is along the diagonal BD.

Let us consider a volume element of the beam X at a height x above the neutral plane of the beam and a distance z from the diagonal AC but running parallel to it. This element will have initial length $y(z) = R\theta(z)$ and an increased post-bending length of $y_X(z) = (R+x)\theta(z)$. So, during bending, element X has been stretched through an elongation of $x\theta(z)$. The strain associated with this elongation is

$$\epsilon_X = \frac{x\theta(z)}{y(z)}. \tag{8.2.1}$$

As the whole beam is experiencing the same pure bending at any point z from the diagonal the radius of curvature will be the same for that element's specific length and degree of curvature. Thus we can write

$$\epsilon_X = \frac{x}{R}. \tag{8.2.2}$$

Which gives a strain energy per unit volume for element X of

$$\frac{U_{st_X}}{V_X} = \frac{1}{2}E'\epsilon_X^2 = \frac{E'x^2}{2R^2}. \tag{8.2.3}$$

If it has a depth dx and a width dz then element X has a volume $y(z).dz.dx$. So the strain energy for element X is

$$U_{st_X} = \frac{E'x^2y(z)dzdx}{2R^2}, \tag{8.2.4}$$

where $y(z) = (L - 2z)$ for a square.

So, for the whole beam, the strain energy due to bending is

$$U_{st} = \frac{E'}{2R^2}\int_{-\frac{h}{2}}^{\frac{h}{2}} x^2dx \int_{-\frac{L}{2}}^{\frac{L}{2}} (L - 2z)dz, \tag{8.2.5}$$

$$U_{st} = \frac{E'h^3L^2}{24R^2}. \tag{8.2.6}$$

The increase in energy associated with the stretching of the surface active layer is equal to the surface stress for the beam, σ, multiplied by the increased area which for an element of area on the surface, element D say, is $\frac{h}{2}\theta_D dz = \frac{hy(z)}{2R}dz$. So the area increase for the whole beam is

$$\int_{\frac{-L}{2}}^{\frac{L}{2}} \frac{h}{2R}(L - 2z)dz = \frac{hL^2}{2R}. \tag{8.2.7}$$

And the increase in energy due to stretching of the surface can be expressed

as

$$U_{su} = \frac{hL^2\sigma}{2R}. \tag{8.2.8}$$

Now sum these energies, differentiate with respect to R and set to zero to find an expression for the radius of curvature,

$$R = \frac{2E'h^2}{12\sigma}. \tag{8.2.9}$$

The displacement due to bending for any element will be $\delta = R(1 - cos(\theta))$

Working through this for the stripe on the bottom alone works out exactly the same.

If we include the effect of the anti-stripe on the lower surface of the beam and the stripe on the upper surface things come out a little different, which I will go through in detail later. However, if we consider that the values we really want to get out from this calculation are the displacements due to bending for the corners C and D, then if we recognise that because the diagonal AC bisects the diagonal BD then the action of each stripe on the diagonal has no effect on the action of the other stripe on the other diagonal. Of course, in saying that I have neglected the tangential effect of the stripes. But as the tangential effect of one stripe is in direct competition with the lateral effect of the other (for the section of the beam that they both cover) then the angle through which the diagonal AC is bent simply needs to be corrected by subtracting w (the width of the strip BD) from its length.

But, in order to get R, we need to know the new strain energy of the beam.

For the same element X, x above the neutral plane of the beam (for the upper stripe's bending, and x below for the lower stripe's effect), it is experiencing strain in both y and z directions.

For the y-direction

$$R\theta(z) \rightarrow (R + x)\theta(z), \tag{8.2.10}$$

so the strain is

$$\epsilon_{yX} = \frac{x\theta(z)}{y(z)} = \frac{x}{R}. \tag{8.2.11}$$

For the z-direction

$$Rd\theta \to (R - x)d\theta, \tag{8.2.12}$$

so the strain is

$$\epsilon_{zX} = \frac{-xd\theta}{dz} = \frac{-x}{R}. \tag{8.2.13}$$

Therefore the strain energy per unit volume of the element X is

$$\frac{U_X}{V_X} = \frac{1}{2}E'(\epsilon_{yX}^2 + \epsilon_{zX}^2) = \frac{E'x^2}{R^2}. \tag{8.2.14}$$

The volume of the element is $y(z).dz.dx$. Which gives a strain energy for the whole beam of

$$U_{st} = \frac{E'}{R^2}\int_{-\frac{h}{2}}^{\frac{h}{2}} x^2 dx \int_{-\frac{L-w}{2}}^{\frac{L-w}{2}} (L - 2z)dz = \frac{E'h^3L(L-w)}{12R^2}. \tag{8.2.15}$$

The increased surface of the active layers, top and bottom, will be twice that before, so the total energy of the beam can be written

$$U_{tot} = \frac{E'h^3L(L-w)}{12R^2} + \frac{hL^2\sigma}{R} = \frac{\alpha}{R} + \frac{\beta}{R^2}. \tag{8.2.16}$$

You can see from this expression that, when the width of the strip, w, is equal to the length of the side of the square, L, the strain energy term goes to zero. This makes sense, as the effects due to both faces of the beam will be in direct competition, exerting equal and opposite forces, and the resultant displacement will be zero.

By minimising U_{tot} with respect to R we find an expression for the radius of curvature,

$$R = \frac{E'h^2(L-w)}{6L\sigma}. \tag{8.2.17}$$

And, from this we determine the sensitivity of the angle of curvature to surface stress, as

$$\frac{d\theta}{d\sigma} = \frac{6L^2}{E'h^2(L-w)}. \tag{8.2.18}$$

For a square beam of silicon, with dimensions $320 \times 320 \times 0.9$ μm and a patterned strip width of 150 μm (giving approximately the same volume and active region area as the silicon beam in the previous example), this results in a sensitivity of 0.027 mN^{-1}. The curvature for a given stress is similar to that for a simply bending beam. However, the value we would actually be measuring in this case would be the angle through which the free end of the cantilever has rotated.

If each corner is deflected from the undeformed position by δ, assuming very small deflections, the angle of rotation about the midpoint of the end of the beam will be

$$\phi \approx arctan(\frac{2\delta}{L}), \tag{8.2.19}$$

which, for the square beam I am considering and, as an example, the decanethiol monolayer formation stress of 0.14 Nm^{-1} from chapter (5), corresponds to an angle of $\sim 0.2^{\circ}$. This response could be exaggerated, however, by increasing the separation of the corners of the free end, for example extending the part of the beam that is being monitored far beyond the active body of the cantilever; so there is no increase in the strain energy, but ϕ is maximised.

8.3 Effect of area of SAM: length of active surface

Recent work in my group at the London Centre for Nanotechnology, performed by J. Bailey and V. Turbe, aimed to use Micro Contact Printing (μCP) tech-

niques to study the geometric dependence of stress transduction, by patterning the cantilever with sensitive SAMs in a variety of ways. Their first results were for a setup with Mercaptoundecanoic acid (MUA) as the active 'ink' and Undecanethiol (UDT) to fill in the gaps. Terminating in a COOH group, MUA is responsive to changes in pH, whereas the CH_3 terminating group on UDT is not and as such, with its structural compatibility, fulfills the role of control in stress transduction experiments. Increasing pH will, through deprotonation of the MUA terminating oxygen, change its net charge to -1, leading to repulsive electrostatic forces across the surface of the cantilever. Under the influence of these titration experiments UDT will remain unchanged and can therefore be used to try and eliminate erroneous stress responses due to non-specific events.

Cantilevers functionalised both in capillaries and by μCP were fully characterised using scanning electron microscopy (SEM) and atomic force microscopy (AFM) techniques, and by studying the wetting properties of treated cantilevers. They found a good response to the patterning, producing cantilevers that were fully coated and a range of others with varying surface coverage from both the hinge end and free end.

Capillary functionalised cantilevers, displaying full monolayers, show a difference in stress response between MUA and UDT coatings of -10.745 mNm^{-1} upon experiencing a change from pH 4.8 to pH 9.0, showing good agreement with previous work [54].

These investigations were extended to look at how changing the geometric coverage of the 'active' MUA SAM on a cantilever affects the bending response. They took several measurements for cantilevers that had been patterned with MUA sections that covered the whole width of a cantilever, but varied in length along its long axis. This was done by increasing the length of the MUA section from the hinge end of the beam outwards and from its free end inwards. The two regimes show markedly different behaviour as the length of the section is increased, as in figure (8.3).

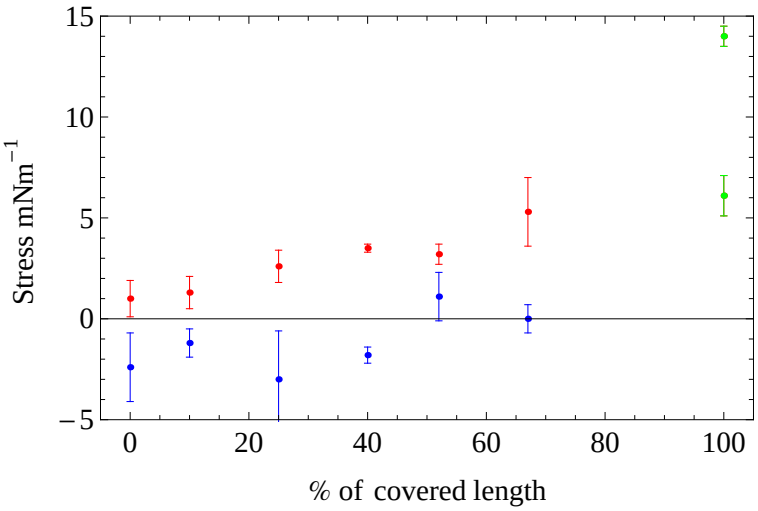

Figure 8.3.1: Figure showing the difference in behaviour experimentally obtained stress values for cantilevers patterned using μCP with varying lengths of 'active layer' extending from the hinge outwards (in red) and the free end inwards (in blue). The green markers are values of stress obtained from two separate cantilevers functionalised using microfluidic capillaries. Reproduced courtesy of J. Bailey.

Extending the MUA coverage from the hinge end outwards results in larger surface stresses that follow a roughly linear increase, but the same extension of MUA from the free end inwards shows a pretty negligible stress response even up to a coverage of around p= 0.7. In order to begin to explain this behaviour I will extend the figure of merit work on a bending beam from section (5.3.1) to one that may be bending with different radii of curvature in different sections.

If we consider a beam of length $L = L_1 + L_2$ with sections L_1 and L_2 coated with different SAMs, they both induce a different curvature in their respective beam sections. See figure (8.3.2) for a schematic of the setup. We can see that, assuming pure bending in each section, the end deflections, y_1 and y_2, of each section from their unstressed starting positions are given by,

$$y_1 = R_1(1 - cos(\theta_1)), \tag{8.3.1}$$

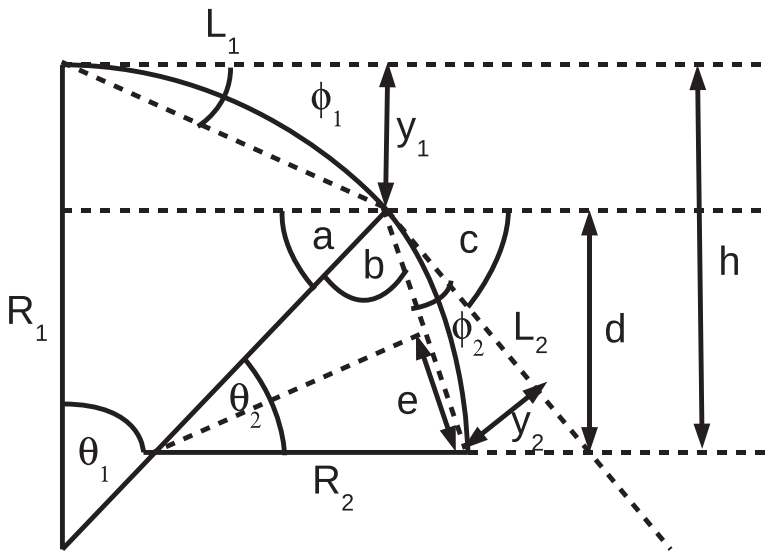

Figure 8.3.2: Schematic of a beam bending in two sections with two different radii of curvature; R_1 and R_2.

and, similarly

$$y_2 = R_2(1 - cos(\theta_2)). \tag{8.3.2}$$

However, because the curvature of the first section of the beam means that the second section's unstressed starting position is at an angle to the horizontal, finding the end deflection of the entire beam is more involved than simply adding these deflections. We need an expression for d, seen in figure (8.3.2), which will be

$$d = 2esin(c + \phi_2), \tag{8.3.3}$$

where

$$c = \pi - a - b - \phi_2, \tag{8.3.4}$$

$$sin(a) = \frac{R_1 - y_1}{R_1}, \tag{8.3.5}$$

$$= \frac{R_1 - R_1(1 - cos(\theta_1))}{R_1} = cos(\theta_1),$$

and

$$b = \frac{\pi - \theta_2}{2}. \tag{8.3.6}$$

Then as the chord of arc length L,

$$2e = 2R_2 sin\left(\frac{L_2}{2R_2}\right), \tag{8.3.7}$$

so

$$d = 2R_2 sin\left(\frac{L_2}{2R_2}\right).sin\left(\pi - sin^{-1}(cos(\theta_1)) - \frac{\pi - \theta_2}{2}\right). \tag{8.3.8}$$

For a beam experiencing no curvature in the second section we can see that this expression would collapse down to

$$d_{nocurve} = L_2.sin\left(\frac{\pi}{2} - sin^{-1}(cos(\theta_1))\right). \tag{8.3.9}$$

So, using the expressions for the deflection for the first section of the beam and the effective deflection, d, of the second section of the beam, we get an expression for the total deflection, h of

$$h = y_1 + d, \tag{8.3.10}$$

$$h = R_1(1 - cos(\theta_1)) + 2R_2 sin\left(\frac{L_2}{2R_2}\right).sin\left(\pi - sin^{-1}(cos(\theta_1)) - \frac{\pi - \theta_2}{2}\right). \tag{8.3.11}$$

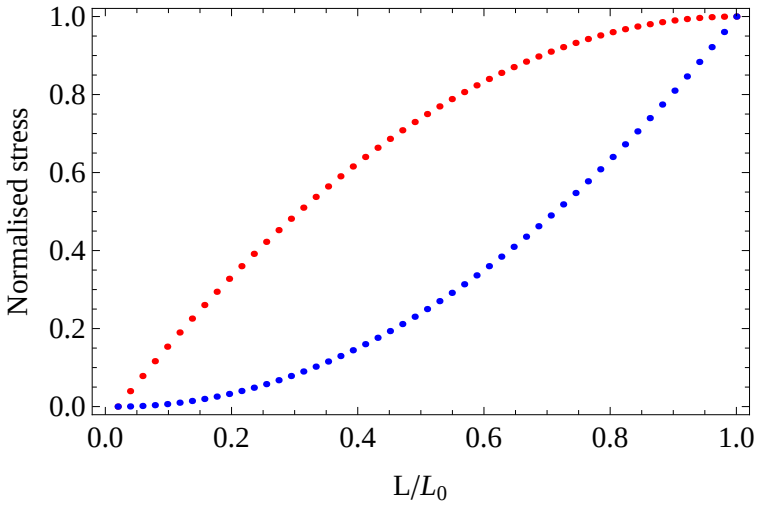

Figure 8.3.3: Normalised stress response of a cantilever as the active region is extended along its length, from the hinge outwards (in red) and from the free end inwards (in blue), as calculated using the model derived in this section.

Which all goes to zero when neither section is experiencing any curvature, as it should.

Plotting the response for the hinge and free end regimes, see figure (8.3.3) we can see that for extensions from the hinge end, while the curve describing the changing end deflection of the beam is not linear, it is increasing in a manner that could appear linear within experimental error bars. The curve showing the stress development as the active layer coverage is extended down the cantilever, while initially increasing slowly, does suggest that a deflection should be measurable much earlier than a coverage of p= 0.7.

The figures (8.3.4) show the fit of the model derived here to the experimental data for two situations. Subfigure (a) is calculated with the stress for the fully active layer covered beam taken as the average of the two, distinct, capillary functionalised responses. Subfigure (b) is for a fit to the lower value of those two stress responses. Both versions of the model fit show qualitatively similar behaviour to the experimental data. However, the fit to the lower value for full coverage stress is much better quantitatively, particularly for those results due

to patterning from the hinge end (in red). This suggests that those monolayers formed by μCP may correspond to a stress response at the lower end of the possible range for monolayers of this kind.

The correlation with the experimental data points for varying MUA coverage from the free end is not so close. The position of the data point at 0% coverage, where the error bars do not include the 0 stress baseline, suggest that these results may be offset by a common factor, possibly a consequence of an environmental factor or the nature of the MUA/UDT monolayer.

The importance of the underlying monolayer is once again underlined in these results. Both the method, and therefore mechanism, of adsorption and the positioning and segregation of adsorbates on the cantilever can have a significant effect. It is of great importance that the monolayers on the beam are properly characterised and controlled if the results obtained from the technology as used in this manner are to be meaningful and reproducible.

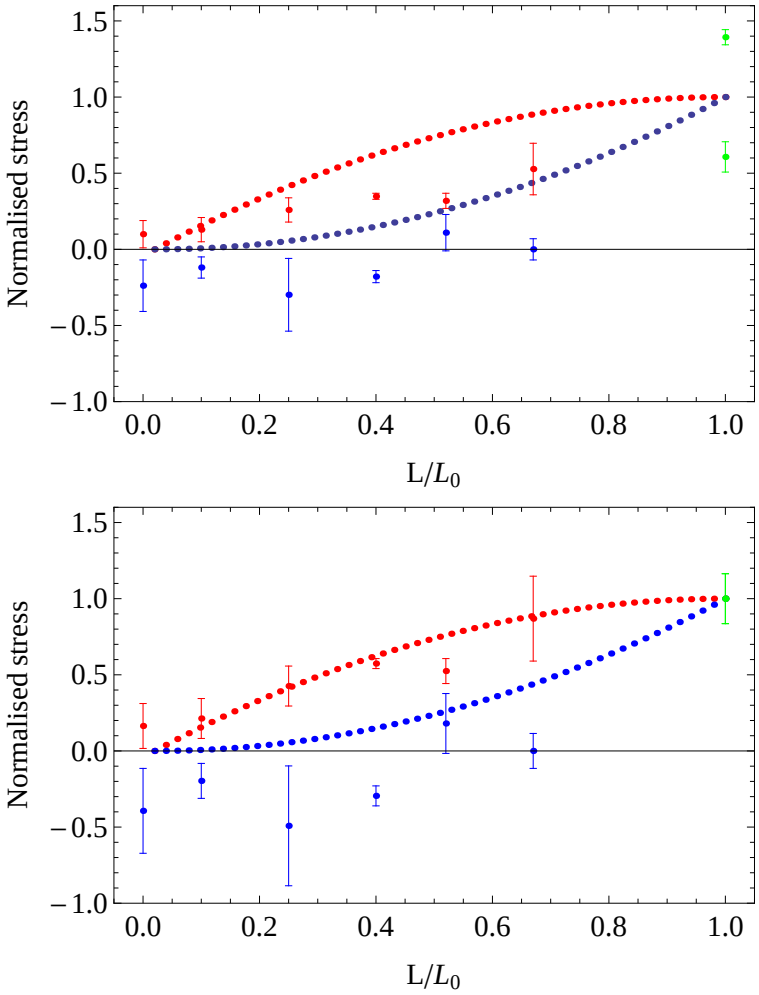

Figure 8.3.4: Plots showing calculated stress responses of cantilevers as the active region is extended along its length, from the hinge outwards (in red) and from the free end inwards (in blue). Plotted alongside experimentally obtained values for a full coverage stress, to which the values are normalised, of 10.05 mNm^{-1} (a) and of 6.1 mNm^{-1} (b). Data points reproduced courtesy of J. Bailey.

8.4 Effect of area of SAM: width of active surface

Another regime was explored by J. Bailey and J. Ndieyira during their measurements with UDT and MUA monolayers. They patterned one cantilever with a single stripe parallel to the long axis of the beam, that corresponded to a coverage of p $\approx 0.2 - 0.3$. This thin strip of MUA produces a deflection of the cantilever that corresponds to a surface stress of ≈ -10 mNm^{-1}, suggesting that a coverage this low can give rise to approximately the same signal as a fully covered beam.

One suggestion as to how this can be the case is to look at the beam as bending biaxially; taking into account now the stress tangentially across the beam as well as that longitudinally, which is in fact closer to reality, but has thus far been considered immaterial to the end deflection of the beam. The suggestion is that the tangential curvature of the beam stiffens it to longitudinal stresses, resulting in a lower end deflection. As an active, or stress producing, strip running down the length of the beam is narrowed, while the number of individual interactions will go down, the degree of bending tangentially across the cantilever will also reduce. It is possible that the opposing nature of these two effects could hold the end deflection of a cantilever approximately constant for even quite a large reduction in the width of the active strip.

In order to explore whether this hypothesis is valid I first approximate the cantilever as a biaxially bending beam with no end support, as the finding an analytical formulation for a beam of this sort held fixed at one end would be an extremely complicated undertaking. The simple formulation I shall be deriving as a preliminary investigation here will follow a very similar set of steps as in section (5.3.1).

The expression for the strain energy in a deformed plate, as derived by Landau and Lifshitz [178], is

$$U_{st} = \frac{E'}{2}\left(\epsilon_{ik}^2 + \frac{\nu}{(1-2\nu)}\epsilon_{ll}^2\right), \tag{8.4.1}$$

summing over indices, where ϵ_{ik} are the components of the strain tensor and ϵ_{ll} the diagonal components, E' is the biaxial modulus of elasticity and ν the Poisson ratio of the beam material.

Assuming no shear within the beam, and that, undergoing pure bending, the only strains across the beam correspond to either a compression or extension dependent on the distance from the neutral surface. If we set the coordinate axes such that the z-axis is the long axis of the undeformed beam; the y-axis is perpendicular to this and in the plane of the undeformed beam; and the x-axis is normal to the undeformed beam, then the strains we must consider are those due to extension/compression in the y- and z-directions

$$\epsilon_{zz} = \frac{x}{R_L}, \tag{8.4.2}$$

$$\epsilon_{yy} = \frac{x}{R_b}, \tag{8.4.3}$$

where x here is the height above, or indeed below, the neutral surface of the beam; R is radius of curvature; and the subscripts L and b specify whether it is the curvature along the length, L, of the beam, or across the width, b.

In the case of interactions on the thricely symmetric Au(111) surface, we can assume an isotropic stress and, therefore, equal radii of curvature along and across the beam, i.e. $R_L = R_b = R$. This simplification results in an expression for strain energy for a volume element X a distance x above the neutral surface of

$$\begin{aligned} U_{st,X} &= \frac{E'}{2}\left(\frac{x^2}{R^2} + \frac{x^2}{R^2} + \frac{\nu}{(1-2\nu)}\frac{x^2}{R^2} + \frac{\nu}{(1-2\nu)}\frac{x^2}{R^2}\right) \\ &= \frac{E'}{2}\left(\frac{2x^2}{R^2} + \frac{2\nu x^2}{(1-2\nu)R^2}\right) \\ &= \frac{E'}{2R^2}\frac{(2-2\nu)}{(1-2\nu)}x^2. \end{aligned} \tag{8.4.4}$$

And for the entire beam

$$U_{st} = \frac{E'}{2R^2}\frac{(2-2\nu)}{(1-2\nu)}Lb\int_{-h/2}^{h/2} x^2 dx, \tag{8.4.5}$$

where $Lbdx$ is the volume of element X,

$$\rightarrow U_{st} = \frac{E'(2-2\nu)Lbh^3}{24R^2(1-2\nu)}. \tag{8.4.6}$$

The increased area on the upper surface of the beam due to biaxial bending is the area post-deformation, $((R_L + (h/2))\theta_L)((R_b + (h/2))\theta_b)$, minus the area of the undeformed beam, $R_L\theta_L R_b\theta_b$, which gives

$$(h/2)^2\theta_L\theta_b + R_L\theta_L(h/2)\theta_b + R_b\theta_b(h/2)\theta_L, \tag{8.4.7}$$

which, if we say that the first term is of second order of smallness and can be neglected, gives an expression for the increase in surface energy due to bending of

$$U_{su} = \sigma(h/2)(L\theta_b + b\theta_L), \tag{8.4.8}$$

where σ is the surface stress (in units of Nm^{-1}). This can also be written in terms of the radius of curvature as

$$U_{su} = \frac{h\sigma Lb}{R}. \tag{8.4.9}$$

Summing equations (8.4.6) and (8.4.9), differentiating the expression with respect to the radius of curvature and setting equal to zero gives us an expression for the radius of curvature in terms of material properties and the increase in surface stress

$$R = \frac{E'(2-2\nu)h^2}{12(1-2\nu)\sigma}. \tag{8.4.10}$$

Now if we consider varying the width of the layer that is introducing the increased surface stress to the beam, so that it still runs the length L of the beam, but now at a width $f < b$. In this case, the radius of curvature of the

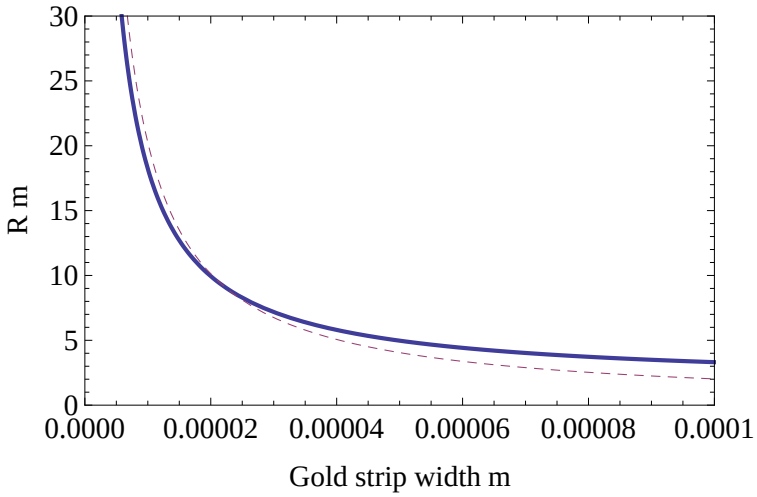

Figure 8.4.1: Plot showing the dependence of radius of curvature, R, on the width of the strip upon which the surface stress is acting of the radius of curvature of a beam considered to be bending only tangentially (dotted line) and one considered to be bending biaxially (thick line).

beam will be equal to

$$R = \frac{E'(2-2\nu)h^2(b+f)}{24f(1-2\nu)\sigma}. \tag{8.4.11}$$

In figure (8.4.1) I have plotted the radius of curvature of a beam of silicon ($E' = 150$ GPa, $\nu = 0.28$) with the same dimensions as the IBM cantilevers [15] used in the majority of experiments referred to in this work; $500 \times 100 \times 0.9$ μm. In this simplified model of the cantilever bending, adding in the effect of the tangential curvature on the end deflection of the beam does indeed reduce the curvature of the beam along its long axis at a full-width coverage of the active layer. In figure (8.4.1) this can be seen as an increase in the radius of curvature for the biaxial model. When biaxial bending effects are included it can also be seen that, as the width of the active strip is reduced to nothing, the radius of curvature increases at a slower rate than for the simple singly axially bending model. For the simpler model the difference in radius of curvature as the strip's width is reduced from $f = b$ to $f = \frac{b}{2}$ is $\Delta R = 2.03$, whereas the same reduction

for the biaxial model leads to $\Delta R = 1.66$. To put it more clearly, halving the width of the active strip results in the beam response dropping to 50% of that for a fully actively covered beam when only the curvature along the long axis is considered in the model. However, if one also considers the curvature across the cantilever, the response is a reduction to 67%.

Investigation into the potential effect of biaxial bending on the cantilever response is still in its preliminary stages here. However, the simple model appears to suggest that further exploration might yield important information about the elastic response of the beam, in order to better analyse measurements and even ways in which the devices could be optimised in terms of sensitivity. The next step with this work would be to include the effect of the support, which would most likely involve performing numerical finite element analysis (FEA) calculations to find approximate solutions of the equations governing this more complex bending pattern.

8.5 Conclusions

In this chapter I have begun to explore some of the variables that affect a cantilever's performance; the impetus from here must be not only on how to improve sensitivity, but also on ascertaining how the assumptions brought to bear on the current model for cantilever deflection hold up to reality. This includes looking at how the hinge section of the cantilever affects performance, the effect of bending in the transverse as well as longitudinal direction and how positioning, patterning and mixing of the 'active' chemical event sites on the beam translates to a stress effect.

Silicon based cantilevers are currently prevalent, exploiting the well developed commercial miniaturisation of similar products, as silicon chips for the computing industry. This chapter presented some evidence for the merit in exploring different materials, as well as geometries and functionalised patterning.

Chapter 9

Operating in viscous media

Biosensors, by their nature, often have to operate in varied environments that impact upon their mode of action. Whether it be the effects of ionic charge in the buffer solution in which they are immersed for measurements to be taken, or the potentially degrading effects of prolonged exposure to high temperatures or light through their actuation and transduction mechanisms, consequences of the environmental particulars of each scenario must be fully understood and accounted for in any theoretical model describing a biosensor response.

In this chapter I focus on one of the most urgent environmental considerations for the operation of nanocantilevers in their dynamic mode of action (see chapter (2)); the rheological properties of the operating medium.

I explore the effectiveness of two models developed by Sader et al [179, 180] in accounting for the effects of the flow field around a vibrating cantilever in a medium that is both dense and viscous. This is done by applying the models to frequency responses for nanocantilevers, of various aspect ratios, in ethanol and water solutions of different dilution, as obtained by members of my group at the LCN.

By examining the changes to the frequency response and working back, as it were, to use these data to ascertain values for the density and viscosity of each solution it is possible to gain a measure of the validity of both models and the

factors that can cause them to break down: where theoretical predictions show significant deviation from the actual behaviour of the system.

I first give some context for these measurements and characterise the theory behind each model. The relevant theory is then applied to R. Paxman's experimental results and discussed, along with some preliminary ideas on the potential for the technology and models' incorporation into point-of-care measurement systems.

9.1 Background

Examining the resonance frequencies of the normal modes of a vibrating cantilever can provide valuable information on changes to the medium in which the cantilever is vibrating and on changes to the cantilever itself. Changes in the density and viscosity of the medium in which a cantilever operates will result in a shift in the position of the peaks in the cantilever's resonance spectrum [181, 182].

Elucidating the manner in which viscous fluids truly affect a vibrating cantilever is complicated by the coupling of the effects of hydrodynamic loading and viscous drag, particularly when using beams on the nanoscale which could potentially enter the low Reynold's number regime [183].

9.1.1 Reynold's number

Reynold's number can be defined in slightly different ways. When one refers to a 'low Reynold's number regime', it is generally with one's mind on the ratio between the convective, time-independent inertial term of the Navier-Stokes equation and the viscous term [184]. This yields the expression $R = \frac{\rho v b}{\eta}$, where ρ is the density of the medium, η its viscosity and v and b the velocity and dominant length scale respectively of the object immersed in said medium.

This expression is useful conceptually, as a value of $R >> 1$ indicates dominating inertial forces and a value of $R << 1$ indicates dominating viscous forces.

For a typical cantilever, such as those used in the experiments described in this report, of width 100 μm oscillating at a fundamental frequency of $\approx$ 700 Hz at an amplitude of $\approx$ 500 nm in water, we get a value of $R \approx 1.5$. So the systems that I am interested in are subject to non-negligible contributions to flow behaviour from both inertial and viscous forces.

However, for an oscillating beam it makes more sense to describe the flow field using a Reynold's number, $Re = \frac{\rho\omega b^2}{4\eta}$ where ω is the angular frequency, derived from the ratio of time-dependent inertial forces to viscous forces.

This second expression is what I mean to refer to as 'Reynold's number' in all of the following, although it is sometimes referred to as the Valensi number in the literature [185].

9.1.2 Measuring rheological properties

The main reasons for considering cantilevers as potential density and viscosity sensors are their ability to perform rapid in-situ measurements and their need for only small sample volumes and probing areas. Traditional rheometers generally need a relatively large, specific setup to measure fluid properties. For example, those that force fluid through a capillary and monitor either flow rate or pressure [186]. Or those that use the drag forces on objects moving through viscous fluids, such as concentric rotating cylinders [186]. That a cantilever can be excited to oscillate thermally, and thus has no need for electrical contacts like piezoelectrically activated quartz crystal microbalances [187], is more promising for incorporation into LOAC devices [188, 84, 189].

Many models to describe media-induced damping of a cantilever's motion have been formulated that consider the medium to be inviscid in nature, i.e. there are no viscous forces on the beam [190, 191, 192, 193, 194, 195]. And indeed, for cantilevers down to about a millimetre in length, shifts in resonant frequency for most fluids have been found to be primarily dependent on the density of the fluid [196]; drag due to viscosity can be viewed as negligible. However, while this assumption can hold in many scenarios, as we approach

a low Reynold's number environment there is significant breakdown between theory and experiment [190, 191].

Significant work has also been done on models that include viscous effects but approximate the beam as a sphere [197, 198, 185]; discounting the specifics of geometry.

Models also exist that describe the 3-dimensional flow field around a cantilever beam accurately [199, 200], but using rather inaccessible numerical and computational techniques, which make them harder to incorporate into applications.

In the next sections I will be introducing two analytical formulations developed by J. Sader and C. Van Eysden. The first provides a model that accounts for a cantilever's cross-section explicitly and includes a viscous contribution to hydrodynamic loading [179]. I will be exploring where this model breaks down and its extension, via the second model, to account for the marked damping dependence on the vibrational mode number [180].

9.1.3 The frequency response

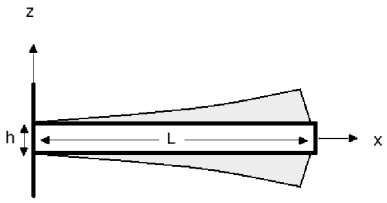

Figure 9.1.1: Schematic outlining the axes and labelling of a cantilever beam executing flexural oscillations in the x-z plane.

Consider a cantilever of rectangular cross section, length L, width b and height h executing flexural oscillations with deflection in the z direction, as in figure (9.1.1). For the moment we aren't considering the torsional modes of vibrations and are assuming that the two modes of vibration are not coupled in

any way. The governing equation for elastic deformation of such a beam can be written as

$$F(x,t) = EI\frac{\partial^4 w(x,t)}{\partial x^4} + \mu\frac{\partial^2 w(x,t)}{\partial t^2}, \tag{9.1.1}$$

where $w(x,t)$ is the deflection function along the length of the beam, E is the Young's modulus, $I = bh^3/12$ is the moment of inertia for a rectangular beam, $\mu = \rho_c bh$ is the mass per unit length of the beam, $F(x,t)$ is the external applied force per unit length, ρ_c is the cantilever density and x and t are the spatial and temporal variables respectively.

For this cantilever setup (one fixed and one free end), the boundary conditions are:

$$\left[w(x,t)\right]_{x=0} = \left[\frac{\partial w(x,t)}{\partial x}\right]_{x=0} = \left[\frac{\partial^2 w(x,t)}{\partial x^2}\right]_{x=L} = \left[\frac{\partial^3 w(x,t)}{\partial x^3}\right]_{x=L} = 0. \tag{9.1.2}$$

The external applied load on a cantilever vibrating in a fluid can be separated into contributions from the driving force exciting the resonances in the beam and the hydrodynamic loading due to the fluid flow around the cantilever as it moves. The expression below depends on frequency instead of time, it is convenient to Fourier transform the governing equation in order to solve it to find the resonant frequencies, equation (B.0.28), and so I refer to the external force as frequency dependent.

$$\hat{F}(x,\omega) = \hat{F}_{hydro}(x,\omega) + \hat{F}_{drive}(x,\omega) \tag{9.1.3}$$

The hydrodynamic term, shown below, is derived from the Navier-Stokes equations [201] and corresponds to the force due to loading on a beam in an inviscid fluid with an additional factor, Γ, quantifying the relative importance of inertial and viscous forces,

$$\hat{F}_{hydro}(x,\omega) = \frac{\pi}{4}\rho\omega^2 b^2 \Gamma^f(\omega,n) w(x,\omega) \tag{9.1.4}$$

The hydrodynamic factor is dependent on the frequency of oscillation, ω, through the Reynold's number

$$Re = \frac{\rho \omega b^2}{4\eta}. \tag{9.1.5}$$

Sader has shown that when assuming low dissipative effects, the frequency response of a cantilever in a viscous medium can be well approximated by a simple harmonic oscillator (SHO). In such a regime the resonant frequency ω of mode n and the quality factor Q are given by

$$\frac{\omega_{R,n}}{\omega_{vac,n}} = \left(1 + \frac{\pi \rho b^2}{4\mu} \Gamma_r(\omega_{R,n})\right)^{-\frac{1}{2}}, \tag{9.1.6}$$

$$Q_n = \frac{\frac{4\mu}{\pi \rho b^2} + \Gamma_r(\omega_{R,n})}{\Gamma_i(\omega_{R,n})}, \tag{9.1.7}$$

which can be solved simultaneously to find both the density and viscosity of the medium in which the beam is resonating.

In the following sections we explore two models developed to find an analytical expression for Γ to describe the velocity field around a vibrating cantilever: a 2-D flow field that corresponds to an infinitely long beam, the extension of that model to a 3-D flow field and the break-down point at which the two diverge. Throughout we will be making the following assumptions.

- The cross section of the beam is uniform along its entire length
- $L \gg b \gg h$ (which could prove problematic for some devices and will be discussed at greater length later in this chapter). $L \gg b$ in order that the approximation to an infinitely long beam is appropriate; $L \gg h$ in order that we are able to use classical beam theory [178] to describe motion of the cantilever, were $\frac{L}{h}$ to approach 20 or less shear would play a non-negligible role in the problem and we would have to instead use Timoshenko beam theory [202] or similar.
- The amplitude of vibration is smaller than any of the length scales of

the beam (Since this is the case we can assume that nonlinear convective inertial effects are negligible compared to linear effects.)

- Internal dissipative effects in the beam can be ignored
- The fluid can be considered incompressible
- Dissipative effects due to the fluid are negligible: i.e. Q-factor is $\gg 1$. This constraint dictates how well the approximation of the cantilever to a simple harmonic oscillator fits with reality. While some of our quality factors approach 1, there are none that fall below unity, and so we can consider the SHO approach to be appropriate, with only slight reservations.

9.1.4 The hydrodynamic function

Model 1, developed by J. Sader in the late nineties [179], presents a correction term for the exact analytical result for the hydrodynamic function Γ for a beam of circular cross section. By approximating a beam of rectangular cross section as an infinitely long beam of identical cross section this model can be applied to the fundamental (and next few harmonic) modes of said beam, provided that $L \gg b$. The hydrodynamic function developed in this model is:

$$\Gamma_{rect}(\omega) = \Omega(\omega)\Gamma_{circ}(\omega) \tag{9.1.8}$$

where $\Gamma_{circ}(\omega) = 1 + \frac{4iK_1(-i\sqrt{iRe})}{\sqrt{iRe}K_0(-i\sqrt{iRe})}$ and the Ks are modified Bessel functions of the third kind, and

$$\Omega(\omega) = \Omega_r(\omega) + i\Omega_i(\omega), \tag{9.1.9}$$

corresponding to the numerical corrections [179].

9.1.5 An extended model

This second model [180] is an extension, by C. Van Eysden and J. Sader, of Model 1 (9.1.4) to account for the 3-D nature of the flow field. As mode num-

ber increases, the longitudinal distance over which the velocity field varies approaches the dominant length scale of the aforementioned model, which is the width b of the beam. This can be accounted for by including a second parameter in the hydrodynamic function, the 'normalised mode number', $\kappa = C_n \frac{b}{L}$ where C_n is the nth positive root of equation (B.0.27).

The model is formulated such that when $\kappa \ll 1$ the result corresponds to that for oscillations of a rigid beam. For larger values of κ the results obtained correspond to sinusoidal oscillations. It is important that the model varies with κ rather than just the mode number, n, as the geometry of the cantilever also affects the fluid response.

In this model the Reynold's number differs by a factor of 4, $Re = \frac{\rho\omega b^2}{\eta}$, as this definition appears in the exact analytical solution as obtained from the linearised Navier-Stokes equation [201].

When considering the full 3-D flow field around the beam, the hydrodynamic function, Γ, quantifying the subsequent load on a cantilever, can be written as

$$\Gamma^f(\omega, n) = 8a_1 \tag{9.1.10}$$

and is obtained by solving the linearised Navier-Stokes equation for the oscillations of a flexible thin blade of infinite length.

The coefficient a_1 can be found by solving the following system of linear equations:

$$\Sigma_{m=1}^{M}(A_{q,m}^{\kappa} + A_{q,m}^{Re})a = \begin{cases} 1, & q = 1 \\ 0, & q > 1 \end{cases}, \tag{9.1.11}$$

$$A_{q,m}^{\kappa} = \frac{-4^{2q-1}}{\sqrt{\Pi}}\, G_{13}^{21}\left(\frac{\kappa^2}{16}\middle|_0 \begin{matrix} 3/2 \\ q+m-1 \;\; q-m+1 \end{matrix}\right), \tag{9.1.12}$$

$$A^{Re}_{q,m} = -\kappa^2 \frac{2^{4q-5}}{\sqrt{\Pi}} G^{21}_{13}\left(\left.\frac{\kappa^2 - iRe}{16}\right|_0 \begin{matrix} 1/2 \\ q+m-2 \; q-m \end{matrix}\right) - \frac{2^{4q-1}}{\sqrt{\Pi}} G^{21}_{13}\left(\left.\frac{\kappa^2 - iRe}{16}\right|_0 \begin{matrix} 1/2 \\ q+m-1 \; q-m+1 \end{matrix}\right), \quad (9.1.13)$$

where the Gs are Meijer functions [203].

The time it takes to find Γ from these equations depends upon the size of the matrix in equation (9.1.11), which is dictated by M. M must be increased until the result for Γ is converged to within the desired accuracy. Convergence of these analytical solutions has been systematically explored in [204]. They find an approximate analytical expression, an M_{critical} that achieves a 99% convergence in results, of $M_{\text{critical}} \approx \text{Max}(1 + \sqrt{\kappa}, \frac{1}{3}\sqrt{Re})$. The Re and κ at which we are working do not necessitate huge matrices, however calculation times stretch to over 20 minutes. While this can be considered an acceptable time to wait for a result as a researcher sat at a powerful computer, it severely limits the model's applicability to in-situ, point of care measurements.

9.2 Application to water-ethanol solutions

While these models have their uses in predicting the changes to an oscillating beam's resonance frequencies upon immersion in a fluid, we are interested here in working the other way; in using measured frequencies and quality factors and knowledge of the geometric and material qualities of the beam to elucidate the rheological properties of the fluid. Namely the density ρ and viscosity η, which are included in the equation of shifted frequency in the Reynold's number.

To test the viability of the models R. Paxman looked at solutions of water mixed with varying amounts of ethanol. Cantilevers of four different geometries were used to obtain the results: the Array cantilevers (500:100:0.9 μm); the Long Veeco (400:30:2 μm); the Medium Veeco (200:30:2 μm); and the Small

Veeco (100:30:2 μm).

The error bars on the plots in figures (9.2.2) and (9.2.3) are there to give an indication of how much results can vary from measurement to measurement. The bars show the effect of the variation of frequency and quality factor over multiple measurements for each cantilever. 24 measurements (three arrays each with eight cantilevers) were taken for the Array cantilevers; three measurements for the Long and Medium Veeco cantilevers and two measurements with the Small Veeco cantilever.

There may be a small degree of variability between the solutions for the Array and Veeco measurements, as they were taken on separate days and the solutions remixed. However, both the Array and Veeco measurements were completed within separate 36 hour periods, during which there was no appreciable change in temperature (kept at the laboratory working temperature of 20°C). So you can see that even within a controlled environment, there could be a high degree of uncertainty, particularly on a single measurement.

9.2.1 Applying model 1

Implementation of the extended model to the data acquired from ethanol/water solutions of 0, 20, 40, 50, 60, 80, and 100% ethanol content is achieved using a Mathematica algorithm to solve equations (9.1.6) and (9.1.7) for density (ρ) and viscosity (η). For this set of calculations the hydrodynamic function is formulated as in equation (9.1.8).

The data in figures (9.2.2) and (9.2.3) have been plotted with the spatial wavelength of the oscillating cantilever, $\lambda_{\text{eff}} = \frac{2\pi L}{C_n}$, against b on the abscissa to clearly demonstrate that the model becomes less applicable for higher modes.

9.2.2 Discussion

Looking back at the model we see that there is no explicit dependence on the mode number, n, of the resonance peak. However, a different mode shape, with a different number of nodes, as can be seen for the first four modes in figure

(9.2.1), directly impacts on the motion of the surrounding fluid.

Higher flexural modes have more nodes along the length of the cantilever, they are experiencing smaller deflections than the first mode. As a result, they are moving less water around with them, their hydrodynamic load is less [191]. But the 1998 model has no dependence on mode number and therefore overestimates the hydrodynamic load on the cantilever at higher modes. The deviation of the model from reality can be seen in figures (9.2.2) and (9.2.3), and is particularly clear for the density results.

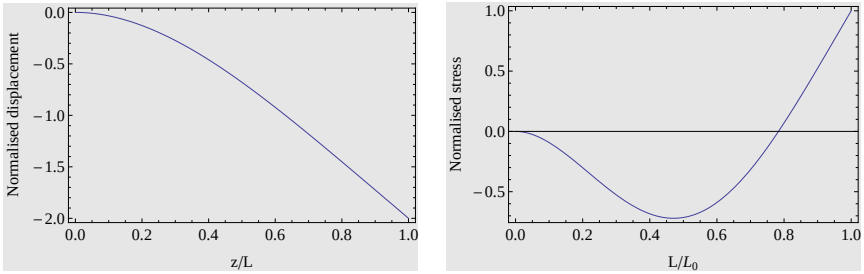

(a) Mode 1

(b) Mode 2

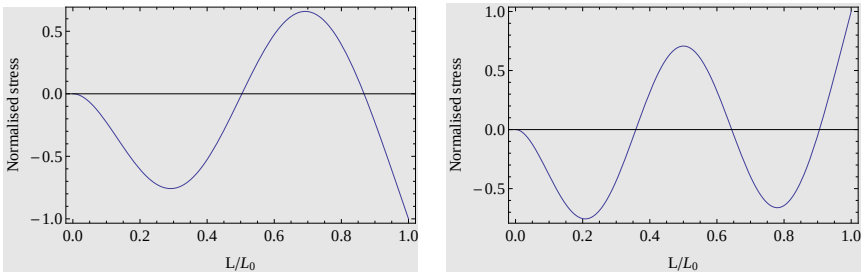

(c) Mode 3

(d) Mode 4

Figure 9.2.1: Mode shapes as described by a vibrating cantilever.

So the main drawback in using this model is that it contains no explicit dependence on the mode order. For an arbitrary mode, far from the fundamental resonance, the model is not representative, as it doesn't account for the possibility that the velocity field's length scale of variation along the longitudinal axis of the cantilever could approach the dominant length scale of the problem, taken in this instance as the cantilever's width, b.

A similar breakdown at higher modes can be seen in work by Maali et al [200], formulated in a similar way from the approximation to an infinitely long and thin beam. In this paper the breakdown is shown as an added mass value and a damping coefficient, and calculated up to mode 8.

Of course, this only becomes an issue should you want to use modes of $n >> 1$. Most measurements in the literature use only the first, and occasionally the second, mode to obtain information on the rheology of samples. Measurements of the viscosity of sucrose have been obtained to within 5% of literature values using the first mode [205, 206], and comparable measurements for water, ethanol [207] and even complex fluids [87]. Simultaneous measurements of viscosity and density have been obtained for a wide range of gases and liquids [208], and even for water/ethanol solutions [209], but using the simplified generalised sphere approach, not accounting for cantilever geometry or mode number.

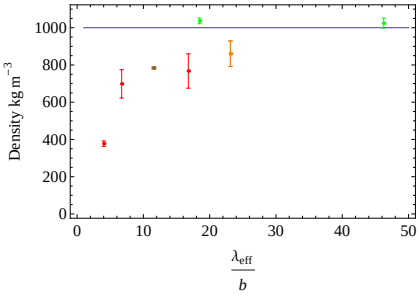

(a) Pure water

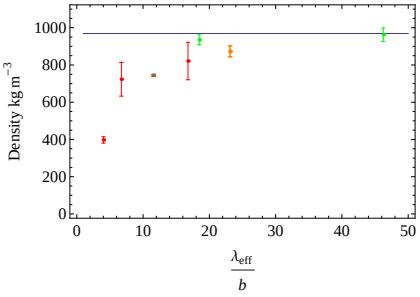

(b) 80:20 % water:ethanol solution

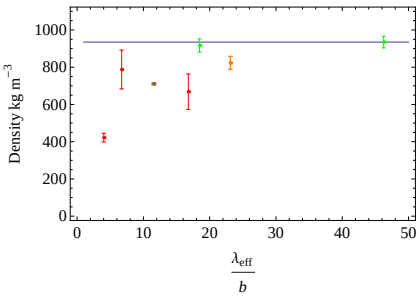

(c) 60:40 % water:ethanol solution

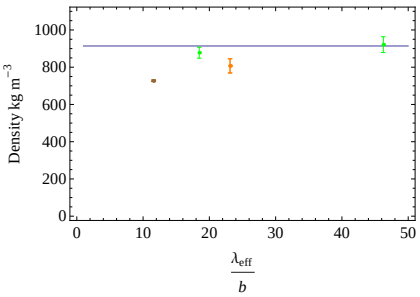

(d) 50:50 % water:ethanol solution

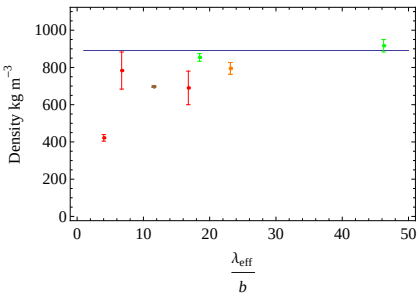

(e) 40:60 % water:ethanol solution

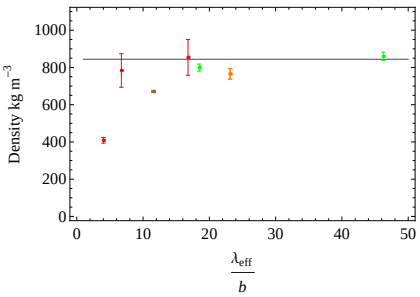

(f) 20:80 % water:ethanol solution

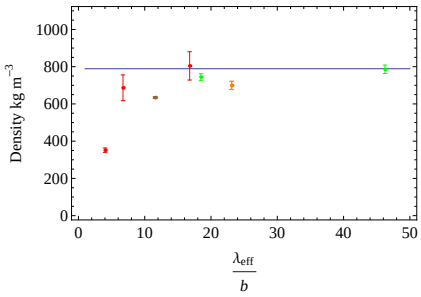

(g) Pure ethanol

Figure 9.2.2: Densities for a range of water/ethanol solutions, as calculated by the model outlined in section (9.1.4). Values shown for the Array cantilever (red), the Long Veeco cantilever (green), the Medium Veeco cantilever (orange) and the Small Veeco cantilever (brown). The literature density value is given by the thin blue line.

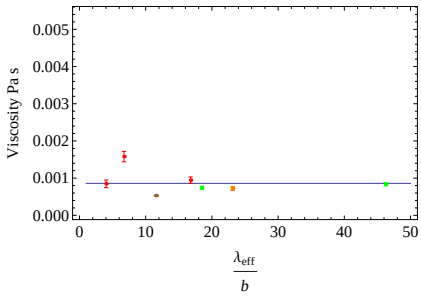

(a) Pure water

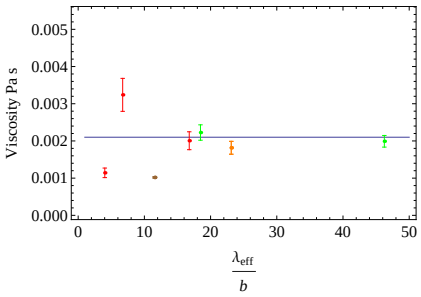

(b) 80:20 % water:ethanol solution

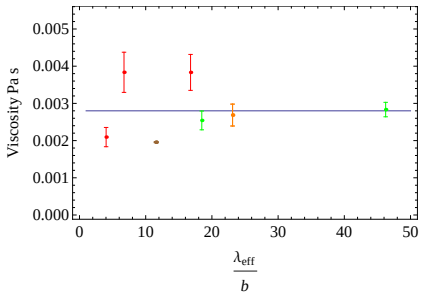

(c) 60:40 % water:ethanol solution

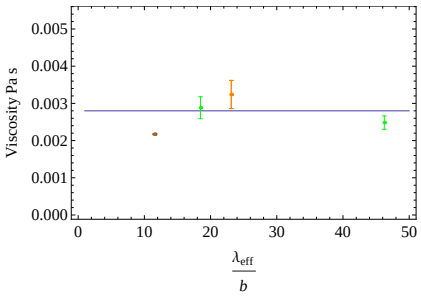

(d) 50:50 % water:ethanol solution

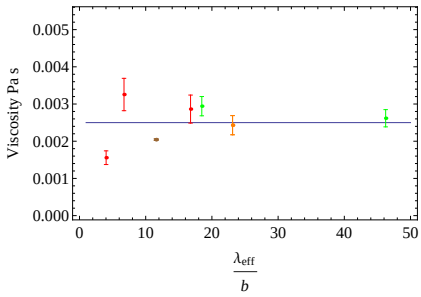

(e) 40:60 % water:ethanol solution

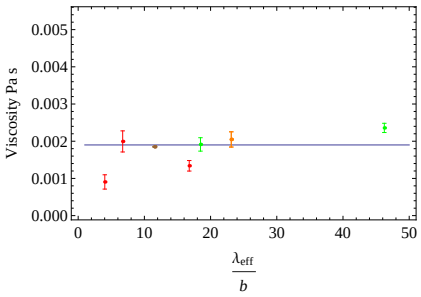

(f) 20:80 % water:ethanol solution

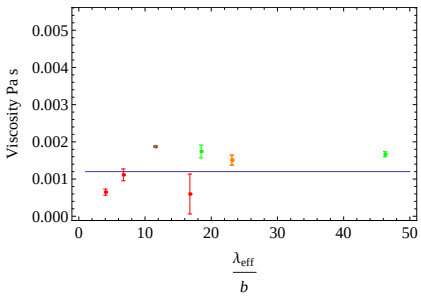

(g) Pure ethanol

Figure 9.2.3: Viscosities for a range of water/ethanol solutions, as calculated by the model outlined in section (9.1.4). Values shown for the Array cantilever (red), the Long Veeco cantilever (green), the Medium Veeco cantilever (orange) and the Small Veeco cantilever (brown). The literature viscosity value is given by the thin blue line.

But utilising higher modes can be an attractive approach for several reasons [210, 200, 211]. For example, in applications that use tapping mode AFM, operating at higher modes has proved more sensitive to the mechanical properties [212] and surface charge density [213] of a sample. As you move to higher modes, the quality factor of oscillation will significantly increase [214] which means the approximation of the beam to a simple harmonic oscillator, made in section (9.1.4), is more accurate. Also, recent work by Dohn et al [60] into deconvoluting both the mass and position of more than one particle attached to an oscillating cantilever, shows the necessity of obtaining information from as many modes as there are degrees of freedom in the problem.

These limits are acknowledged in the Sader paper [179], where they expressly point out the applicability of the model only to the fundamental and next few subsequent modes, and accounted for in a later paper by C. Van Eysden and J. Sader [180] where they have included a parameter directly dependent on mode number, κ, and looked at the 3-D variation of the velocity field in the medium. Application of this newer model, which is further described in section (9.1.5), to our experimental results should eliminate this drift away from the true ρ and η as we explore higher modes.

9.2.3 Applying model 2

Implementation of the extended model to the data acquired from ethanol/water solutions of 0, 20, 40, 50, 60, 80, and 100% ethanol content is achieved using a Mathematica algorithm to solve equations (9.1.6) and (9.1.7) for density (ρ) and viscosity (η). For this set of calculations the hydrodynamic function is formulated as in equation (9.1.10).

The results in figures (9.2.6) and (9.2.7) show the densities and viscosities calculated using this extended model, alongside the original results calculated in section (9.1.4). For those cantilevers whose only measurement was of the first mode, the difference between the results from the two models is minimal, as to be expected. However, if we look at the results for the Array cantilever,

which has measurements for modes 1, 2 and 3, the increasing difference in the calculated results as we move up the modes can be clearly seen.

9.2.4 Discussion

To illustrate the discrepancies between the two models, figures (9.2.4) and (9.2.5) show the percentage difference between Model 1 and Model 2 for the real and imaginary parts of Γ respectively, plotted against the ratio of effective wavelength of the beam's oscillatory motion to its width. The breakdown between Model 1 and Model 2 can be clearly seen as λ_{eff} approaches the width of the beam.

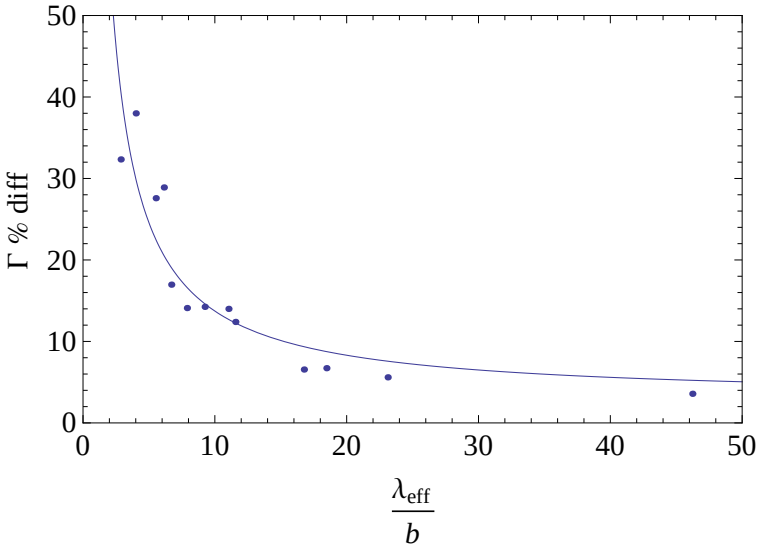

Figure 9.2.4: Figure showing the percentage difference in the real part of the hydrodynamic function between Model 1 and Model 2 plotted against the ratio between cantilever effective wavelength and width.

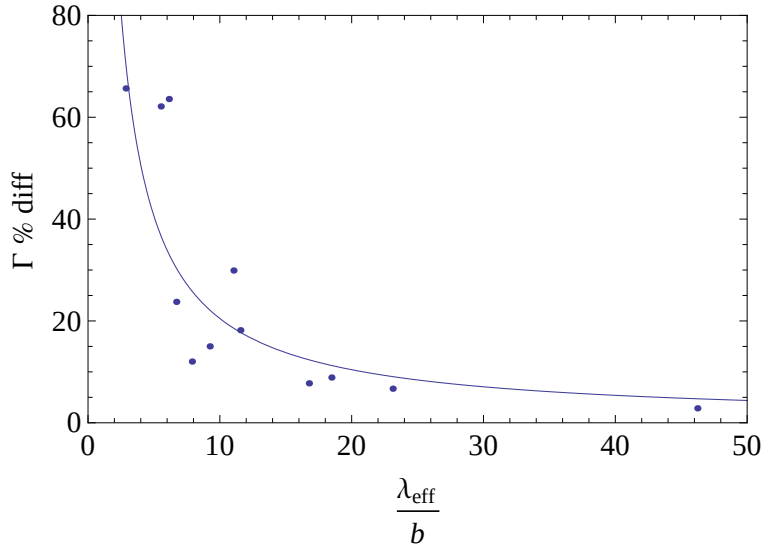

Figure 9.2.5: Figure showing the percentage difference in the imaginary part of the hydrodynamic function between Model 1 and Model 2 plotted against the ratio between cantilever effective wavelength and width.

For example, for the real part of the hydrodynamic function from Model 1 to agree with Model 2 within $\sim 10\%$, the effective wavelength of the beam must be ~ 15 times larger than its width. This requirement is violated at n = 3 for the Long Veeco cantilever. For the other cantilevers this threshold is passed much earlier, as a shorter λ_{eff} can be due either to an increased mode number or to cantilever length. In the case of the latter, however, other important considerations come to bear on the situation.

While the Long Veeco cantilever results are mostly consistent with the literature values for density and viscosity, the cantilevers of lower aspect ratio deviate to a varying degree. This effect, that as the cantilevers become shorter the model's accuracy in describing the response decreases, is brought about by the deviation of the actual set-up from those assumptions required to successfully approximate our beam to one of the same cross-section but infinite length.

At small ratios of length to width, both the governing equation for the elastic deformation of the beam, equation (9.1.1), and the expression for the force

due to loading, equation (9.1.4), are no longer formally exact [190]. Additionally, dissipative effects become more important for shorter beams [207] and the approximation to a SHO is not valid. Thus, at small aspect ratios the models break down and results from calculations are unreliable. This is quite possibly what we are seeing with some of the shorter cantilevers in this study, and means that even including mode number dependence, as in the second model, will still yield incorrect values for ρ and η.

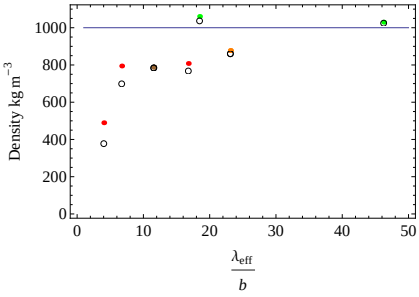

(a) Pure water.

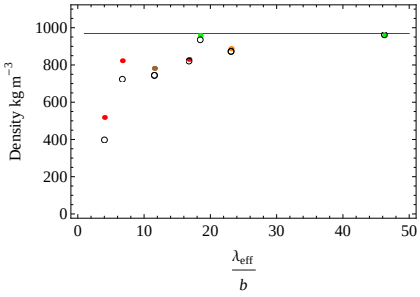

(b) 80:20 % water:ethanol solution.

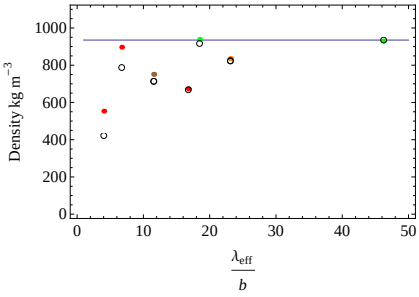

(c) 60:40 % water:ethanol solution.

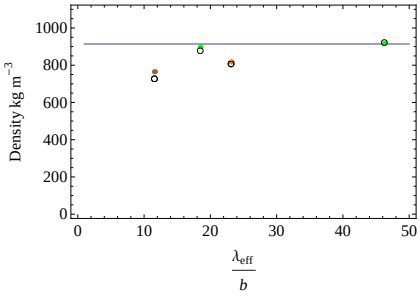

(d) 50:50 % water:ethanol solution.

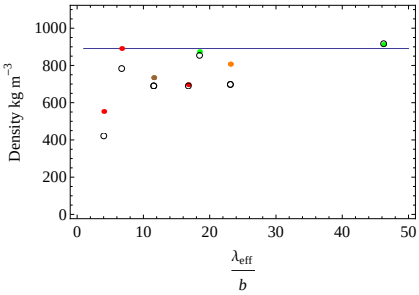

(e) 40:60 % water:ethanol solution.

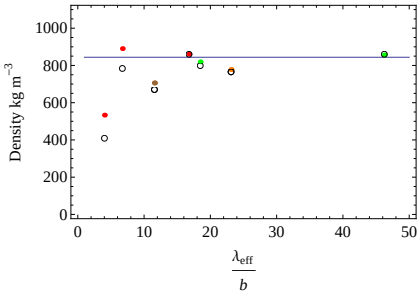

(f) 20:80 % water:ethanol solution.

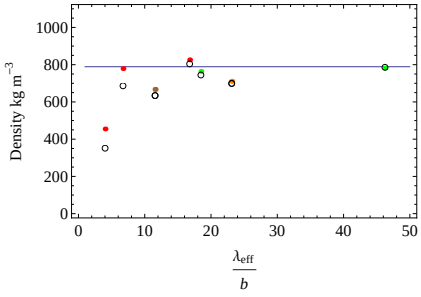

(g) Pure ethanol.

Figure 9.2.6: Comparison between densities calculated using the model outlined in section (9.1.5) (solid discs) and those calculated using the model outlined in section (9.1.4) (empty circles). Values shown for the Array cantilever (red), the Long Veeco cantilever (green), the Medium Veeco cantilever (orange) and the Small Veeco cantilever (brown). The literature density value is given by the thin blue line.

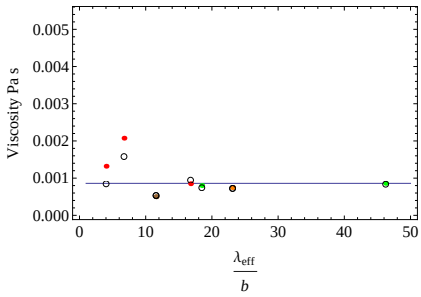

(a) Pure water.

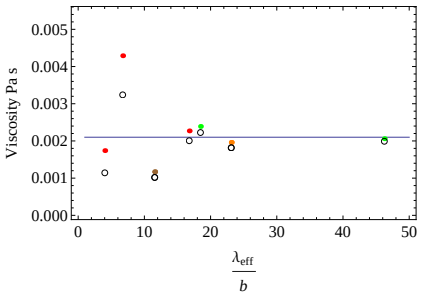

(b) 80:20 % water:ethanol solution.

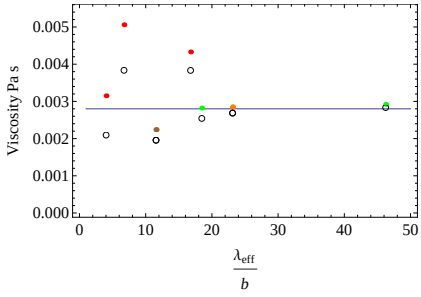

(c) 60:40 % water:ethanol solution.

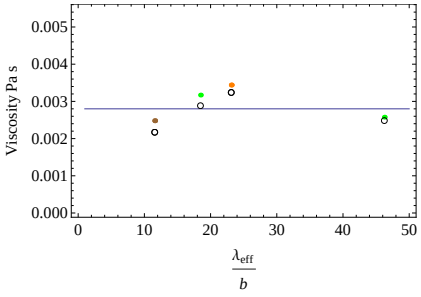

(d) 50:50 % water:ethanol solution..

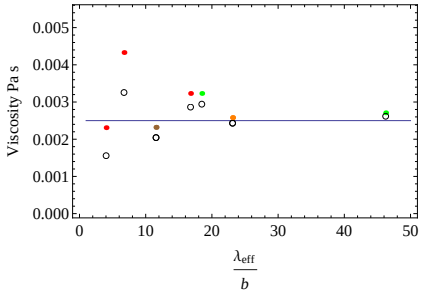

(e) 40:60 % water:ethanol solution.

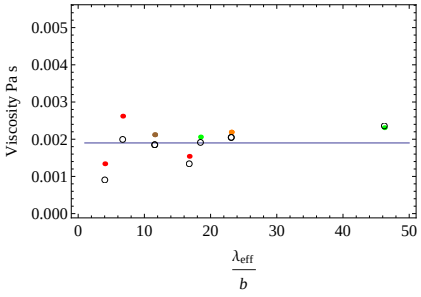

(f) 20:80 % water:ethanol solution.

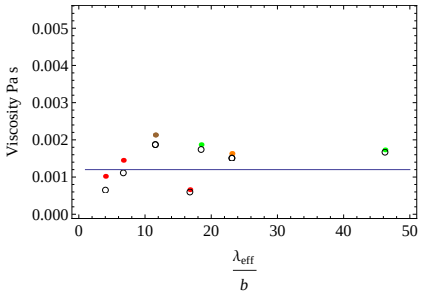

(g) Pure ethanol

Figure 9.2.7: Comparison between viscosities calculated using the model outlined in section (9.1.5) (solid discs) and those calculated using the model outlined in section (9.1.4) (empty circles). Values shown for the Array cantilever (red), the Long Veeco cantilever (green), the Medium Veeco cantilever (orange) and the Small Veeco cantilever (brown). The literature viscosity value is given by the thin blue line.

There is value in looking in detail into two different breakdown models with regards to the theoretical formulations outlined in this chapter. To explore systematically how the hydrodynamic functions of the two models diverge with κ, so applications wishing to exploit the simpler and faster first model have a clearer idea of what mode a cantilever of a certain aspect ratio may operate in without a significant deviation in Γ. Also, a rigorous study of when the analytic expressions describing the beam's deformation and loading become unusable, so as to place a firm lower limit on the length of cantilevers used for such purposes as these.

A potential application of the first breakdown model is outlined in the next section of this chapter. The amount of experimental data points presented in this report are not, to my mind, comprehensive enough to formulate the second breakdown model. However, this is a direction that might be explored with more measurements, taken systematically with cantilevers of varying lengths.

9.3 Reducing the computing time

In order to eliminate the lengthy calculation times involved in using Model 2, but to retain the accuracy of said model, it is sensible to formulate a simpler function that accounts for the discrepancy between Models 1 and 2. This is done by taking the following steps.

First, the hydrodynamic function Γ, as described in Model 1, is calculated for a range of Re (10^{-4}-10^{4}) that comfortably covers the range of density and viscosity in which we are working. The same is done for Model 2, but of course this time we calculate Γ over a range of Re and of κ, with κ varying from 0 to 20. By subtracting the Re dependent Γ values of Model 1 from those for each value of κ of Model 2, we discover how the difference between the models depends upon rheology and the dimensions of the beam. We know the width and length of the beam and, by measuring the frequency and Q factor of the beams various modes in the medium, can use Model 1 to find the Reynold's number.

We calculate the hydrodynamic function for the measured properties according to Model 1. This value is referenced back to the calculated list of Γ for the model and yields a value for Re.

Now, equipped with both κ and Re we can look up the correction term for the hydrodynamic function, as calculated previously.

This corrected Γ can be substituted back into Model 1, and the whole solved for ρ and η.

The results can be seen in figures (9.3.1) and (9.3.2), as compared with those calculated using the full Model 2 formulation. The approximation is good, with all values of ρ from the interpolating function lying within 5% of the Model 2 values and the majority of values of η within 10%. They are all calculated in a fraction of the time as well. The time taken to find ρ and η using Model 2 is dependent on the size of the matrix in equation (9.1.11). So, the biggest cut in calculation time will correspond to the data set with the highest value of either κ or Re, which is that for the first mode of the Small Veeco cantilever in 100% ethanol. While the full calculation for this data set takes over 20 minutes, the approximated value is found in under 0.5 seconds. Even for the quickest calculation using Model 2, that for the first mode of the Array cantilever in water, the calculation time drops from 27 seconds to just over 0.1 seconds.

The next step to be taken with this would be to extend the approximate model to media of different Reynold's numbers and ascertain how well it copes with measurements taken for much higher modes of $n >> 1$. Having access to more experimental data, for a range of media and cantilever geometries, would also enable the formulation of an easily applicable breakdown model to inform design and incorporation of cantilevers operating in viscous and complex biological media into point of care devices.

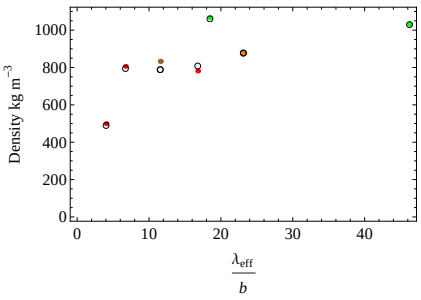

(a) Pure water.

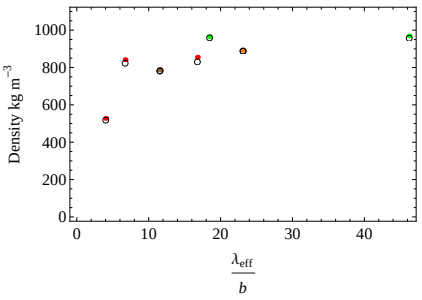

(b) 80:20 % water:ethanol solution.

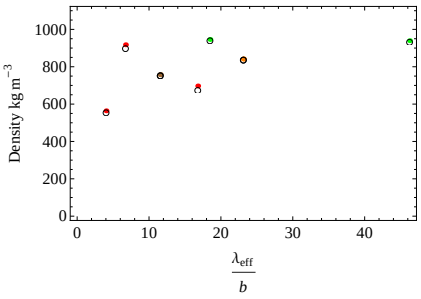

(c) 60:40 % water:ethanol solution.

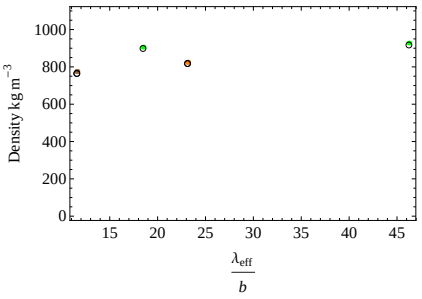

(d) 50:50 % water:ethanol solution.

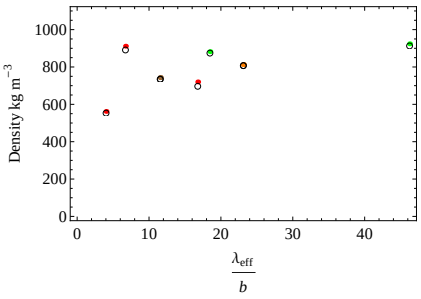

(e) 40:60 % water:ethanol solution.

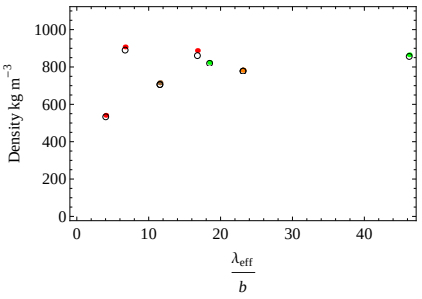

(f) 20:80 % water:ethanol solution.

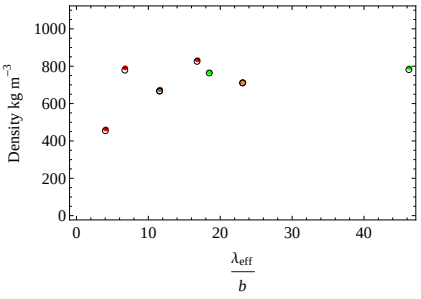

(g) Pure ethanol.

Figure 9.3.1: Comparison between densities calculated using the model outlined in section (9.1.5) (empty circles) and the approximated values (solid discs). Values shown for the Array cantilever (red), the Long Veeco cantilever (green), the Medium Veeco cantilever (orange) and the Small Veeco cantilever (brown).

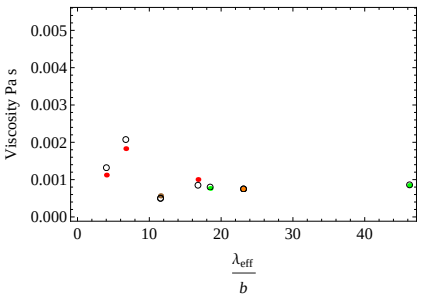

(a) Pure water.

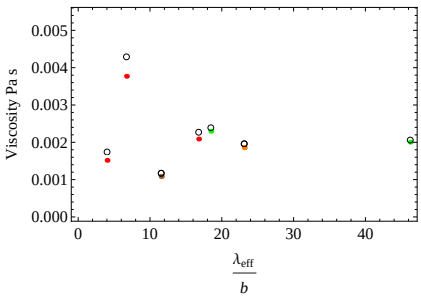

(b) 80:20 % water:ethanol solution.

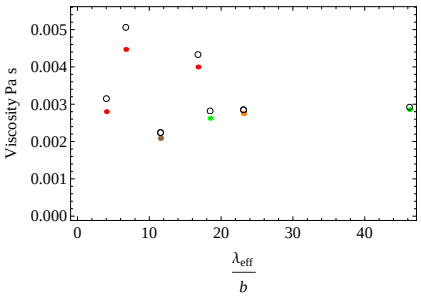

(c) 60:40 % water:ethanol solution.

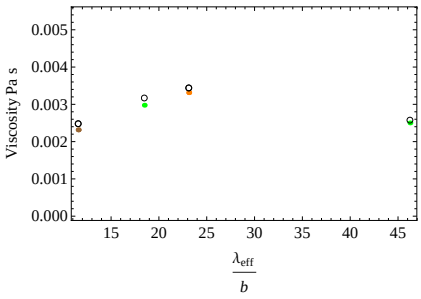

(d) 50:50 % water:ethanol solution.

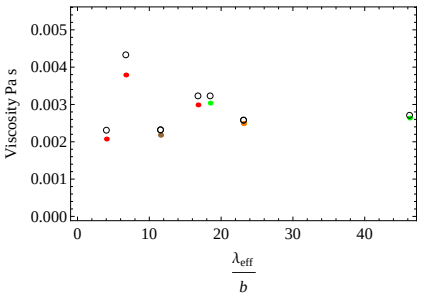

(e) 40:60 % water:ethanol solution.

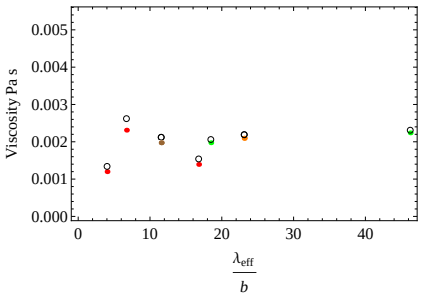

(f) 20:80 % water:ethanol solution.

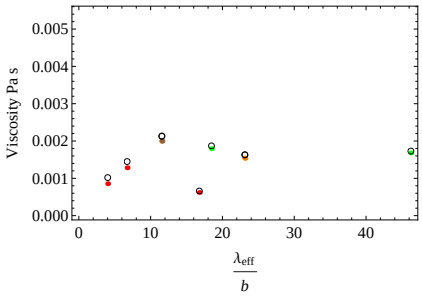

(g) Pure ethanol.

Figure 9.3.2: Comparison between viscosities calculated using the model outlined in section (9.1.5) (empty circles) and the approximated values (solid discs). Values shown for the Array cantilever (red), the Long Veeco cantilever (green), the Medium Veeco cantilever (orange) and the Small Veeco cantilever (brown).

9.4 Conclusions

This chapter explored the ability of two models for the viscous flow around a cantilever to account, separately, for the density and viscosity of water-ethanol solutions of different strengths, and the difference in quantitative accuracy between the two of them. Although the data set is not as large as it could be, it can be clearly seen that not accounting for mode number in the model has an adverse effect on the results. Perhaps more important, since many measurements are made using only the first mode of vibration, the aspect ratio of the cantilever is shown to be of paramount importance in gaining a valid measurement.

I have discussed the breakdown of the model's applicability with effective wavelength, which covers arguments around both mode number and aspect ratio. Although the experimental data included in this report is not sufficient to formulate a detailed breakdown model, it is possible to show the trend for the accuracy of the hydrodynamic function with decreasing aspect ratio.

I have begun a preliminary investigation of ways to computationally simplify the calculation process to better correspond to in-situ timescales for the turn-around between measurement and result, while maintaining an acceptable level of accuracy. For development into a valid point-of-care method, for potential inclusion in hand-held biochip devices, the computational time and power needed must be kept at a minimum. Calculations with the full Model 2 that range in CPU time from 27 seconds to over 20 minutes are calculated to within 5% for density and 10% for viscosity in times of 0.1-0.5 seconds. The model of approximating is not analytical and can thus only be applied for a pre-defined range of density and viscosity, but for most applications it is safe to assume that some prior knowledge of the approximate value range will exist. For these calculations the data set used to interpolate the final results was for a Reynold's number from 10^{-4} to 10^{4} and a κ from 0 to 20.

This chapter looks at the manner in which frequency shifts can be used to determine density and viscosity of the operating medium, and has led to a publication on the determination of alcohol content in commercial beverages [215].

But findings in this vein can also be reversed to develop models to explain how density and viscosity impact upon the resonant frequency and how these effects can be deconvoluted and accounted for, for measurements taken in complex media.

This is particularly important for biosensing, where many analytes would not survive, or be altered by, ex-situ measurements. For example, measurements for medical purposes may often have to be made in plasma, blood, urine or other non-ideal bodily fluids.

Chapter 10

Conclusions and future work

10.1 On the origins of surface stress

In chapter (5) I presented analytic expressions for the various force contributions to a cantilever-adsorbate system in equilibrium, to try to elucidate which factors cause the change in surface stress that leads to deflection of the beam. I also developed a lattice model in Mathematica 8.0 [25] capable of reproducing the spacing and coordination of adsorbates on cantilever's surface, and of calculating the radius of curvature induced by a particular set of forces and thus the deflection response of a cantilever to a specific adsorbate.

In applying these models to a cantilever covered with a full monolayer of decanethiol molecules, I demonstrated that many of the stress values for formation of such a monolayer reported in the literature [56, 107, 108] can be accounted for by the repulsive interactions at the cantilever's surface due to the dipoles that sit at the point where the S head atoms covalently bond with the Au surface atoms, which yields a compressive surface stress of ~ -0.14 Nm^{-1}.

Where experimental investigations report stress values that exceed this amount, I have suggested a mechanism by which the excess can be accounted for; through relief of the intrinsic tensile stress observable on clean metal surfaces. This tensile stress has been measured and calculated as being of the order of 1 Nm^{-1} in

total magnitude, so a release of part of this, due to the presence of adsorbates on the surface and the reorganisation of charge that this instigates, is one likely origin of the increased stress shown for alkanethiol monolayers elsewhere in the literature [100, 106].

This chapter begins to highlight the complexity of interaction involved in measurements with this technology and the need to carefully monitor or control all aspects of the system, including the state of the underlying Au surface, in order to maintain a satisfactory degree of reproducibility and comparability between measurements. The large stress response measured by Godin et al [106], of -15.9 Nm^{-1} suggests that there are further factors at work in the cantilever-monolayer system.

Future work

Considering how important rearrangement of charge at the surface upon adsorption is to the observed surface stress, further investigation of the preferred adsorption sites for S on an Au(111) surface is definitely warranted. For example, in terms of how the length of the chains of C atoms of alkanethiols affects the situation of the covalent bond. Some studies [56] report distinct differences in σ for varying chain lengths. Since we assume, for simple alkanethiols, that the chain-chain interaction is purely affecting the tilt angle of the adsorbed molecules then why would this effect manifest? It is suggested that these findings are the result of how the movement of charge, transferred across the covalent S-Au bond, up the C chain differs depending upon its length. However, it would also be worth running lattice model calculations for the different S-S separations and orientations postulated in those papers devoted to understanding how the $(\sqrt{3} \times \sqrt{3})R30^\circ$ lattice and the c(4×2) superlattice differ in positioning of the head groups on the surface, particularly since the prevalence of each is dependent to an extent on chain length of the alkanethiols.

As well as gaining a deep understanding of the sources of surface stress for this particular system, this work should be driven towards gathering enough knowledge to be able to draw wider conclusions about the stress generation for

any system, so general or initial predictions as to expected stress responses can be made without resorting to expensive and time-consuming simulation and experimental exploration techniques. This pool of understanding, which is only shallow at the current time, can be deepened through detailed investigation into other adsorbate systems. Members of our group at the LCN have already made some preliminary experimental investigations into the surface stresses of formation of monolayers of D-Ala and PEG molecules. Building models to represent these two setups would not only yield valuable information in their own right, but also tie in to the further work planned for the D-Ala-Vancomycin complexes, and discussed in the next sections.

Another system of interest is that mentioned in chapter (8), of the deprotonation of a carboxylic acid terminated monolayer of mercaptoundecanoic acid upon changes in the pH of the operating medium, which shows an increased stress compared to that of a neutral undecanethiol monolayer of -10.75 mNm^{-1}. I have done some preliminary calculations on the response for a full monolayer of MUA, assuming that at pH 9.0 every alkanethiol comprising the monolayer is deprotonated, using the same lattice setup as for the decanethiol monolayer in chapter (5). Due to their extremely similar packing densities and structural make-up, it is likely that the difference in stress response is solely due to the electrostatic repulsion between negatively charged COO^-. The calculation simply equates the sum of the terminal group's repulsive coulombic forces with the elastic restoring force of the beam. However, the value of surface stress calculated is -185.97 mNm^{-1}; an order of magnitude larger than that experimentally measured.

Simply reducing the coverage of 'active' charged sites in the model, to correspond to a more realistic partially incomplete monolayer, is not enough to reflect the reality of the situation however. A model that looks to explain the stress transduction mechanism purely through electrostatic repulsion as above must reduce coverage of charged sites down to $p \approx 0.3$ before the theoretical stress, 18.0 mNm^{-1}, approaches that experimentally observed.

To represent the deprotonation as a point charge on the upper end of each

monolayer molecule is a very crude way of looking at the system. In actuality the negative charge is delocalised between the two oxygen atoms of the carboxylate group, forming two partial double bonds with the intermediate carbon atom, as represented in figure (10.1.1). To achieve a meaningful stress value from the model, this added complexity should be included in the interactions.

But the main discrepancy between this model and the experimental measurements is neglect of the solute properties. There will be a degree of screening due to ions in solution surrounding the cantilever, which will have the effect of reducing the bending due to electrostatic interaction of the deprotonated MUA molecules. Indeed, Watari et al [54] demonstrate that not only the number of ions in solution, but also ionic species can have a profound effect on surface stress in these kinds of systems. This is something that needs including in the model, along with a better representative of the siting of the deprotonation charge, and may account for the differences in experimental and theoretical results.

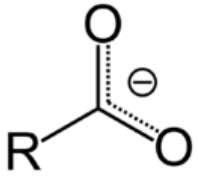

Figure 10.1.1: Schematic representing the delocalised charge on a deprotonated carboxylate group.

10.2 Vancomycin and understanding the effects of connectivity

I extend the lattice model to include coverage dependence, which is demonstrated in chapter (6) in my reproduction of the site percolation thresholds for honeycomb and square lattices of 0.70 and 0.59 respectively. This extended lattice model is then used in conjunction with potentials for Vancomycin interaction, for comparison to the experimental results outlined in chapter (4)

to explore the effects of coverage and connectivity on a cantilever's deflection response.

Through simulation and analysis of the interaction force on approach between two complexes of Vancomycin and the upper fragment of a bacterial cell-wall mucopeptide precursor, I extrapolated a first approximation of the force curve describing their interaction in the form,

$$F(r_{ij}) = 2\epsilon \left(\left(\frac{r_{min}}{r_{ij}^2} \right) - \left(\frac{r_{min}^2}{r_{ij}^3} \right) \right), \tag{10.2.1}$$

where the equilibrium separation is $r_{min} = 14.75$ Å.

Upon application to the lattice model, this very simple approximate fit to the force curve produces stress results that are encouragingly close to those observed experimentally. Fitting the lattice model stress values for different coverages, up to a complete underlying D-Ala monolayer, to the model described by equation (4.1.1), gives a saturation stress of $\sigma = -110.06$ mNm^{-1} which is within an order of magnitude of the experimental -34.6 ± 0.9 mNm^{-1} [15], and a percolation threshold and power law index that fall within the experimental error bars, of $p_c = 0.003$ to 0.075 ± 0.09 and $\alpha = 1.15$ to 1.3 ± 0.3 respectively.

Future work

The validity of results from MD simulation relies heavily on the accuracy of the model potentials and parameters used to describe the system under scrutiny. As mentioned in chapter (7), some of the parameters used in this body of work are approximated from similar systems rather than specifically tailored to the chemistry of Vancomycin. Before continuing to explore Van, in such a way, in more detail, more accurate and appropriate parameters (partial charges; bond lengths, angles and force constants) should be developed, using the methods outlined in [95].

The results of chapter (7), interpreted as I have done here, only really take into account one local minimum of the interaction between two Van-D-Ala complexes. Starting configurations in simulations has a lot to do with what energetic

landscape is explored. A systematic study of the possible approach configurations of a pair of complexes may uncover preferable local minima, or the global minimum of interaction. Of particular interest is how a pair interact in their back-to-back arrangement, since the varying likelihood of dimerisation, particularly when catalysed at a surface, across the Vancomycin family of antibiotics may have a considerable part to play in enhancing their antibiotic action. With a much higher ability to dimerise, Oritavancin shows a binding relationship with D-Ala precursors 25 times stronger than that for Vancomycin, and 11,000 times stronger with the Vancomycin-resistant mucopeptide terminating in D-Lactate [21]. Ndieyira et al. show that Oritavancin is predominantly bound to the surface in dimer complexes, as opposed to the dominance of bound monomers for Vancomycin, and suggests that this altered form of antibiotic-mucopeptide complex may be, in part, responsible for their contrasting antibiotic action: Vancomycin takes $\sim$24 hours to kill a bacterial cell, Oritavancin only two.

While the simulations that comprise much of chapter (7) have provided an interesting and fruitful first insight into the interaction of Vancomycin molecules bound to a monolayer of D-Ala mucopeptide precursor analogues, the next step must be to increase the complexity of the computational model to better represent the actual cantilever system.

Acknowledgement of the role screening due to ions in the buffer surrounding the cantilever has to play in the interactions leading to a deflection response cannot be ignored in a system such as this, where the analytes are charged. The simplest way to gain a lower limit on the interaction due to charges, where an upper limit is a simulation in vacuum, is to calculate the interactions for complexes in an environment with the dielectric constant of the buffer solution in which they are immersed, which I have calculated to be approximately $\epsilon = 79.6$, close to that of water. This approach, however, shows no appreciation of the size and behaviour of individual water molecules and ions, and as such is inferior to the explicitly hydrated simulations that would be the eventual aim.

A big step in improving the validity of simulations of this kind for Vancomycin would be to include the rest of the monolayer, assuming as I am that it

has a large part to play in both the way Vancomycin behaves when bound and in the transduction of the surface stress. One of the major assumptions of chapter (7) was that the D-Ala monolayer was organised similarly to an alkanethiol monolayer, as a hexagonally close-packed lattice. Considering the bulky nature of the mucopeptide analogue, this is not a certainty. The first undertaking in attempting to include the monolayer in simulations is to systematically investigate the structure and coordination most energetically favourable for such an organisation of molecules. For example, a starting configuration for a preliminary simulation of D-Ala molecules in an hexagonal lattice at a separation of ~ 8 Å is shown from above and side on in figure (10.2.1).

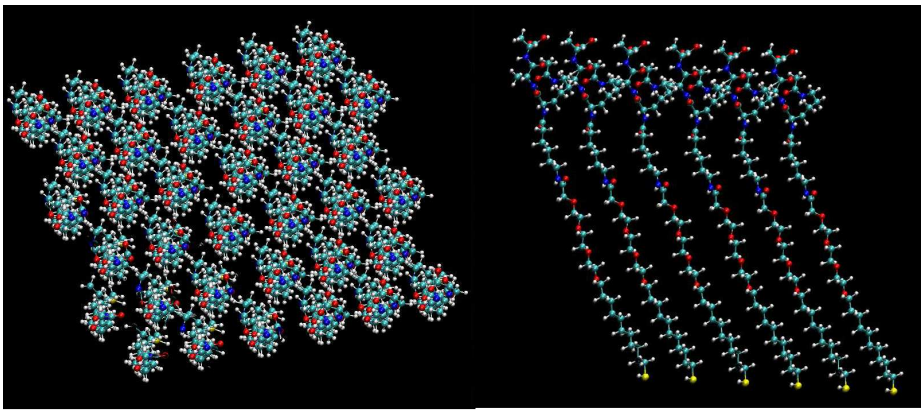

Figure 10.2.1: D-Ala molecules organised into an hexagonally close-packed lattice at a separation of ~ 8 Å. Image created using VMD [216].

Once the nature of the underlying monolayer is better understood, antibiotics can be added to the simulation cell. There is merit in uncovering how the energy of the monolayer changes both from the interaction of the added antibiotic molecules, and also from observing how inserting a single Vancomycin molecule into the D-Ala layer exerts forces on those proximal precursor analogues and how those forces are mediated through the monolayer as a whole. This work would raise interesting questions around the necessity of viewing a monolayer both as the sum of individual members and as a whole, and the

subsequent need to include short and longer-ranged stress dependencies in a theoretical model. More detailed simulation of Vancomycin can also be quite easily extended to other antibiotics in the same family [5] by addition of, correctly parameterised, specific chemical groups along the molecule's backbone.

Experimental findings that drive the next steps of research into the part that the monolayer plays in the Van-D-Ala-cantilever system result from continuing investigations made into the effect of the underlying density of D-Ala SAMs on the stress response by M. Vogtli, who measured the stress response of cantilevers functionalised by varying concentrations of 10^{-4}, 10^{-3},
0.01, 0.05, 0.1, 0.5, 1.0, 2.0, 3.0, 4.0mM of D-Ala in solution, upon exposure to Vancomycin.

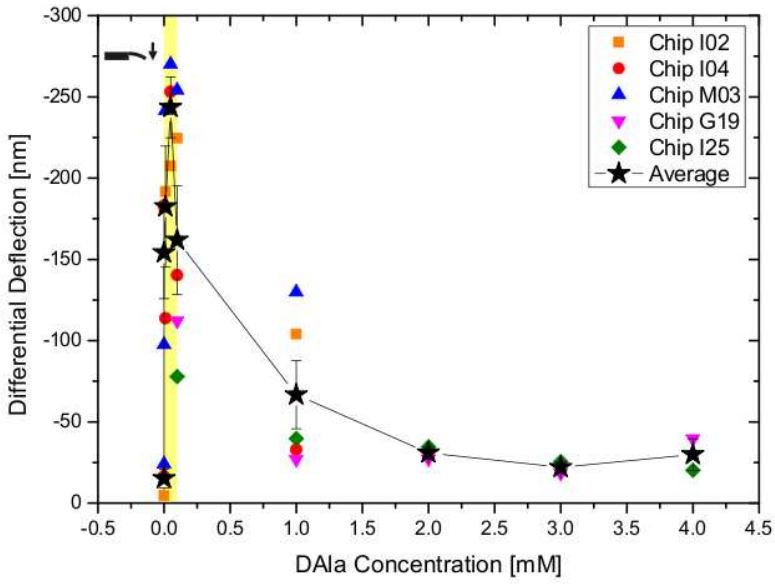

Figure 10.2.2: Measured cantilever deflection due to compressive surface stress for differently functionalised monolayers of D-Ala upon injection of 250 μM Vancomycin. Reproduced courtesy of M. Vogtli.

There was a very minimal stress response measured for the lowest concentrations of D-Ala, combined with ellipsometry measurements showing a layer

thickness of 5 Å, contact angle results similar to that of bare Au, low N(1s) and S(2p) XPS intensities and high Au(4f) intensity. All of the above results suggest an incomplete covering of D-Ala molecules in the lying down stage.

Above a concentration of 0.05 mM, where the stress peaks, the data supports a monolayer in the standing regime with a thickness, according to ellipsometry data, of $\approx$ 30 Å. As the concentration increases beyond this point the ellipsometry thickness holds approximately constant at $\approx$ 30 Å, but the XPS S(2p) intensity continues to increase suggesting that the coverage remains that of a single monolayer but one that is increasing in density, and the measured deflection, and thus the stress, drops, as can be seen in figure (10.2.2).

The fall off in stress as the monolayer gets denser could be the result of several factors; that as the monolayer becomes much more densely packed less binding sites are available to the antibiotics, or that at higher concentrations the monolayer of D-Ala that is forming is much more disordered.

Or the pronounced peak in stress may be a consequence of the shape of the interaction curve between two approaching Van-D-Ala complexes. It is a possibility that the drop in repulsion between two approaching complexes, as seen in figure (7.1.2) and temporarily neglected to formulate a first approximation of the interaction, may be an exaggerated version of what is actually happening on a cantilever surface. If the individual D-Ala molecules in the monolayer are tighter packed, at a smaller separation, then the proximity of the bound Vancomycin may result in an interaction energy high enough to release them from the local minimum they found at slightly larger separations. Though such a dramatic configurational shift as that witnessed in the simulations in chapter (7), at such large separations, may be unlikely due to the surrounding monolayer and other bound Vancomycin adding to the energy barrier to large-scale conformational shifts, something in the same vein may be taking place at separations consistent with the densities at which σ values drop. Or, indeed, the increased steric interactions at these smaller separations may make it energetically unfavourable for Van molecules to bind to adjacent D-Ala sites. If the model in chapter (7) is

representative this proximity is necessary for generation of the stress signal and a cantilever with fewer sites with nearest neighbour connectivity will return a lower deflection signal.

Whatever the reason for these changes in stress, it is clear that the state of the underlying monolayer plays an important role in the response measured. In order to explore the nature of this role I intend to perform molecular dynamics simulations of D-Ala monolayers of varying density to see how the configuration and the energy changes.

10.3 Modelling the beam's elastic response

In chapter (8) I derived analytical expressions for the sensitivity of a cantilever beam undergoing pure bending to surface stress, σ, based on its geometry and materials. I have shown, quantitatively, the potential in novel cantilever materials, such as polymers and carbon nanotubes, for future incorporation into cantilever technology.

I made investigation into simple theoretical models of how changing the patterning of the active layer on the surface can affect a cantilever's performance. It is demonstrated that changing the longitudinal length of patterning along a cantilever, and the positioning of this strip on the cantilever can have a significant effect. A cantilever with half its upper surface covered in Au can increase its σ response by up to three times, simply by coating that half from the hinge end rather than the free end of the cantilever. The theoretical model here shows similar qualitative behaviour to those experimental results reported alongside it. However, in failing to supply a fully comprehensive reason for the lack of observed signal up to 70% coverage of active layer, as coated from the free end, in experiment, this work suggests that other factors, not yet well understood, are causing big differences in stress that may be due to the quality of the monolayers produced by patterning the active layer using μCP.

Also within this chapter, I explored the suggestion, proposed in line with experimental findings, that tangential curvature of the beam stiffens it to lon-

gitudinal stresses. This changes the way we might assume that surface stress would decrease on reducing the area of the Au active strip by narrowing it widthwise. The simplified model contained herein supports the merit of the argument, showing a difference in stress brought on by halving the width of the active strip of 50% when only longitudinal curvature is considered, compared with 33% when the stiffening effects of tangential curvature are also included.

Future work

The investigations into the bending behaviour of the cantilever beam made in this thesis have necessarily been simplified to enable the formulation of analytic expressions that underline what merit there is in further examination of the various factors that might complicate stress results.

For many of these factors, approaching a state that accurately represents reality is beyond the capability of pen and paper analytic derivation. To consider how the bending response is altered by the combined effects of biaxial bending, active layer patterning, differing materials and adhesion layers and its tethering at the hinge end, it will be more useful to employ numerical techniques such as finite element analysis [217, 218].

10.4 Exploring the effect of the medium

For a cantilever beam of aspect ratio ~ 13, values of density obtained from the dynamic mode of operation for ethanol/water solutions of 0, 20, 40, 50, 60, 80 and 100 % ethanol are within $\sim 5\%$ of those recorded in the CRC handbook of chemistry and physics [219]. Those values calculated for viscosity are not as accurate but still predominantly fall within $\sim 25\%$ of the literature values. I believe the discrepancies here may be due to the viscosity of the solution not exactly mirroring that of the ideal literature values.

Utilising a model that included a specific dependence on mode number was shown to correct, to an extent, for the overestimation of hydrodynamic load in a model with no such dependence. However, for cantilevers with lower aspect

ratios (~ 6.6, ~ 5, ~ 3.3), even this more advanced model was shown to break down as the real life situation deviated significantly from the model approximation to an infinitely long beam. While the number and reproducibility of the measurements used in chapter (9) are not enough to formulate a detailed breakdown model, a definite trend is clearly demonstrated.

Finally, the validity of an iterative process of correction, from look up tables for the hydrodynamic function for a range of Reynold's number and aspect ratio, between the less accurate 2-D model and its more accurate 3-D successor shows excellent agreement with the 3-D model. This correction process also takes much less computational power and time, two factors of great importance for the technology's future use at point-of-care.

Future work

Most real-world applications for cantilevers in their dynamic mode, for example monitoring blood clotting or taking added mass measurements to assay the amount of different biological analytes in complex fluids, will operate within a reasonably defined range of viscosity and density. It, therefore, makes a lot of sense to use the simpler model to calculate initial values and correction tables to account for the model's shortcomings and extrapolate a more accurate value. If the range is not massive then the amount of information needed to be stored will be manageable for a small hand-held device. The simpler model is less computationally taxing and much less time-consuming, allowing for in-situ measurement and analysis without bulky and immovable external equipment. In order to achieve a reliable model for when the methods of calculation break down, many more measurements should be taken, systematically spanning a wide range of aspect ratios and rheological properties and exploring higher modes. All care must be taken also to ensure that variation between those measurements used to calibrate the tables of correction values is minimised. For example, in the case of these investigations into ethanol/water solutions, it would be valuable to take alongside measurements using a different system, such as glass capillary tubes [220], to get in-situ values for each solution, rather than assuming they

exactly match literature values.

In many aspects nanocantilever technology shows great potential for miniaturisation and incorporation into hand held LOAC devices. The cantilevers themselves operate purely mechanically and, in array, can provide their own reference and control against environmental variables such as temperature changes. Microfluidics [221] enable the delivery of analytes in a controlled way, allowing many simultaneous measurements to be made, even at such a small scale. Holding the technology back at the moment is the technique used to measure deflection. The optical method (see appendix (A)) currently requires a bulky external setup and also suffers from the inability to operate through opaque fluids. Other measurement techniques such as incorporation of a piezoelectric strip in the cantilever [222, 223], or the use of parallel, capacitive plates [224, 225], must continue to be investigated as viable alternatives.

This thesis makes progress towards understanding nanocantilever sensor technology as a whole system, by looking at the bending behaviour of the beam, environmental concerns, the chemical origin of stress at the level of a single adsorbate molecule and the effect of geometric connectivity of events across the cantilever's surface in producing the continuum response.

In representing so complex a system as Vancomycin binding to bacterial cell wall analogues on a cantilever's surface, many assumptions and approximations had to be made. The final correlation between the calculated results and those collected experimentally, however, presents a good example of the power of simplified models to elucidate the figures of merit for understanding elaborate real-world scenarios.

This thesis provides a first step in the development of a truly comprehensive theoretical model supporting nanocantilevers as a reliable and accurate technology for biosensing. In particular it highlights how interdisciplinary working can open up new avenues of approach for pressing problems, like how better understanding of drug action can impact the development of new antibiotic

agents.

Appendix A

Sensor measurement techniques

A.1 Optics

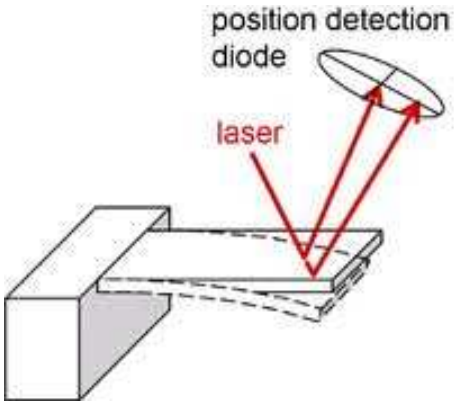

Figure A.1.1: Figure outlining the optical lever measurement setup.

Used commonly in conjunction with AFM as well as being the most widespread detection method for stand-alone cantilever devices, the optical lever method uses a position sensitive photodetector to measure the displacement of reflected

laser light from a cantilever [226]. This setup can be seen in figure (A.1.1) and can record the absolute deflection of a beam down to sub-angstrom resolution. The segmentation of the photodiode allows for the potential to measure in-plane and out-of-plane lateral and torsional oscillations simultaneously.

Drawbacks to this setup include the need for external devices and time consuming and fiddly calibration and alignment, making it a less than perfect candidate for incorporation into LOAC devices. Optical detection is also very sensitive to changes in the optical properties of the medium surrounding a cantilever. As such, changes in optical density can move the laser spot along the cantilever; particulates within the operating fluid can scatter the laser light; and a non-transparent medium renders the method untenable [174].

The method relies on either an array of lasers, which can be difficult to set up, or a scanning laser source that moves sequentially across the end of each of the cantilevers comprising an array [227], and as such needs a reflective surface of a certain size. The thermal effects of laser light on a cantilever in the micro-scale can lead to bimetallic bending or thermal expansion, giving rise to significant thermal drift, which must be accounted for, generally using reference cantilevers.

Modifications to optical detection can alleviate some of these causes of concern. Interferometry, in which the reflected light is modulated by the changing separation between cantilever and detector, need only illuminate a small part of the cantilever and can be used to detect the resonant behaviour of devices significantly smaller than the wavelength of light [228]. Optical waveguides can be patterned into cantilevers and aligned with another, static, section of waveguide separated from the cantilever by a small gap. When oscillations occur, the amount of light able to pass through the static section of the waveguide will modulate; an effect that can be measured and related to resonant frequency [229].

A.2 Electrics

Cantilevers incorporating piezoelectric or piezoresistive material are causing a lot of interest in the biosensor community as they can act both as sensor and measurement method, eliminating the need for external laser alignment [84, 223, 230, 222]. Piezoresistive material experiences a change in resistivity upon compression or extension of the material and similar distortions due to mechanical stress creates a voltage across piezoelectric the material. When piezoresistive or -electric material is included in a nanocantilever, the bending due to adsorbate induced surface stress can be indirectly measured by monitoring the changes in resistivity or voltage.

This technology is attractive to the biosensing community because it doesn't need a transparent medium, and, acting as its own readout mechanism, is suitable for integration into LOAC devices [189, 84].

There are associated difficulties around ensuring that the electrically responsive parts of the setup are protected from contact with the liquid media. There is also some challenge in reaching the levels of sensitivity seen with optically readout cantilevers, as the thickness of the piezo-films must be relatively substantial in order to gain a decent signal [231]. Techniques to maximise the sensitivity are being developed however [232], and the technology has real potential for use in the miniaturisation of the entire process of actuation and measurement.

It is also possible to include a layer of conductive material on a cantilever's surface and then measure the capacitance between said conductor and a corresponding one on a substrate at some distance [233]. Any change in distance between the two conducting strips will register as a change in capacitance. The capacitance will vary inversely proportionally with distance and this value and its period of oscillation directly informs one of changes in amplitude and frequency of the cantilever.

This method has been found to be capable of detecting the addition of toluene at 50 ppm and octane at 10 ppm [224] and is suitable for LOAC integration, but it suffers both from interference due to changes in the dielectric

constant of the operating medium, and is limitingly dependent on the gap between the cantilever and the substrate.

Appendix B

Vacuum frequencies of an oscillating cantilever

We can find the resonance frequencies of a singly clamped beam, a cantilever, in a vacuum by first looking at the equations of equilibrium for a bent beam. We need to satisfy the requirements of equilibrium; namely that the resultant forces and the resultant moments across the beam are zero. Looking first at the forces, we can denote the resultant internal stresses on a cross-section of the beam as $\mathbf{F}$ with components $F_i = \int \sigma_{i\zeta} df$ that are integrated over the area of the cross-section. Using this notation we can look at two adjacent cross-sections that bound a chosen element of the beam, which will be experiencing internal forces $\mathbf{F} + d\mathbf{F}$ and $-\mathbf{F}$, the resultant of which is $d\mathbf{F}$. The beam will also be experiencing an external force per unit length, $\mathbf{K}$, which, across an element dl in length, will be $\mathbf{K}dl$. At equilibrium then, the total forces on the element will be:

$$\frac{d\mathbf{F}}{dl} = -\mathbf{K} \tag{B.0.1}$$

The moment of the internal stresses on a cross-section has a component about each co-ordinate axis (chosen as arbitrary axes for now):

$$\mathbf{M} = \begin{pmatrix} M_\xi \\ M_\eta \\ M_\zeta \end{pmatrix} = \begin{pmatrix} EI_1\Omega_\xi \\ EI_2\Omega_\eta \\ C\Omega_\zeta \end{pmatrix} \tag{B.0.2}$$

where E is the Young's modulus of the beam, I_1 and I_2 are the principal moments of inertia, C is the torsional rigidity and Ω_i is the rate of rotation of the co-ordinate axes about the ith axis. Across the aforementioned element, at one end we have moments $\mathbf{M}+d\mathbf{M}$ about a point O on the cross-section, and at the other end moment of internal stresses $-\mathbf{M}$ about the 'shifted' point O' plus the moment of the force on that end about the initial point O, $d\mathbf{l}\mathbf{x}\mathbf{F}$, where $d\mathbf{l}$ is the vector of the length between the points O and O'. As we are considering our beam to be thin, the moment due to external forces is of a higher order of smallness (it takes relatively small external forces to produce large internal stresses in a thin rod - i.e. it is very easy to bend a thin beam) and can therefore be neglected. So, in equilibrium:

$$d\mathbf{M} + d\mathbf{l}\times\mathbf{F} = 0 \tag{B.0.3}$$

If we divide this through by dl we get the expression:

$$\frac{d\mathbf{M}}{dl} = \mathbf{F}\times\mathbf{t} \tag{B.0.4}$$

where $\mathbf{t}$ is the unit vector tangential to the beam, which for our purposes we are approximating as an elastic line. Differentiating with respect to the length gives:

$$\frac{d^2\mathbf{M}}{dl^2} = \frac{d\mathbf{F}}{dl}\times\mathbf{t} + \mathbf{F}\frac{d\mathbf{t}}{dl} \tag{B.0.5}$$

the last term of which can be neglected as in the case of very small deflections the direction in which the tangential vector points changes slowly along the length of the beam. From the first requirement of equilibrium above, we see that we can substitute $\frac{d\mathbf{F}}{dl} = -\mathbf{K}$ into this expression, giving us the equation of

equilibrium of a beam experiencing small deflections in the form:

$$\frac{d^2\mathbf{M}}{dl^2} = \mathbf{t}\times\mathbf{K} \tag{B.0.6}$$

where the components of $\mathbf{M}$ are as stated before. In the case of slight bending we can assume zero torsion in the beam, i.e. $\Omega_\zeta = 0$ By taking the definition of $\Omega = \frac{d\phi}{dl}$, which is the rate at which the vector of angle of rotation of the co-ordinate axes changes along the length of the beam, and realising that the change in a vector due to an infinitesimal rotation is the vector product of said vector and the rotation vector $d\phi$, which for the tangential vector gives us:

$$d\mathbf{t} = d\phi\times\mathbf{t} \tag{B.0.7}$$

or in terms of Ω:

$$\frac{d\mathbf{t}}{dl} = \mathbf{\Omega}\times\mathbf{t} \tag{B.0.8}$$

which, when multiplied through vectorially by $\mathbf{t}$, is

$$\mathbf{\Omega} = \mathbf{t}\times\frac{d\mathbf{t}}{dl} + \mathbf{t}(\mathbf{t}.\mathbf{\Omega}) \tag{B.0.9}$$

By recognising that, as the tangential vector is in the same direction as the axis of the elastic line at any point,and therefore $\mathbf{t}.\mathbf{\Omega} = \Omega_{zeta}$,and remembering we are assuming zero torsion, we get an expression for $\mathbf{\Omega}$:

$$\mathbf{\Omega} = \mathbf{t}\times\frac{d\mathbf{t}}{dl} \tag{B.0.10}$$

Using this expression and due to the smallness of the deformations involved we can now approximate rotations of our arbitrary co-ordinate axes to the fixed axes x, y and z, where z runs along the undeformed axis of the beam. We can approximate the unit tangent vector to the unit vector along the z-axis and the change in that unit tangent vector along the length of the beam as the second derivative of the radius vector $\mathbf{r}$ of the curve with respect to its z position. This

allows us to write the two non-zero components of the rotation $\mathbf{\Omega}$ as:

$$\Omega_{xi} = -\frac{d^2Y}{dz^2} \tag{B.0.11}$$

$$\Omega_{eta} = \frac{d^2X}{dz^2} \tag{B.0.12}$$

where X and Y are coordinates giving the displacements of points from their initial positions in the undeformed beam. Which gives us expressions for the non-zero components of the moment $\mathbf{M}$ as

$$M_x = -EI_xY'' \tag{B.0.13}$$

$$M_y = EI_yX'' \tag{B.0.14}$$

where having defined our fixed axes as x, y and z, in a beam with constant, rectangular cross-section, the principal axes of inertia are parallel to the sides. These definitions, when substituted into equation (B.0.6) give us the expressions:

$$EI_yX'''' = \rho A\ddot{X} \tag{B.0.15}$$

$$EI_xY'''' = \rho A\ddot{Y} \tag{B.0.16}$$

Where in the case of a thin beam performing transverse oscillations, the components of external force per unit length can be replaced by the acceleration, $\ddot{X}$ and $\ddot{Y}$, that must depend on both t and z, and the mass per unit length of the beam, ρA, where ρ is density and a the cross-sectional area of the beam. If we are considering a beam oscillating in the x-z plane we can then seek solutions to equation B.0.15 using the ansatz $X = X_0(z)\cos(\omega t + \alpha)$ and the following boundary conditions for a cantilever beam:

$$fixed\ end: \ z = 0;\ X = 0;\ X' = 0 \tag{B.0.17}$$

$$free\ end: \ z = L\ X'' = 0;\ X''' = 0 \tag{B.0.18}$$

$$\dot{X} = -X_0\omega\sin(\omega t+\alpha);\ \ddot{X} = -X_0\omega^2\cos(\omega t+\alpha) \tag{B.0.19}$$

$$X'''' = X_0''''\cos(\omega t+\alpha) \tag{B.0.20}$$

$$X_0'''' = \frac{\omega^2\rho S}{EI_y}X_0, \tag{B.0.21}$$

where we will define the coefficient as $C_n^4 = \omega^2\frac{\rho S}{EI_y}$. The most general form of X_0 will be a combination like:

$$X_0 = A\cos(C_nz) + B\sin(C_nz) + D\cosh(C_nz) + E\sinh(C_nz) \tag{B.0.22}$$

Applying the boundary conditions for the fixed end of the beam, we can see that $D = -A$ and $E = -B$, so

$$X_0 = A[\cos(C_nz) - \cosh(C_nz)] + B[\sin(C_nz) - \sinh(C_nz)]. \tag{B.0.23}$$

Applying the boundary conditions for the free end to this new expression for X_0 gives,

$$X_0''|_{z=L} = A[-\cos(C_nL) - \cosh(C_nL)] + B[-\sin(C_nL) - \sinh(C_nL)] = 0 \tag{B.0.24}$$

and

$$X_0'''|_{z=L} = A[\sin(C_nL) - \sinh(C_nL)] + B[-\cos(C_nL) - \cosh(C_nL)] = 0. \tag{B.0.25}$$

These two expression can be combined to find a relationship between the

coefficients A and B, such that

$$B = A\left(\frac{-\cos(C_nL) - \cosh(C_nL)}{\sin(C_nL) + \sinh(C_nL)}\right). \tag{B.0.26}$$

Substituting this back into the expression for $X_0'''|_{z=L}$,and using the identities $\sin^2(C_nL)+\cos^2(C_nL) = 1$ and $\cosh^2(C_nL) = \sinh^2(C_nL) = \frac{1}{2}(\cosh(2C_nL)+1)$, gives

$$A(1 + \cos(C_nL)\cosh(C_nL)) = 0, \tag{B.0.27}$$

which we can solve to find the values of C_nL. If we take the length of the beam as being normalised to $L = 1$, the coefficients of the first four modes are $C_1 = 1.875$,$C_2 = 4.694$,$C_3 = 7.855$ and $C_4 = 10.996$ and can be applied to find the vacuum frequencies of an oscillating beam using

$$\omega = \frac{C_n^2}{L^2}\sqrt{\frac{EI_y}{\mu}} \tag{B.0.28}$$

where I have rewritten $\mu = \rho A$ for the mass per unit length of the beam. In order to find the above solution, we set the external force on the beam equal to zero. For a beam oscillating in a medium, however, will experience a hydrodynamic load that will depend on the nature of the oscillations and the rheological properties of the medium.

Appendix C

Adsorption sites

In this appendix, I list those arrangements of S atoms commensurate with the underlying Au surface structure in a separation range of 6 to 8 Å, calculated as detailed in section (7.7). The available separations are listed in ascending order, with indication of whether they are suitable for forming a hexagonal close-packed lattice.

6.04 Å

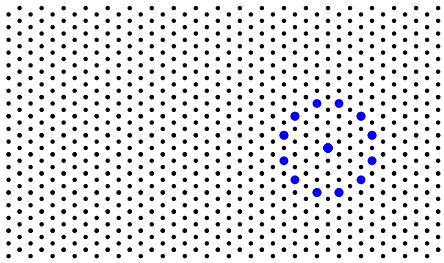

Figure C.0.1: Separation of 6.04 Å: hexagonal lattice.

6.32 Å

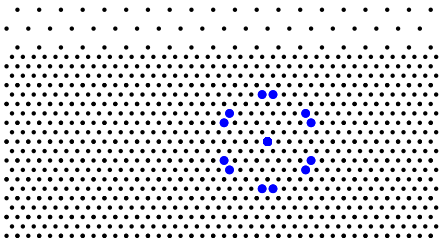

Figure C.0.2: Separation of 6.32 Å: hexagonal lattice.

6.54 Å

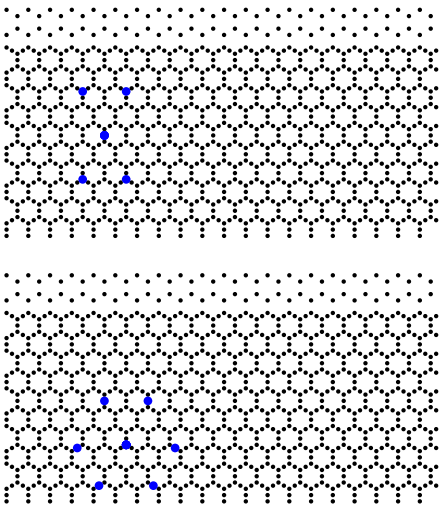

(b) Separation of 7.3 Å

Figure C.0.3: Separations of 6.54 Å: no hexagonal lattice.

6.64 Å

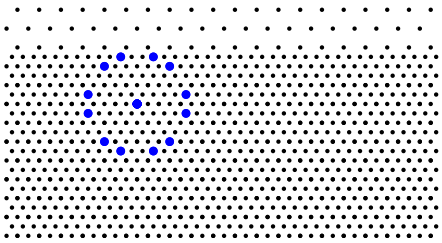

Figure C.0.4: Separation of 6.64 Å: hexagonal lattice.

6.70 Å

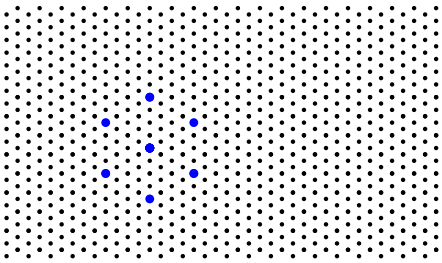

Figure C.0.5: Separation of 6.70 Å: hexagonal lattice.

6.85 Å

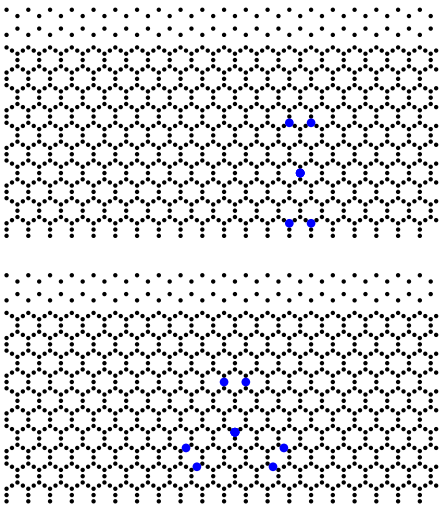

Figure C.0.6: Separations of 6.85 Å: no hexagonal lattice.

7.15 Å

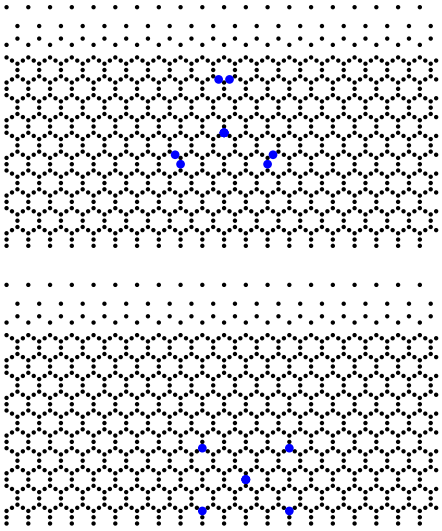

Figure C.0.7: Separations of 7.15 Å: no hexagonal lattice.

7.25 Å

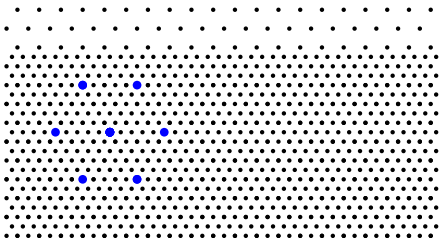

Figure C.0.8: Separation of 7.25 Å: hexagonal lattice.

7.30 Å

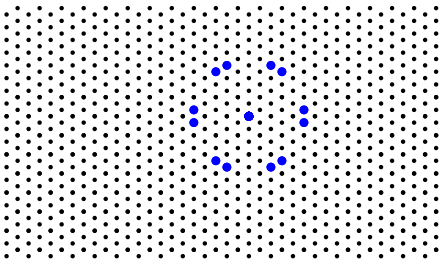

Figure C.0.9: Separation of 7.30 Å: hexagonal lattice.

7.44 Å

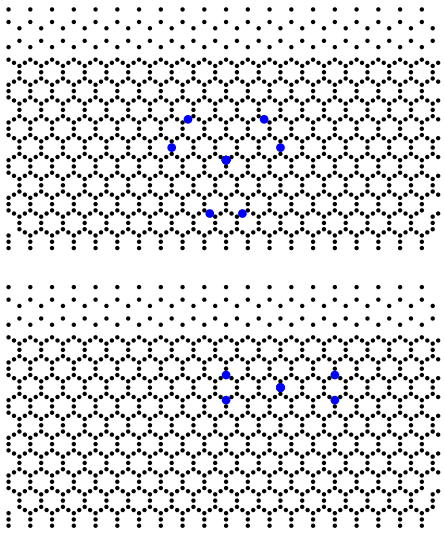

Figure C.0.10: Separations of 7.44 Å: no hexagonal lattice.

7.53 Å

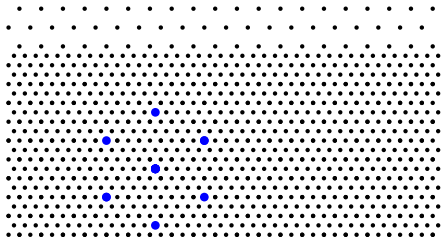

Figure C.0.11: Separation of 7.53 Å: hexagonal lattice.

7.67 Å

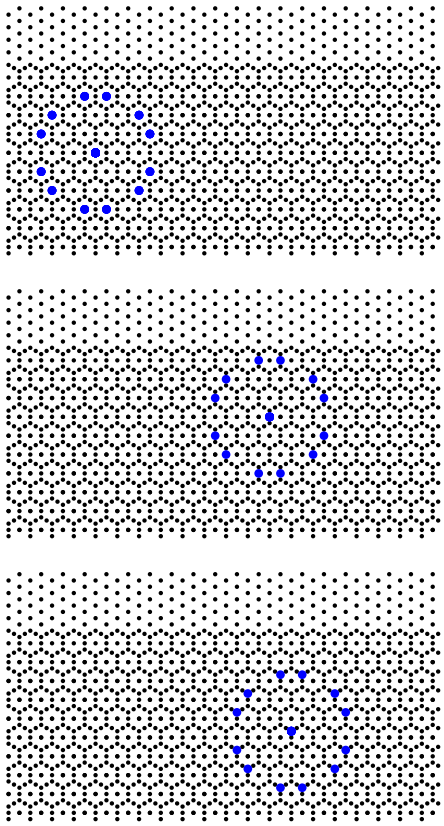

Figure C.0.12: Separations of 7.67 Å: no hexagonal lattice.

7.99 Å

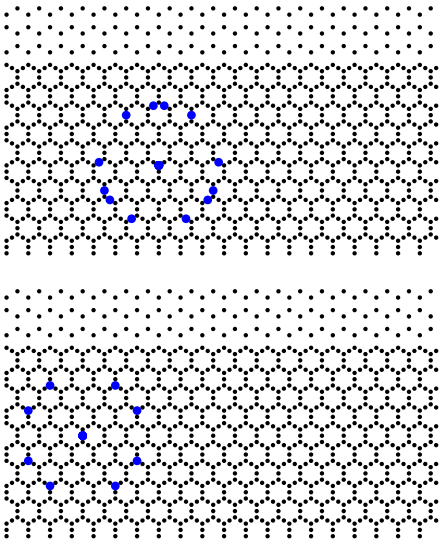

Figure C.0.13: Separations of 7.99 Å: no hexagonal lattice.

Appendix D

Potential parameter approximations

Tables documenting those approximations made for linkages in the Vancomycin-peptide fragment complex that are not already explicitly parameterised in the literature.

For angles described as $U_{angle}(\theta_{ijk}) = \frac{1}{2}k(\theta_{ijk} - \theta_0)^2$, where k is the force constant and θ_0 the equilibrium angle, in degrees.

And for dihedrals described as $U_{dihedral}(\phi_{ijkl}) = A[1 + cos(m\phi_{ijkl} - \delta)]$, where A is the force constant, m the multiplicity and δ the phase, in degrees.

Angle	Sub.	k kcal/mol/rad^2	θ_0 °
CS-CS-CAS3	C1-C1-C3	53.35	108.50
CS-CS5-CAS3	C1-C1-C3	53.35	108.50
HAS1-CS5-CAS3	H1-C1-C3	34.5	110.10
HAS3-CAS3-CS	H1-C3-C1	33.43	110.10
HAS3-CAS3-CS5	H1-C3-C1	33.43	110.10
C1-C1-C4	C2-C1-C4	51.80	107.50
C4-C1-OH	CS-CS-OHS	75.70	110.10
H1-C1-N2	H1-C2-N2	32.40	109.50
C3-N1-C1	C3-N2-C7	50.00	120.00
CS-CS-N3	C_L2-C_L2-N3L	67.70	110.00
CAS3-CS-N3	C_L2-C_L2-N3L	67.70	110.00
CS-N3-HN	C_L2-N3L-HN	33.00	109.50
C4-OET-CS1	C4-OET-C1	65.00	108.00

Table D.0.1: Table listing those approximate angle potential parameters for sections of the Vancomycin-peptide fragment complex that are not explicitly parameterised.

Dihedral	Sub.	A kcal/mol	m	δ °
CAS3-CS-CS-OHS	CAS3-CS5-CS-OHS	0.20	3	0.0
CAS3-CS-CS-HAS1	CAS3-CAS2-CAS2-HAS2	0.19	3	0.0
HAS3-CAS3-CS-CS	HAS3-CAS3-CS5-CS	0.2	3	0.0
OET-C4-C4-OET	OET-C2-C2-OET	0.25	1	180.0
		1.21	2	0.0
OET-C4-C4-CL	OET-C4-C4-C3	2.40	2	180.0
C4-C1-N2-H0	C1-C2-N2-H0	0.0	1	0.0
C4-C4-C1-N2	C4-C4-C4-N2	3.10	2	180.0
C7-N2-C1-C4	C7-N2-C1-C3	1.80	1	0.0
OHS-CS-CS-N3	OH-C_L2-C_L2-NT	4.30	-1	180.0
		-0.40	3	180.0
HAS3-CAS3-CS-N3	H1-C2-C1-NT	0.2	3	0.0
C4-C4-OET-CS1	C4-C4-OET-C2	1.62	2	180.0
		0.19	4	180.0
C4-OET-CS1-HAS1	C4-OET-C2-H2	0.095	3	0.0
C4-OET-CS1-CS	C4-OET-C2-C2	0.24	1	0.0
		0.29	2	0.0
C4-OET-CS1-OS	CS-OET-CS1-OS	0.05	-1	180.0
		0.91	-2	0.0
		1.27	3	180.0
C4-C1-C7-OC2	C4-C4-C7-OC2	1.0	2	180.0
N2-C7-C1-C4	N2-C7-C1-C1	0.00	1	0.0

Table D.0.2: Table listing those approximate dihedral potential parameters for sections of the Vancomycin-peptide fragment complex that are not explicitly parameterised.

Bibliography

[1] S.S. Kardar. Antibiotic resistance: new approaches to a historical problem. *Action Bioscience*, 2005.

[2] S.B. Levy. Antibiotic resistance: Consequences of inaction. *Clinical Infectious Diseases*, 33(Supplement 3):S124–S129, 2001.

[3] N. E. Allen and T. I. Nicas. Mechanism of action of oritavancin and related glycopeptide antibiotics. *FEMS microbiology reviews*, 26:511–532, 2003.

[4] J.C.J. Barna and D.H. Williams. The structure and mode of action of glycopeptide antibiotics of the vancomycin group. *Annual Reviews in Microbiology*, 38(1):339–357, 1984.

[5] D.H. Williams and B. Bardsley. The vancomycin group of antibiotics and the fight against resistant bacteria. *Angewandte Chemie International Edition*, 38(9):1172–1193, 1999.

[6] H.R. Perkins. Specificity of combination between mucopeptide precursors and vancomycin or ristocetin. *Biochemical Journal*, 111(2):195, 1969.

[7] D. Kahne, C. Leimkuhler, W. Lu, and C. Walsh. Glycopeptide and lipoglycopeptide antibiotics. *Chem. Rev*, 105(2):425–448, 2005.

[8] D.H. Williams. Structural studies on some antibiotics of the vancomycin group, and on the antibiotic-receptor complexes, by proton NMR. *Accounts of Chemical Research*, 17(10):364–369, 1984.

[9] P.J. Loll and P.H. Axelsen. The structural biology of molecular recognition by vancomycin. *Annual Review of Biophysics and Biomolecular Structure*, 29(1):265–289, 2000.

[10] I. Chopra. Antibiotics. *eLS*, 2001.

[11] M. Nieto and H.R. Perkins. Modifications of the acyl-D-alanyl-D-alanine terminus affecting complex-formation with vancomycin. *Biochemical Journal*, 123(5):789, 1971.

[12] C. Walsh. Molecular mechanisms that confer antibacterial drug resistance. *Nature*, 406(6797):775–781, 2000.

[13] T.D.H. Bugg, G.D. Wright, S. Dutka-Malen, M. Arthur, P. Courvalin, and C.T. Walsh. Molecular basis for vancomycin resistance in Enterococcus faecium BM4147: biosynthesis of a depsipeptide peptidoglycan precursor by vancomycin resistance proteins VanH and VanA. *Biochemistry*, 30(43):10408–10415, 1991.

[14] H.C. Neu. The crisis in antibiotic resistance. *Science*, 257(5073):1064, 1992.

[15] J.W. Ndieyira, M. Watari, A.D. Barrera, D. Zhou, M. Vögtli, M. Batchelor, M.A. Cooper, T. Strunz, M.A. Horton, C. Abell, T. Rayment, G. Aeppli, and R.A. Mckendry. Nanomechanical detection of antibiotic-mucopeptide binding in a model for superbug drug resistance. *Nature Nanotechnology*, 3:691–696, Dec 2008.

[16] C.T. Walsh, S.L. Fisher, I-S. Park, M. Prahalad, and Z. Wu. Bacterial resistance to vancomycin: five genes and one missing hydrogen bond tell the story. *Chemistry and Biology*, 3(1):21 – 28, 1996.

[17] M. Arthur, P.E. Reynolds, F. Depardieu, S. Evers, S. Dutka-Malen, R. Quintiliani Jr, and P. Courvalin. Mechanisms of glycopeptide resistance in enterococci. *Journal of Infection*, 32(1):11 – 16, 1996.

[18] S.S.F. Leung, J. Tirado-Rives, and W.L. Jorgensen. Vancomycin analogs: Seeking improved binding of d-Ala-d-Ala and d-Ala-d-Lac peptides by side-chain and backbone modifications. *Bioorganic and Medicinal Chemistry*, 17(16):5874 – 5886, 2009.

[19] D.Y. Aksoy and S. Unal. New antimicrobial agents for the treatment of Gram-positive bacterial infections. *Clinical Microbiology and Infection*, 14(5):411–420, 2008.

[20] M.A. Cooper, M.T. Fiorini, C. Abell, and D.H. Williams. Binding of vancomycin group antibiotics to d-alanine and d-lactate presenting self-assembled monolayers. *Bioorg Med Chem*, 8:2609–2616, 2000.

[21] J.W. Ndieyira, A.D. Barrera, M. Vögtli, D. Zhou, M. Cooper, C. Abell, T. Strunz, G. Aeppli, and R. A. McKendry. Oritavancin's spectacular surface mode of action against superbugs.

[22] T.I. Nicas, D.L. Mullen, J.E. Flokowitsch, D.A. Preston, N.J. Snyder, M.J. Zweifel, S.C. Wilkie, M.J. Rodriguez, R.C. Thompson, and R.D. Cooper. Semisynthetic glycopeptide antibiotics derived from LY264826 active against vancomycin-resistant enterococci. *Antimicrobial Agents and Chemotherapy*, 40(9), 1996.

[23] N.E. Allen, D.L. LeTourneau, and J.N. Hobbs Jr. Molecular interactions of a semisynthetic glycopeptide antibiotic with D-alanyl-D-alanine and D-alanyl-D-lactate residues. *Antimicrobial Agents and Chemotherapy*, 41(1), 1997.

[24] J. Rao, L. Yan, J. Lahiri, G.M. Whitesides, R.M. Weis, and H.S. Warren. Binding of a dimeric derivative of vancomycin to l-Lys-d-Ala-d-lactate in solution and at a surface. *Chemistry & biology*, 6(6):353–359, 1999.

[25] Inc. Wolfram Research.

[26] H.N. Daghestani and B.W. Day. Theory and applications of surface plasmon resonance, resonant mirror, resonant waveguide grating, and dual polarization interferometry biosensors. *Sensors*, 10(11):9630–9646, 2010.

[27] C.K. O'Sullivan and G.G. Guilbault. Commercial quartz crystal microbalances: theory and applications. *Biosensors and Bioelectronics*, 14(8):663 – 670, 1999.

[28] N.S. Oliver, C. Toumazou, A.E.G. Cass, and D.G. Johnston. Glucose sensors: a review of current and emerging technology. *Diabetic Medicine*, 26(3):197–210, 2009.

[29] D.G. Georganopoulou, L. Chang, J.M. Nam, C.S. Thaxton, E.J. Mufson, W.L. Klein, and C.A. Mirkin. Nanoparticle-based detection in cerebral spinal fluid of a soluble pathogenic biomarker for Alzheimer's disease. *Proceedings of the National Academy of Sciences of the United States of America*, 102(7):2273, 2005.

[30] C.A. Rowe, S.B. Scruggs, M.J. Feldstein, J.P. Golden, and F.S. Ligler. An array immunosensor for simultaneous detection of clinical analytes. *Anal. Chem*, 71(2):433–439, 1999.

[31] B.B. Haab, M.J. Dunham, and P.O. Brown. Protein microarrays for highly parallel detection and quantitation of specific proteins and antibodies in complex solutions. *Genome Biol*, 2(2):1–13, 2001.

[32] M. Alvarez and L.M. Lechuga. Microcantilever-based platforms as biosensing tools. *Analyst*, 135:827–836, 2010.

[33] J. Rao, L. Yan, B. Xu, and G.M. Whitesides. Using surface plasmon resonance to study the binding of vancomycin and its dimer to self-assembled monolayers presenting D-Ala-D-Ala. *J. Am. Chem. Soc*, 121(11):2629–2630, 1999.

[34] P. Vettiger, J. Brugger, M. Despont, U. Drechsler, U. Durig, W. Haberle, M. Lutwyche, H. Rothuizen, R. Stutz, R. Widmer, et al. Ultrahigh density,

high-data-rate NEMS-based AFM data storage system. *Microelectronic Engineering*, 46(1-4):11–17, 1999.

[35] G. Binnig, C.F. Quate, and C. Gerber. Atomic force microscope. *Physical Review Letters*, 56(9):930–933, 1986.

[36] N.A. Burnham and R.J. Colton. Measuring the nanomechanical properties and surface forces of materials using an atomic force microscope. *Journal of Vacuum Science & Technology A: Vacuum, Surfaces, and Films*, 7(4):2906–2913, 2009.

[37] E.K. Dimitriadis, F. Horkay, J. Maresca, B. Kachar, and R.S. Chadwick. Determination of elastic moduli of thin layers of soft material using the atomic force microscope. *Biophysical journal*, 82(5):2798–2810, 2002.

[38] Y. Martin and H.K. Wickramasinghe. Magnetic imaging by force microscopy with 1000 Å resolution. *Applied Physics Letters*, 50(20):1455–1457, 2009.

[39] J.E. Stern, B.D. Terris, H.J. Mamin, and D. Rugar. Deposition and imaging of localized charge on insulator surfaces using a force microscope. *Applied Physics Letters*, 53(26):2717–2719, 2009.

[40] L.G. Carrascosa, M. Moreno, M. Álvarez, and L.M. Lechuga. Nanomechanical biosensors: a new sensing tool. *Trends in Analytical Chemistry*, 25(3):196 – 206, 2006.

[41] B. Ilic, Y. Yang, and H. G. Craighead. Virus detection using nanoelectromechanical devices. *Applied Physics Letters*, 85:2604–3, 2004.

[42] X. Li, H. Yu, X. Gan, X. Xia, P. Xu, J. Li, M. Liu, and Y. Li. Integrated mems/nems resonant cantilevers for ultrasensitive biological detection. *Journal of Sensors*, 2009.

[43] R. Raiteri, M. Grattarola, and R. Berger. Micromechanics senses biomolecules. *Materials Today*, 5(1):22 – 29, 2002.

[44] F. Tian, K.M. Hansen, T.L. Ferrell, T Thundat, and D.C. Hansen. Dynamic microcantilever sensors for discerning biomolecular interactions. *Analytical Chemistry*, 77(6):1601–1606, 2005.

[45] C. Wang, D. Wang, Y. Mao, and X. Hu. Ultrasensitive biochemical sensors based on microcantilevers of atomic force microscope. *Analytical Biochemistry*, 363(1):1 – 11, 2007.

[46] H-J. Butt. A sensitive method to measure changes in the surface stress of solids. *Journal of Colloid and Interface Science*, 180(1):251 – 260, 1996.

[47] F.M. Battiston, J.P. Ramseyer, H.P. Lang, M.K. Baller, C. Gerber, J.K. Gimzewski, E. Meyer, and H.J. Guntherodt. A chemical sensor based on a microfabricated cantilever array with simultaneous resonance-frequency and bending readout. *Sensors and Actuators B: Chemical*, 77(1-2):122–131, 2001.

[48] G.G. Stoney. The tension of metallic films deposited by electrolysis. *Proceedings of the Royal Society*, 9:172–175, 1909.

[49] C.A. Klein. How accurate are Stoney's equation and recent modifications? *Journal of Applied Physics*, 88:5487–5489, 2000.

[50] D.W. Dareing and T. Thundat. Simulation of adsorption-induced stress of a microcantilever sensor. *Journal of Applied Physics*, 97(4):043526 – 043526–5, February 2005.

[51] M.F. Hagan, A. Majumdar, and A.K. Chakraborty. Nanomechanical forces generated by surface grafted DNA. *The Journal of Physical Chemistry B*, 106(39):10163–10173, 2002.

[52] J-Q. Zhang, S-W. Yu, X-Q. Feng, and G-F. Wang. Theoretical analysis of adsorption-induced microcantilever bending. *Journal of Applied Physics*, 103:93506–93512, 2008.

[53] M.L. Sushko, J.H. Harding, A.L. Shluger, R.A. McKendry, and M. Watari. Physics of nanomechanical biosensing on cantilever arrays. *Advanced materials*, 20:3848–3853, 2008.

[54] M. Watari, J. Galbraith, H-P. Lang, M. Sousa, M. Hegner, C. Gerber, M.A. Horton, and R.A. McKendry. Investigating the molecular mechanisms of in-plane mechanochemistry on cantilever arrays. *Journal of the American Chemical Society*, 129(3):601–609, 2007.

[55] J.C. Stachowiak, M. Yue, K. Castelino, A. Chakraborty, and A. Majumdar. Chemomechanics of surface stresses induced by dna hybridization. *Langmuir*, 22(1):263–268, 2006.

[56] R. Berger, E. Delamarche, H.P. Lang, C. Gerber, J.K. Gimzewski, E. Meyer, and H.J. Guntherodt. Surface stress in the self-assembly of alkanethiols on gold. *Science*, 276(5321):2021, 1997.

[57] V. Srinivasan, G. Cicero, and J.C. Grossman. Adsorption-Induced Surface Stresses in Alkanethiolate-Au Self-Assembled Monolayers. *Physical Review Letters*, 101(18):185504, 2008.

[58] M. Godin, V. Tabard-Cossa, Y. Miyahara, T. Monga, P.J. Williams, L.Y. Beaulieu, R.B. Lennox, and P. Grütter. Cantilever-based sensing: the origin of surface stress and optimization strategies. *Nanotechnology*, 21:075501, 2010.

[59] B. Ilic, H.G. Craighead, S. Krylov, W. Senaratne, C. Ober, and P. Neuzil. Attogram detection using nanoelectromechanical oscillators. *Journal of Applied Physics*, 95:3694–10, 2004.

[60] S. Dohn, S. Schmid, F. Amiot, and A. Boisen. Position and mass determination of multiple particles using cantilever based mass sensors. *Applied Physics Letters*, 97:044103–3, 2010.

[61] A. K. Naik, M. S. Hanay, W. K. Hiebert, X. L. Feng, and M. L. Roukes. Towards single-molecule nanomechanical mass spectrometry. *Nature Nanotechnology*, 4:445–450, 2009.

[62] B. Lassagne, D. Garcia-Sanchez, A. Aguasca, and A. Bachtold. Ultrasensitive mass sensing with a nanotube electromechanical resonator. *Nano Letters*, 8:3735–3738, 2008.

[63] R.R. Grüter, Z. Khan, R. Paxman, J.W. Ndieyira, B. Dueck, B.A. Bircher, J.L. Yang, U. Drechsler, M. Despont, R.A. McKendry, and B.W. Hoogenboom. Disentangling mechanical and mass effects on nanomechanical resonators. *Applied Physics Letters*, 96(2):023113, January 2010.

[64] J. Tamayo, D. Ramos, J. Mertens, and M. Calleja. Effect of the adsorbate stiffness on the resonance response of microcantilever sensors. *Applied Physics Letters*, 89:224104–3, 2006.

[65] J. Fritz, M.K. Baller, H.P. Lang, H. Rothuizen, P. Vettiger, E. Meyer, H. Guntherhodt, C. Gerber, and J.K. Gimzewski. Translating biomolecular recognition into nanomechanics. *Science*, 288:5464, 2000.

[66] R.A. McKendry, J. Zhang, Y. Arntz, T. Strunz, M. Hegner, H.P. Lang, M.K. Baller, U. Certa, E. Meyer, H.J. Güntherodt, et al. Multiple label-free biodetection and quantitative DNA-binding assays on a nanomechanical cantilever array. *Proceedings of the National Academy of Sciences of the United States of America*, 99(15):9783, 2002.

[67] C.A. Savran, S.M. Knudsen, A.D. Ellington, and S.R. Manalis. Micromechanical detection of proteins using aptamer-based receptor molecules. *Analytical Chemistry*, 76(11):3194–3198, 2004.

[68] M. Calleja, M. Nordstrom, M. Alvarez, J. Tamayo, L.M. Lechuga, and A. Boisen. Highly sensitive polymer-based cantilever-sensors for DNA detection. *Ultramicroscopy*, 105(1-4):215–222, 2005.

[69] J. Zhang, H.P. Lang, F. Huber, A. Bietsch, W. Grange, U. Certa, R. McKendry, H.J. Guntherodt, M. Hegner, and C. Gerber. Rapid and label-free nanomechanical detection of biomarker transcripts in human RNA. *Nature Nanotechnology*, 1(3):214–220, 2006.

[70] K.M. Hansen, H.F. Ji, G. Wu, R. Datar, R. Cote, A. Majumdar, and T. Thundat. Cantilever-based optical deflection assay for discrimination of DNA single-nucleotide mismatches. *Anal. Chem*, 73(7):1567–1571, 2001.

[71] W. Shu, D. Liu, M. Watari, C.K. Riener, T. Strunz, M.E. Welland, S. Balasubramanian, and R.A. McKendry. DNA molecular motor driven micromechanical cantilever arrays. *J. Am. Chem. Soc*, 127(48):17054–17060, 2005.

[72] Y. Yang, H.F. Ji, and T. Thundat. Nerve agents detection using a Cu2+/L-cysteine bilayer-coated microcantilever. *J. Am. Chem. Soc*, 125(5):1124–1125, 2003.

[73] B.L. Weeks, J. Camarero, A. Noy, A.E. Miller, J.J. De Yoreo, and L. Stanker. A microcantilever-based pathogen detector. *Scanning*, 25(6):297–299, 2003.

[74] S-H. Tark, A. Das, S. Sligar, and V.P. Dravid. Nanomechanical detection of cholera toxin using microcantilevers functionalised with ganglioside nanodiscs. *Nanotechnology*, 21:435502, 2010.

[75] L.A. Pinnaduwage, A. Gehl, D.L. Hedden, G. Muralidharan, T. Thundat, R.T. Lareau, T. Sulchek, L. Manning, B. Rogers, M. Jones, et al. Explosives: A microsensor for trinitrotoluene vapour. *Nature*, 425(6957):474, 2003.

[76] A. Subramanian, P.I. Oden, S.J. Kennel, K.B. Jacobson, R.J. Warmack, T. Thundat, and M.J. Doktycz. Glucose biosensing using an enzyme-coated microcantilever. *Applied Physics Letters*, 81:385, 2002.

[77] W. Shu, S. Laurenson, T.P.J. Knowles, P. Ko Ferrigno, and A.A. Seshia. Highly specific label-free protein detection from lysed cells using internally referenced microcantilever sensors. *Biosensors and Bioelectronics*, 24(2):233–237, 2008.

[78] G.A.J. Besselink, R.P.H. Kooyman, P.J.H.J. van Os, G.H.M. Engbers, and R. Schasfoort. Signal amplification on planar and gel-type sensor surfaces in surface plasmon resonance-based detection of prostate-specific antigen. *Analytical biochemistry*, 333(1):165–173, 2004.

[79] Y. Arntz, J.D. Seelig, H-P. Lang, J. Zhang, P. Hunziker, J.P. Ramseyer, E. Meyer, M. Hegner, and C. Gerber. Label-free protein assay based on a nanomechanical cantilever array. *Nanotechnology*, 14:86, 2003.

[80] A.M. Moulin, S.J. O'Shea, R.A. Badley, P. Doyle, and M.E. Welland. Measuring surface-induced conformational changes in proteins. *Langmuir*, 15(26):8776–8779, 1999.

[81] T.P.J. Knowles, W. Shu, F. Huber, H.P. Lang, C. Gerber, C.M. Dobson, and M.E. Welland. Label-free detection of amyloid growth with microcantilever sensors. *Nanotechnology*, 19:384007, 2008.

[82] D. Ramos, M. Calleja, J. Mertens, A. Zaballos, and J. Tamayo. Measurement of the mass and rigidity of adsorbates on a microcantilever sensor. *Sensors*, 7:1834–1845, 2007.

[83] S. Kim, D. Yi, A. Passian, and T. Thundat. Observation of an anomalous mass effect in microcantilever-based biosensing caused by adsorbed DNA. *Applied Physics Letters*, 96:153703–3, 2010.

[84] Y. Lee, G. Lim, and W. Moon. A self-excited micro cantilever biosensor actuated by PZT using the mass micro balancing technique. *Sensors and Actuators A: Physical*, 130-131:105 – 110, 2006.

[85] E. Gil-Santos, D. Ramos, J. Martinez, M. Fernandez-Regulez, R. Garcia, A. San Paulo, M. Calleja, and J. Tamayo. Nanomechanical mass sensing

and stiffness spectrometry based on two-dimensional vibrations of resonant nanowires. *Nature Nanotechnology*, 5:641–645, 2010.

[86] M. Varshney, P.S. Waggoner, R.A. Montagna, and H.G. Craighead. Prion protein detection in serum using micromechanical resonator arrays. *Talanta*, 80(2):593–599, 2009.

[87] A. Agoston, F. Keplinger, and B. Jakoby. Evaluation of a vibrating micromachined cantilever sensor for measuring the viscosity of complex organic liquids. *Sensors and Actuators A: Physical*, 123-124:82 – 86, 2005. Eurosensors XVIII 2004 - The 18th European conference on Solid-State Transducers.

[88] T.P. Burg, M. Godin, S.M. Knudsen, W. Shen, G. Carlson, J.S. Foster, K. Babcock, and S.R. Manalis. Weighing of biomolecules, single cells and single nanoparticles in fluid. *Nature*, 446:1066–1069, 2007.

[89] D.C. Rapaport. *The art of molecular dynamics simulation*. Cambridge University Press, 2004.

[90] B.D. Todd and R.M. Lynden-Bell. Surface and bulk properties of metals modelled with sutton-chen potentials. *Surface Science*, 281(1):191 – 206, 1993.

[91] M.S. Daw, S.M. Foiles, and M.I. Baskes. The embedded-atom method: a review of theory and applications. *Materials Science Reports*, 9(7):251 – 310, 1993.

[92] J. Hautman and M.L. Klein. Simulation of a monolayer of alkyl thiol chains. *Journal of Chemical Physics*, 91:4994+, May 1989.

[93] J. Tersoff. Empirical interatomic potential for carbon, with applications to amorphous carbon. *Phys. Rev. Lett.*, 61:2879–2882, Dec 1988.

[94] A.D. MacKerell, D. Bashford, Bellott, R.L. Dunbrack, J.D. Evanseck, M.J. Field, S. Fischer, J. Gao, H. Guo, S. Ha, D. Joseph, L. Kuchnir, K. Kuczera, F.T.K. Lau, C. Mattos, S. Michnick, T. Ngo, D.T.

Nguyen, B. Prodhom, W.E. Reiher, B. Roux, M. Schlenkrich, J.C. Smith, R. Stote, J. Straub, M. Watanabe, J. Wiórkiewicz-Kuczera, D. Yin, and M. Karplus. All-atom empirical potential for molecular modeling and dynamics studies of proteins. *The Journal of Physical Chemistry B*, 102(18):3586–3616, 1998.

[95] K. Vanommeslaeghe, E. Hatcher, C. Acharya, S. Kundu, S. Zhong, J. Shim, E. Darian, O. Guvench, P. Lopes, I. Vorobyov, and A. D. Mackerell. Charmm general force field: A force field for drug-like molecules compatible with the charmm all-atom additive biological force fields. *Journal of Computational Chemistry*, 31(4):671–690, 2010.

[96] D. Frenkel and B. Smit. *Understanding molecular simulation: From algorithms to applications*. Academic Press, 2002.

[97] W. Smith, T.R. Forester, and I.T. Todorov. *The DL POLY 2.0 User Manual*, 2.19 edition, 2008.

[98] K.L. Prime and G.M. Whitesides. Adsorption of proteins onto surfaces containing end-attached oligo (ethylene oxide): a model system using self-assembled monolayers. *Journal of the American Chemical Society*, 115(23):10714–10721, 1993.

[99] J. Lahiri, L. Isaacs, J. Tien, and G.M. Whitesides. A strategy for the generation of surfaces presenting ligands for studies of binding based on an active ester as a common reactive intermediate: a surface plasmon resonance study. *Anal. Chem*, 71(4):777–790, 1999.

[100] A.G. Hansen, M.W. Mortensen, J.E.T. Andersen, J. Ulstrup, A Kuhle, J. Garnaes, and A. Boisen. Stress formation during self-assembly of alkanethiols on differently pre-treated gold surfaces. *Probe microscopy*, 2:139–149, 2001.

[101] G. Wu, H. Ji, K. Hansen, T. Thundat, R. Datar, R. Cote, M.F. Hagan, A.K. Chakraborty, and A. Majumdar. Origin of nanomechanical can-

tilever motion generated from biomolecular interactions. *Proceedings of the National Academy of Sciences*, 98(4):1560–1564, 2001.

[102] R. Marie, H. Jensenius, J. Thaysen, C.B. Christensen, and A. Boisen. Adsorption kinetics and mechanical properties of thiol-modified dna-oligos on gold investigated by microcantilever sensors. *Ultramicroscopy*, 91(1):29 – 36, 2002.

[103] S. Kohale, S.M. Molina, B.L. Weeks, R. Khare, and L.J. Hope-Weeks. Monitoring the formation of self-assembled monolayers of alkanedithiols using a micromechanical cantilever sensor. *Langmuir*, 23(3):1258–1263, 2007.

[104] F. Zhou, W. Shu, M.E. Welland, and W.T.S. Huck. Highly reversible and multi-stage cantilever actuation driven by polyelectrolyte brushes. *Journal of the American Chemical Society*, 128(16):5326–5327, 2006.

[105] C. Vericat, M. E. Vela, G. A. Benitez, J. A. M. Gago, X. Torrelles, and R. C. Slavarezza. Surface characterisation of sulphur and alkanethiol self-assembled monolayers on Au(111). *Journal of Physics: Condensed Matter*, 18:868–900, 2006.

[106] V. Tabard-Cossa, M. Godin, I.J. Burgess, T. Monga, R.B. Lennox, and P. Grütter. Microcantilever-based sensors: Effect of morphology, adhesion, and cleanliness of the sensing surface on surface stress. *Analytical Chemistry*, 79(21):8136–8143, 2007.

[107] R. Desikan, I. Lee, and T. Thundat. Effect of nanometer surface morphology on surface stress and adsorption kinetics of alkanethiol self-assembled monolayers. *Ultramicroscopy*, 106(8-9):795 – 799, 2006.

[108] P. Shrotriya, K.K.S. Karuppiah, R. Zhang, A. Chandra, and S. Sundararajan. Surface stress generation during formation of alkanethiol self-assembled monolayer (SAM). *Mechanics Research Communications*, 35(1-2):43–49, 2008.

[109] J. Israelachvili. *Intermolecular & surface forces*. Academic Press, 1992.

[110] W. Haiss. Surface stress of clean and adsorbate-covered solids. *Reports of Progress in Physics*, 64:591–648, 2000.

[111] H. Ibach. The role of surface stress in reconstruction, epitaxial growth and stabilization of mesoscopic structures. *Surface Science Reports*, 29(5-6):195–263, 1997.

[112] J.G. Zhou and F. Hagelberg. Do methanethiol adsorbates on the Au (111) surface dissociate? *Physical review letters*, 97(4):45505, 2006.

[113] T. Hayashi, Y. Morikawa, and H. Nozoye. Adsorption state of dimethyl disulfide on Au (111): Evidence for adsorption as thiolate at the bridge site. *The Journal of Chemical Physics*, 114:7615, 2001.

[114] V. De Renzi, R. Di Felice, D. Marchetto, R. Biagi, U. del Pennino, and A. Selloni. Ordered (3 $\times$ 4) high-density phase of methylthiolate on Au (111). *J. Phys. Chem. B*, 108(1):16–20, 2004.

[115] I.I. Rzeźnicka, J. Lee, P. Maksymovych, and J.T. Yates Jr. Nondissociative chemisorption of short chain alkanethiols on Au (111). *J. Phys. Chem. B*, 109(33):15992–15996, 2005.

[116] J.C. Love, L.A. Estroff, J.K. Kriebel, R.G. Nuzzo, and G.M. Whitesides. Self-assembled monolayers of thiolates on metals as a form of nanotechnology. *Chem. Rev*, 105(4):1103–1170, 2005.

[117] A. Ulman. Formation and structure of self-assembled monolayers. *Chem. Rev*, 96(4):1533–1554, 1996.

[118] F. Schreiber. Self-assembled monolayers: from simple model systems to biofunctionalized interfaces. *J. Phys.: Condens. Matter*, 16:R881–R900, 2004.

[119] G.E. Poirier and E.D. Pylant. The self-assembly mechanism of alkanethiols on Au(111). *Science(Washington)*, 272(5265):1145–1145, 1996.

[120] C.D. Bain, E.B. Troughton, Y.T. Tao, J. Evall, G.M. Whitesides, and R.G. Nuzzo. Formation of monolayer films by the spontaneous assembly of organic thiols from solution onto gold. *Journal of the American Chemical Society*, 111(1):321–335, 1989.

[121] B.T. Houseman, E.S. Gawalt, and M. Mrksich. Maleimide-Functionalized Self-Assembled Monolayers for the Preparation of Peptide and Carbohydrate Biochips. *Langmuir*, 19(5):1522–1531, 2003.

[122] E.A. Smith, M.J. Wanat, Y. Cheng, S.V.P. Barreira, A.G. Frutos, and R.M. Corn. Formation, spectroscopic characterization, and application of sulfhydryl-terminated alkanethiol monolayers for the chemical attachment of DNA onto gold surfaces. *Langmuir*, 17(8):2502–2507, 2001.

[123] E.A. Smith, W.D. Thomas, L.L. Kiessling, and R.M. Corn. Surface plasmon resonance imaging studies of protein-carbohydrate interactions. *J. Am. Chem. Soc*, 125(20):6140–6148, 2003.

[124] G.J. Wegner, H.J. Lee, and R.M. Corn. Characterization and optimization of peptide arrays for the study of epitope- antibody interactions using surface plasmon resonance imaging. *Anal. Chem*, 74(20):5161–5168, 2002.

[125] J.P. Collman, N.K. Devaraj, and C.E.D. Chidsey. 'Clicking' functionality onto electrode surfaces. *Langmuir*, 20(4):1051–1053, 2004.

[126] C.D. Hodneland, Y.S. Lee, D.H. Min, and M. Mrksich. Selective immobilization of proteins to self-assembled monolayers presenting active site-directed capture ligands. *Proceedings of the National Academy of Sciences of the United States of America*, 99(8):5048, 2002.

[127] S. Choi and W.L. Murphy. Multifunctional mixed SAMs that promote both cell adhesion and noncovalent DNA immobilization. *Langmuir*, 24(13):6873–6880, 2008.

[128] E. Barrena, E. Palacios-Lidón, C. Munuera, X. Torrelles, S. Ferrer, U. Jonas, M. Salmeron, and C. Ocal. The role of intermolecular and

molecule-substrate interactions in the stability of alkanethiol nonsaturated phases on Au(111). *Journal of the American Chemical Society*, 126(1):385–395, 2004. PMID: 14709106.

[129] F. Terán Arce, M.E. Vela, R.C. Salvarezza, and A.J. Arvia. Complex structural dynamics at adsorbed alkanethiol layers at Au(111) single-crystal domains. *Langmuir*, 14(25):7203–7212, 1998.

[130] M.C. Vargas, P. Giannozzi, A. Selloni, and G. Scoles. Coverage-dependent adsorption of CH3S and (CH3S)2 on Au(111): a density functional theory study. *The Journal of Physical Chemistry B*, 105(39):9509–9513, 2001.

[131] X. Torrelles, E. Barrena, C. Munuera, J. Rius, S. Ferrer, and C. Ocal. New insights in the c(4 x 2) reconstruction of hexadecanethiol on au(111) revealed by grazing incidence x-ray diffraction. *Langmuir*, 20(21):9396–9402, 2004. PMID: 15461535.

[132] P. Fenter, A. Eberhardt, and P. Eisenberger. Self-assembly of n-alkyl thiols as disulfides on au(111). *Science*, 266(5188):1216–1218, 1994.

[133] M. Tachibana, K. Yoshizawa, A. Ogawa, H. Fujimoto, and R. Hoffmann. Sulfur- Gold Orbital Interactions which Determine the Structure of Alkanethiolate/Au (111) Self-Assembled Monolayer Systems. *J. Phys. Chem. B*, 106(49):12727–12736, 2002.

[134] C. Masens, M.J. Ford, and M.B. Cortie. The effect of surface symmetry on the adsorption energetics of SCH3 on gold surfaces studied using Density Functional Theory. *Surface Science*, 580(1-3):19–29, 2005.

[135] J. Gottschalck and B. Hammer. A density functional theory study of the adsorption of sulfur, mercapto, and methylthiolate on Au(111). *Journal of Chemical Physics*, 116:784–790, January 2002.

[136] M.G. Roper, M.P. Skegg, C.J. Fisher, J.J. Lee, V.R. Dhanak, D.P. Woodruff, and R.G. Jones. Atop adsorption site of sulphur head groups

in gold-thiolate self-assembled monolayers. *Chemical Physics Letters*, 389(1):87 – 91, 2004.

[137] H. Kondoh, M. Iwasaki, T. Shimada, K. Amemiya, T. Yokoyama, T. Ohta, M. Shimomura, and S. Kono. Adsorption of thiolates to singly coordinated sites on Au(111) evidenced by photoelectron diffraction. *Phys. Rev. Lett.*, 90:066102, Feb 2003.

[138] R.P.S. Fartaria, F.F.M. Freitas, and F.M.S. Silva-Fernandes. A preliminary study of alkylthiols self-assembly on gold electrodes by computer simulation.

[139] M.L. Sushko and A.L. Shluger. Dipole- dipole interactions and the structure of self-assembled monolayers. *J. Phys. Chem. B*, 111(16):4019–4025, 2007.

[140] B. R. Brooks, R. E. Bruccoleri, B. D. Olafson, D. J. States, S. Swaminathan, and M. Karplus. Charmm: A program for macromolecular energy, minimization, and dynamics calculations. *Journal of Computational Chemistry*, 4:187–217, 1983.

[141] A.J. Pertsin and M. Grunze. Monte-carlo studies of self-assembled monolayers using simple generalized models. 2. a 2-site molecular-model. *Journal of Chemical Physics*, 106(17):7343–7351, 1997.

[142] X. Torrelles, C. Vericat, M.E. Vela, M.H. Fonticelli, M.M.A. Daza, R. Felici, T.L. Lee, J. Zegenhagen, G. Munoz, J.A. Martin-Gago, et al. Two-site adsorption model for the ($\sqrt{3}$ x $\sqrt{3}$)-R30 degrees dodecanethiolate lattice on Au (111) surfaces. *The Journal of Physical Chemistry. B*, 110(11):5586, 2006.

[143] H. Kondoh, A. Nambu, Y. Ehara, F. Matsui, T. Yokoyama, and T. Ohta. Substrate dependence of self-assembly of alkanethiols: X-ray absorption fine structure study. *The Journal of Physical Chemistry B*, 108(34):12946–12954, 2004.

[144] L.H. Dubois and R.G. Nuzzo. Synthesis, structure, and properties of model organic surfaces. *Annual Review of Physical Chemistry*, 43(1):437–463, 1992.

[145] A. Ulman, J.E. Eilers, and N. Tillman. Packing and molecular orientation of alkanethiol monolayers on gold surfaces. *Langmuir*, 5(5):1147–1152, 1989.

[146] S-I. Imabayashi, D. Hobara, and T. Kakiuchi. Voltammetric detection of the surface diffusion of adsorbed thiolate molecules in artificially phase-separated binary self-assembled monolayers on an Au(111) surface. *Langmuir*, 17(9):2560–2563, 2001.

[147] M. Yu, N. Bovet, C.J. Satterley, S. Bengió, K.R.J. Lovelock, P.K. Milligan, R.G. Jones, D.P. Woodruff, and V. Dhanak. True nature of an archetypal self-assembly system: Mobile Au-thiolate species on Au(111). *Phys. Rev. Lett.*, 97:166102, Oct 2006.

[148] F.P. Cometto, P. Paredes-Olivera, V.A. Macagno, and E.M. Patrito. Density functional theory study of the adsorption of alkanethiols on Cu (111), Ag (111), and Au (111) in the low and high coverage regimes. *J. Phys. Chem. B*, 109(46):21737–21748, 2005.

[149] G. Heimel, L. Romaner, J.L. Brédas, and E. Zojer. Organic/metal interfaces in self-assembled monolayers of conjugated thiols: A first-principles benchmark study. *Surface Science*, 600(19):4548–4562, 2006.

[150] X.D. Cui, X. Zarate, J. Tomfohr, O.F. Sankey, A. Primak, A.L. Moore, T.A. Moore, D. Gust, G. Harris, and S.M. Lindsay. Making electrical contacts to molecular monolayers. *Nanotechnology*, 13:5–14, February 2002.

[151] L. Duan and S.J. Garrett. An investigation of rigid p-methylterphenyl thiol self-assembled monolayers on Au(111) using reflection absorption infrared spectroscopy and scanning tunneling microscopy. *The Journal of Physical Chemistry B*, 105(40):9812–9816, 2001.

[152] H. Grönbeck, H. Häkkinen, and R.L. Whetten. Gold thiolate complexes form a unique c(4 x 2) structure on Au(111). *The Journal of Physical Chemistry C*, 112(41):15940–15942, 2008.

[153] V. Fiorentini, M. Methfessel, and M. Scheffler. Reconstruction mechanism of fcc transition metal (001) surfaces. *Physical review letters*, 71(7):1051–1054, 1993.

[154] P.J. Feibelman. Anisotropy of the stress on fcc (110) surfaces. *Physical Review B*, 51(24):17867–17875, 1995.

[155] C.W. Mays, J.S. Vermaak, and D. Kuhlmann-Wilsdorf. On surface stress and surface tension: II. Determination of the surface stress of gold. *Surface Science*, 12(2):134–140, 1968.

[156] W.R. Tyson and W.A. Miller. Surface free energies of solid metals: Estimation from liquid surface tension measurements. *Surface Science*, 62(1):267–276, 1977.

[157] M. Buck, M. Grunze, F. Eisert, J. Fischer, and F. Trager. Adsorption kinetics of n-alkyl thiols on gold studied by second harmonic generation and x-ray photoelectron spectroscopy. *Journal of Vacuum Science & Technology A: Vacuum, Surfaces, and Films*, 10(4):926–929, 2009.

[158] T. Wink, S.J. van Zuilen, A. Bult, and W.P. van Bennekom. Self-assembled monolayers for biosensors. *Analyst*, 122:43R–50R, 1997.

[159] M.M. Biener, J. Biener, and C.M. Friend. Revisiting the S- Au (111) interaction: Static or dynamic? *Langmuir*, 21(5):1668–1671, 2005.

[160] J. Mertens, C. Rogero, M. Calleja, D. Ramos, J.A. Martin-Gago, C. Briones, and J. Tamayo. Label-free detection of DNA hybridization based of hydration induced tension in nucleic acid films. *Nature Nanotechnology*, 3:301–307, 2008.

[161] D. Stauffer and A. Aharony. *Introduction to percolation theory*. CRC Press, 1991.

[162] M. Schäfer, T.R. Schneider, and G.M. Sheldrick. Crystal structure of vancomycin. *Structure*, 4(12):1509–1515, 1996.

[163] www.accelrys.com.

[164] www.rscb.org/pdb.

[165] W.G. Prowse, A.D. Kline, M.A. Skelton, and R.J. Loncharich. Conformation of a82846b, a glycopeptide antibiotic, complexed with its cell wall fragment: an asymmetric homodimer determined using nmr spectroscopy. *Biochemistry*, 34(29):9632–9644, 1995.

[166] C.W. Yong. *DL_FIELD v1.0*. STFC Daresbury Laboratory, 2010.

[167] C. Vericat, M.E. Vela, and R.C. Salvarezza. Self-assembled monolayers of alkanethiols on Au(111): surface structures, defects and dynamics. *Phys. Chem. Chem. Phys.*, 7:3258–3268, 2005.

[168] K. Tamada, T. Ishida, W. Knoll, H. Fukushima, R. Colorado, M. Graupe, O.E. Shmakova, and T.R. Lee. Molecular packing of semifluorinated alkanethiol self-assembled monolayers on gold: Influence of alkyl spacer length. *Langmuir*, 17(6):1913–1921, 2001.

[169] S.E. Creager, L.A. Hockett, and G.K. Rowe. Consequences of microscopic surface roughness for molecular self-assembly. *Langmuir*, 8(3):854–861, 1992.

[170] N.G. Semaltianos and E.G. Wilson. Investigation of the surface morphology of thermally evaporated thin gold films on mica, glass, silicon and calcium fluoride substrates by scanning tunneling microscopy. *Thin Solid Films*, 366(1):111 – 116, 2000.

[171] www.memsnet.org/materials.

[172] www.sigmaaldrich.com/materials-science.

[173] A.W. Farland and J.S. Colton. Chemical sensing with micromolded plastic microcantilevers. *Journal of Microelectromechanical Systems*, 14(6), 2005.

[174] K.M. Goeders, J.S. Colton, and L.A. Bottomley. Microcantilevers: Sensing chemical iinteractions via mechanical motion. *Chemical Reviews*, 108:522–542, 2008.

[175] M. Nordstrom, S. Keller, M. Lillemose, A. Johansson, S. Dohn, G. Blagoi, M Havsteen-Jakobsen, and A. Boisen. Su-8 cantilevers for bio/chemical sensing; fabrication, characterisation and development of novel read-out methods. *Sensors*, 8:1595–1612, 2008.

[176] S.S. Wong, E. Joselevich, A.T. Woolley, C.L. Cheung, and C.M. Lieber. Covalently functionalized nanotubes as nanometer-sized probes in chemistry and biology. *Nature*, 394:52–55, 1998.

[177] D. Lee, S. Kim, N. Jung, T. Thundat, and S. Jeon. Effects of gold patterning on the bending profile and frequency response of a microcantilever. *Journal of Applied Physics*, 106:024310–7, 2009.

[178] L. D. Landau and E. M. Lifshitz. *Theory of elasticity.* Pergamon Press, 1970.

[179] J.E. Sader. Frequency response of cantilever beams immersed in viscous fluids with applications to the atomic force microscope. *Journal of Applied Physics*, 84:64–76, 1998.

[180] C.A. Van Eysden and J.E. Sader. Frequency response of cantilever beams immersed in viscous fluids with applications to the atomic force microscope: Arbitrary mode order. *Journal of Applied Physics*, 101:044908, 2007.

[181] S. Tetin, B. Caillard, F. Menil, H. Debeda, C. Lucat, C. Pellet, and I. Dufour. Modeling and performance of uncoated microcantilever-based chemical sensors. *Sensors and Actuators B: Chemical*, 143(2):555 – 560, 2010.

[182] N. Ahmed, D.F. Nino, and V.T. Moy. Measurement of solution viscosity by atomic force microscopy. *Review of scientific instruments*, 72:2731–2735, 2001.

[183] E. M. Purcell. Life at low Reynold's number. *American Journal of Physics*, 45:3–11, 1977.

[184] G. K. Batchelor. *An introduction to fluid dynamics*. Cambridge university press, 1967.

[185] H. Hosaka, K. Itao, and S. Kuroda. Damping characteristics of beam-shaped micro-oscillators. *Sensors and Actuators A*, 49:87–95, 1995.

[186] C. Tropea, A.L. Yarin, and J.F. Foss. *Springer handbook of experimental fluid mechanics*. Springer Verlag, 2007.

[187] S. Bruckenstein and M. Shay. Experimental aspects of use of the quartz crystal microbalance in solution. *Electrochimica Acta*, 30(10):1295–1300, 1985.

[188] P. Abgrall and A.M. Gue. Lab-on-chip technologies: making a microfluidic network and coupling it into a complete microsystem: a review. *Journal of Micromechanics and Microengineering*, 17:R15, 2007.

[189] P. Vettiger, M. Despont, U. Drechsler, U. Durig, W. Haberle, M.I. Lutwyche, H.E. Rothuizen, R. Stutz, R. Widmer, and G.K. Binnig. The Millipede: More than thousand tips for future AFM storage. *IBM Journal of Research and Development*, 44(3):323–340, 2010.

[190] C.A. Van Eysden and J.E. Sader. Resonant frequencies of a rectangular cantilever beam immersed in a fluid. *Journal of Applied Physics*, 100:114916–8, 2006.

[191] F-J. Elmer and M. Dreier. Eigenfrequencies of a rectangular atomic force micrscope cantilever in a medium. *Journal of Applied Physics*, 81:7709–6, 1997.

[192] G. Muthuveerappan, N. Ganesan, and M.A. Veluswami. A note on vibration of a cantilever plate immersed in water. *Journal of Sound and Vibration*, 63(3):385 – 391, 1979.

[193] G. Muthuveerappan, N. Ganesan, and MA Veluswami. Vibrations of skew plates immersed in water. *Computers & Structures*, 21(3):479–491, 1985.

[194] D.G. Crighton. Resonant oscillations of fluid-loaded struts. *Journal of Sound and Vibration*, 87(3):429–437, 1983.

[195] Y. Fu and W.G. Price. Interactions between a partially or totally immersed vibrating cantilever plate and the surrounding fluid. *Journal of Sound and vibration*, 118(3):495–513, 1987.

[196] S. Inaba, K. Akaishi, T. Mori, and K. Hane. Analysis of the resonance characteristics of a cantilever vibrated photothermally in a liquid. *Journal of applied physics*, 73(6):2654–2658, 2009.

[197] H.J. Butt, P. Siedle, K. Seifert, K. Fendler, T. Seeger, E. Bamberg, A.L. Weisenhorn, K. Goldie, and A. Engel. Scan speed limit in atomic force microscopy. *Journal of microscopy*, 169:75–84, 1993.

[198] G.Y. Chen, R.J. Warmack, T. Thundat, D.P. Allison, and A. Huang. Resonance response of scanning force microscopy cantilevers. *Review of Scientific Instruments*, 65(8):2532 –2537, August 1994.

[199] M.R. Paul and M.C. Cross. Stochastic dynamics of nanoscale mechanical oscillators immersed in a viscous fluid. *Phys. Rev. Lett.*, 92(23):235501, Jun 2004.

[200] A. Maali, C. Hurth, R. Boisgard, C. Jai, T. Cohen-Bouhacina, and J-P. Aime. Hydrodynamics of oscillating atomic force microscopy cantilevers in viscous fluids. *Journal of Applied Physics*, 97:074907–6, 2005.

[201] L. D. Landau and E. M. Lifshitz. *Fluid Mechanics*. Pergamon Press, 1987.

[202] S.P. Timoshenko. On the transverse vibrations of bars of uniform cross-section. *Philosophical Magazine Series 6*, 43(253):125–131, 1922.

[203] L.C. Andrews. *Special functions for engineers and applied mathematicians*. Macmillan, 1985.

[204] C.A. Van Eysden and J.E. Sader. Small amplitude oscillations of a flexible thin blade in a viscous fluid: Exact analytical solution. *Physics of Fluids*, 18:123102–11, 2006.

[205] P. Brunetto, L. Fortuna, P. Giannone, S. Graziani, and F. Pagano. A small scale viscometer based on an ipmc actuator and an ipmc sensor. In *Instrumentation and Measurement Technology Conference (I2MTC), 2010 IEEE*, pages 585 –589, may 2010.

[206] M. Hennemeyer, S. Burghardt, and R.W. Stark. Cantilever microrheometer for the characterization of sugar solutions. *Sensors*, 8:10–22, 2008.

[207] C. Bergaud and L. Nicu. Viscosity measurements based on experimental investigations of composite cantilever beam eigenfrequencies in viscous media. *Review of Scientific Instruments*, 71:2487–2492, 2000.

[208] S. Boskovic, J.W.M Chon, P. Mulvaney, and J.E. Sader. Rheological measurements using microcantilevers. *Journal of Rheology*, 46:891–899, 2002.

[209] N. McLoughlin, S.L. Lee, and G. Hahner. Simultaneous determination of density and viscosity of liquids based on resonance curves of uncalibrated microcantilevers. *Applied Physics Letters*, 89:184106–3, 2006.

[210] M.K. Ghatkesar, T. Braun, V. Barwich, J-P. Ramseyer, C. Gerber, M. Hegner, and H.P. Lang. Resonating modes of vibrating microcantilevers in liquid. *Applied Physics Letters*, 92:043106–3, 2008.

[211] M.K. Ghatkesar, V. Barwich, T. Braun, J-P. Ramseyer, C. Gerber, M. Hegner, H.P. Lang, U. Drechsler, and M. Despont. Higher modes of vibration increase mass sensitivity in nanomechanical microcantilevers. *Nanotechnology*, 18:445502, 2007.

[212] A. Arturas Ulcinas and V. Valentinas Snitka. Intermittent contact afm using the higher modes of weak cantilever. *Ultramicroscopy*, 86(1):217–222, 2001.

[213] S.J.T. van Noort, O.H. Willemsen, K.O. van der Werf, B.G. de Grooth, and J. Greve. Mapping electrostatic forces using higher harmonics tapping mode atomic force microscopy in liquid. *Langmuir*, 15(21):7101–7107, 1999.

[214] T. Ikehara, J. Lu, M. Konno, R. Maeda, and T. Mihara. A high quality-factor silicon cantilever for a low detection-limit resonant mass sensor operated in air. *Journal of Micromechanical Microengineering*, 17:2491–2494, 2007.

[215] R. Paxman, J. Stinson, A. Dejardin, R.A. McKendry, and B.W. Hoogenboom. Using micromechanical resonators to measure rheological properties and alcohol content of model solution and commercial beverages. *Sensors*, 12:6497–6507, 2012.

[216] W. Humphrey, A. Dalke, and K. Schulten. VMD - visual molecular dynamics. *Journal of Molecular Graphics*, 14:33–38, 1996.

[217] Y.W. Kwon and H. Bang. *The finite element method using MATLAB*. CRC Press, 2 edition, 2000.

[218] J.-H. Fabian, L. Scandella, H. Fuhrmann, R. Berger, T. Mezzacasa, C. Musil, J. Gobrecht, and E. Meyer. Finite element calculations and fabrication of cantilever sensors for nanoscale detection. *Ultramicroscopy*, 82(1):69 – 77, 2000.

[219] W.M. Haynes. *CRC handbook of chemistry and physics*. CRC Press, 91 edition, 2010.

[220] J.F. Steffe. *Rheological methods in food processing engineering*. Freemen Press, 2 edition, 1996.

[221] MEMS in microfluidic channels. *Unlimited release*, 2004.

[222] J. Thaysen, R. Marie, and A. Boisen. Cantilever-based bio-chemical sensor integrated in a microliquid handling system. In *Micro Electro Mechanical Systems, 2001. MEMS 2001. The 14th IEEE International Conference on*, pages 401–404. IEEE, 2002.

[223] P.A. Rasmussen, J. Thaysen, O. Hansen, S.C. Eriksen, and A. Boisen. Optimised cantilever biosensor with piezoresistive read-out. *Ultramicroscopy*, 97(1-4):371–376, 2003.

[224] J. Amirola, A. Rodríguez, L. Castaŋer, JP Santos, J. Gutierrez, and M.C. Horrillo. Micromachined silicon microcantilevers for gas sensing applications with capacitive read-out. *Sensors and Actuators B: Chemical*, 111:247–253, 2005.

[225] J. Brugger, R.A. Buser, and N.F. de Rooij. Micromachined atomic force microprobe with integrated capacitive readout. *Journal of Micromechanics and Microengineering*, 2(3):218–220, 1992.

[226] G. Meyer and N.M. Amer. Novel optical approach to atomic force microscopy. *Applied Physics Letters*, 53(12):1045–1047, 2009.

[227] J. Tamayo, M. Alvarez, and L.M. Lechuga. System and method for detecting the displacement of micro- and nanomechnical elements, such as cantilevers. Technical report, 2005.

[228] M. Helm, J.J. Servant, F. Saurenbach, and R. Berger. Read-out of micromechanical cantilever sensors by phase shifting interferometry. *Applied Physics Letters*, 87:064101, 2005.

[229] K. Zinoviev, C. Dominguez, J.A. Plaza, V. Cadarso, and L.M. Lechuga. Light coupling into an optical microcantilever by an embedded diffraction grating. *Applied Optics*, 45(2):229–234, 2006.

[230] M. Yang, X. Zhang, K. Vafai, and C.S. Ozkan. High sensitivity piezoresistive cantilever design and optimization for analyte-receptor binding. *Journal of Micromechanics and Microengineering*, 13:864, 2003.

[231] X. Yu, J. Thaysen, O. Hansen, and A. Boisen. Optimization of sensitivity and noise in piezoresistive cantilevers. *Journal of Applied Physics*, 92:6296, 2002.

[232] G. Yoshikawa, T. Akiyama, S. Gautsch, P. Vettiger, and H. Rohrer. Nanomechanical membrane-type surface stress sensor. *Nano Letters*, 2011.

[233] C.L. Britton Jr, R.L. Jones, P.I. Oden, Z. Hu, R.J. Warmack, S.F. Smith, W.L. Bryan, and J.M. Rochelle. Multiple-input microcantilever sensors. *Ultramicroscopy*, 82(1-4):17, 2000.